

Copyright

by

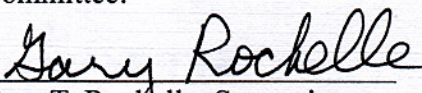
Norman Kirk Yeh

2002

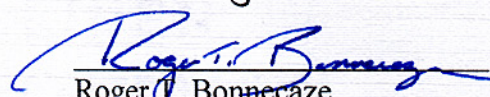
The Dissertation Committee for Norman Kirk Yeh
Certifies that this is the approved version of the following dissertation:

Liquid Phase Mass Transfer in Spray Contactors


Committee:



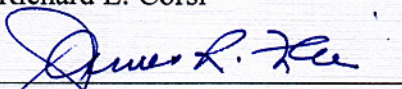
Gary T. Rochelle, Supervisor



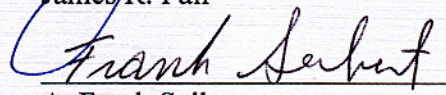
Roger T. Bonnecaze



Richard L. Corsi



James R. Fair



A. Frank Seibert

Liquid Phase Mass Transfer in Spray Contactors

by

Norman Kirk Yeh, S.B., M.S.C.E.P.

Dissertation

Presented to the Faculty of the Graduate School of

The University of Texas at Austin

in Partial Fulfillment

of the Requirements

for the Degree of

Doctor of Philosophy

The University of Texas at Austin

May 2002

In memory of Christopher W. Holder,
a friend who always challenged me to think critically about a variety of subjects and
thus helped me to strengthen my personal beliefs

Acknowledgments

A wise teacher once said:

If one falls down, his friend can help him up. But pity the man who falls and has no one to help him up! ... Though one may be overpowered, two can defend themselves. A cord of three strands is not quickly broken. (Ecclesiastes 4:10,12 NIV)

I am thankful for many people and organizations that have been helpful to me while in graduate school. For three years of my graduate studies, I was fortunate to receive financial support from the U.S. Environmental Protection Agency through the Science to Achieve Results (STAR) Fellowship Program. In addition, the David Bruton Jr. Graduate Fellowship through the UT Graduate School and the Chevron Corporation Endowed Graduate Fellowship through the UT College of Engineering Thrust Program have also been greatly appreciated. In terms of equipment and expertise, the Spraying Systems Company donated some of the nozzles used in this work and provided useful technical support and performance data for those nozzles. The large scale nozzle that was used the pilot scale work was provided by ABB. In addition, ABB and Alstom Power provided initial direction and financial support for the research.

I also thank the UT Separations Research Program and its staff for their generosity and flexibility. Frank Seibert, in addition to serving on my committee, was very supportive and allowed time for me to use the equipment at SRP. Christopher Lewis, Robert Montgomery, Steve Orwick, Steve Briggs, and Clayton Wooten were always ready to give advice and often a helping hand when I was building the pilot scale apparatus. I am especially thankful for De Vu, a fellow graduate student, who was kind enough to serve as my “buddy” when I had to conduct pilot scale experiments during off hours.

In addition, I feel fortunate to have worked with each of the members of my committee. Gary Rochelle has been an excellent advisor and continues teaching me

to think on my feet and ask the question “Why?” Frank Seibert provided valuable feedback and assistance throughout this work, particularly with the pilot scale experiments. My discussions with Roger Bonnacaze helped me to understand the fluid mechanics and his course on surface phenomena gave me an excellent background for the breakup phenomena. Richard Corsi’s input on the importance of sample collection issues was also very helpful and much appreciated. Finally, I was honored to interact with James Fair and benefit from his experience in this area.

The other members of Dr. Rochelle’s research group have been great companions on this journey. Sometimes we shared technical advice, and sometimes it was emotional support or encouragement when the experimental work became frustrating. I was fortunate to share my time at UT with many great friends and researchers: Lia Brodnax, Joseph DeVincentis, Paul Chisholm, Sanjay Bishnoi, Michael Dutchuk, Nicole Pauly, Sharmi Roy, Eric Chen, Amy Nowlin, Stefano Freguia, Dyron Hamlin, George Goff, and Tim Cullinane.

My family has also been a great source of support over the years. My father sparked my interest in science as a child, and my mother has always stressed education and encouraged me to excel. My sister, Karen, has been my strongest supporter and an inspiration for me. Finally, my extended family of Hyde Park Baptist Church and the guys from my men’s small groups have been the highlight of my time in Austin and a constant reminder that the Lord is our strength and shield.

Liquid Phase Mass Transfer in Spray Contactors

Publication No. _____

Norman Kirk Yeh, Ph.D.
The University of Texas at Austin, 2002

Supervisor: Gary T. Rochelle

Spray absorbers are used in the majority of limestone slurry scrubbers to remove sulfur dioxide from the flue gas of coal-fired power plants, and in these systems, the mass transfer is primarily liquid film controlled. Improving the fundamental understanding of spray towers should be helpful in the selection, design, and optimization of nozzles, spray scrubbers, and other gas-liquid contactors. Liquid phase mass transfer in sprays has been measured with carbon dioxide desorption by collecting and analyzing samples of the spray. Commercial hollow cone nozzles were used to determine the effects of spray distance, nozzle pressure drop, and nozzle selection on mass transfer performance. Experiments were conducted with laboratory (1/8 to 3/8 inch) and pilot scale (3 inch) nozzles at pressures of 5 to 20 psi. Significant mass transfer occurred during sample collection, and a quench sampling method was developed to minimize this effect. Spray impact in the sample collector without quenching resulted in 0.2 to 0.7 liquid phase transfer units (N_L), compared to 0.5 to 1.2 transfer units in the spray. Of the mass transfer in the spray, approximately 60% occurs in the liquid sheet before droplet formation. The droplet region can account for less than half of the total N_L . Increasing the nozzle pressure drop resulted in substantially higher mass transfer during spray impact but had negligible effect on the N_L of the spray itself. The spray N_L decreased with nozzle size, and spray distance appears to scale with the nozzle orifice diameter up to 60 orifice diameters.

Table of Contents

List of Tables	xii
List of Figures	xiii
Nomenclature	xv
Chapter 1: Introduction	1
1.1. APPLICATIONS	1
1.2. FLUE GAS DESULFURIZATION	2
1.2.1. Historical implementation.....	3
1.2.2. Wet FGD spray scrubbing	4
1.2.3. Description of limestone slurry scrubbing in spray towers	6
1.3. MASS TRANSFER BACKGROUND	8
1.3.1. General interfacial mass transfer	8
1.3.2. Transfer units	9
1.3.2.1. Calculation of column height.....	10
1.3.2.2. Application to sprays	11
1.4. LITERATURE SUMMARY	12
1.4.1. Limestone slurry scrubbing.....	12
1.4.2. Mass transfer in limestone slurry scrubbing.....	12
1.4.3. Other spray literature	15
1.5. RESEARCH OBJECTIVES AND SCOPE OF WORK	16
Chapter 2: Literature Review	18
2.1. SPRAY NOZZLES	18
2.1.1. Spray patterns.....	18
2.1.2. Nozzle designs	19
2.1.3. Drop size distributions	20
2.2. SPRAY FORMATION	22
2.2.1. Jet breakup	23
2.2.2. Sheet breakup.....	23
2.3. MASS TRANSFER IN SPRAYS	24
2.3.1. Transfer units	25
2.3.2. Mass transfer coefficients	27
2.3.3. Mass transfer during spray droplet formation.....	28
2.3.4. Spray droplet mass transfer.....	30
2.3.5. Surface mass transfer	31
2.4. SUMMARY	31
Chapter 3: Theory	34
3.1. GENERAL MODELS FOR K_L	34
3.1.1. Film theory.....	34

3.1.2. Penetration theory	35
3.1.3. Levich-Davies turbulent model.....	36
3.1.4. Other turbulent models	38
3.2. LIQUID SHEETS.....	39
3.2.1. Sheet hydrodynamics	39
3.2.1.1. <i>Flow regimes</i>	40
3.2.1.2. <i>Sheet breakup</i>	40
3.2.2. Sheet mass transfer	42
3.2.3. Sheet model.....	43
3.2.3.1. <i>Sheet k_L</i>	43
3.2.3.2. <i>Sheet area</i>	43
3.2.3.3. <i>Sheet N_L</i>	46
3.3. SINGLE DROPLETS	46
3.3.1. Droplet hydrodynamics.....	46
3.3.1.1. <i>Flow regimes</i>	46
3.3.1.2. <i>Flow transitions</i>	48
3.3.1.3. <i>Oscillation frequency</i>	48
3.3.1.4. <i>Oscillation damping constant</i>	50
3.3.2. Droplet mass transfer	50
3.3.2.1. <i>Stagnant diffusion</i>	51
3.3.2.2. <i>Steady circulation</i>	52
3.3.2.3. <i>Turbulent circulation</i>	52
3.3.2.4. <i>Oscillation</i>	53
3.3.2.5. <i>Mass transfer data</i>	53
3.3.3. Droplet model	55
3.4. SUMMARY	56
Chapter 4: Experimental Methods.....	57
4.1. BASIS AND RATIONALE	57
4.1.1. Liquid phase controlled mass transfer	58
4.1.2. Equilibrium limitations	58
4.1.3. Calculation of N_L	59
4.2. DESCRIPTION OF APPARATUS	60
4.2.1. Nozzles.....	60
4.2.2. Laboratory contactor.....	62
4.2.2.1. <i>CO₂ delivery and dissolution</i>	65
4.2.2.2. <i>Gas phase CO₂ concentrations</i>	65
4.2.3. Pilot scale contactor	68
4.3. SAMPLE STORAGE	71
4.4. SAMPLE ANALYSIS	72
4.4.1. CO ₂ electrode.....	72
4.4.2. Total carbonate analyzer	73
4.5. SPRAY SAMPLER DEVELOPMENT	73

4.5.1. Simple sampler results	74
4.5.2. Overflow sampler.....	75
4.5.2.1. <i>Overflow sampler development</i>	76
4.5.2.2. <i>Overflow sampler mass transfer</i>	77
4.5.3. Quench sampler	80
4.5.3.1. <i>Quench sampler development</i>	81
4.5.3.2. <i>Quench sampler mass transfer</i>	82
Chapter 5: Spray mass transfer	86
5.1. SHEET OBSERVATIONS	86
5.1.1. Breakup length.....	88
5.1.2. Calculated properties at breakup.....	90
5.2. MASS TRANSFER RESULTS.....	92
5.2.1. Empirical correlations.....	95
5.2.2. Effect of distance	97
5.2.3. Effect of nozzle pressure drop	99
5.2.4. Effect of nozzle size.....	100
5.2.5. Summary.....	103
5.3. ANALYSIS/CALCULATION OF K_L	104
5.3.1. Calculation of $k_L a$	104
5.3.2. Comparison with Levich-Davies theory.....	107
5.3.3. Semi-empirical model.....	111
5.3.3.1. <i>Sheet k_L model</i>	111
5.3.3.2. <i>Droplet k_L model</i>	111
5.3.3.3. <i>Regression results</i>	112
5.3.3.4. <i>Model interpretation</i>	116
5.4. SUMMARY.....	119
Chapter 6: Mass transfer during spray impact	121
6.1. IMPACT INTO LIQUID	121
6.1.1. Experimental methods	122
6.1.2. Results.....	123
6.1.3. Analysis.....	124
6.2. INTERSECTING SPRAYS.....	126
6.2.1. Experimental methods	126
6.2.2. Results.....	129
6.2.3. Comparison with real scrubber conditions	131
6.3. WALL EFFECTS.....	132
6.3.1. Experimental methods	132
6.3.2. Results.....	134
6.3.3. Interpretation.....	135
6.4. APPLICATION TO PUBLISHED DATA	137
6.5. SUMMARY.....	140

Chapter 7: Conclusions	142
7.1. SPRAY MASS TRANSFER AS A FUNCTION OF DISTANCE	142
7.2. SPRAY IMPACT	142
7.3. NOZZLE PRESSURE DROP	143
7.4. NOZZLE SIZE	144
7.5. HIGHLY VARIABLE K_L	144
Chapter 8: Recommendations	146
8.1. GAS PHASE MASS TRANSFER	146
8.2. GAS DISTRIBUTION.....	146
8.3. SPRAY IMPACT	147
8.4. SPRAY INTERFERENCE IN PILOT SCALE SYSTEM.....	148
8.5. CONTACTOR INNOVATIONS	148
Appendix A Nozzle data	150
Appendix B Oscillation criteria	152
Appendix C Calculating k_L and a.....	153
Appendix D Pilot scale apparatus	156
Appendix E Sample storage and stability.....	159
Appendix F Total carbonate analyzer	161
Appendix G Tabulated data.....	165
Appendix H Sample calculations for spray contacting	178
Bibliography	184
Vita	191

List of Tables

Table 1.1.	Capacity (MW) and number of units with FGD technology in 1998 (Jozewicz et al., 1999)	5
Table 1.2.	Parameters for base case simulation of limestone slurry scrubbing (DeVincentis, 1998).....	13
Table 1.3.	Spray level mass transfer units	15
Table 2.1.	Characteristic diameters for droplet size distributions.....	22
Table 2.2.	Literature on liquid phase mass transfer in sprays.....	25
Table 3.1.	Models for k_L in droplets	51
Table 4.1.	Nozzle properties (data provided by the Spraying Systems Company).....	61
Table 4.2.	N_L values for open sampler and 0.04 cm jet	75
Table 4.3.	Overflow sampler characterization	78
Table 4.4.	N_L data for quench sampler development (0.04 cm jet, high and low liquid levels).....	82
Table 4.5.	Quench sampler characterization.....	83
Table 5.1.	Sheet breakup measurements and model predictions	90
Table 5.2.	Calculated sheet properties at breakup	91
Table 5.3.	Spray mass transfer in laboratory experiments ($T = 20-25^\circ\text{C}$).....	93
Table 5.4.	Spray mass transfer in pilot scale experiments (Nozzle: 3CF-SILCNB-120, $T = 35-40^\circ\text{C}$)	94
Table 5.5.	Empirical correlation of spray N_L	96
Table 5.6.	Dimensionless correlation of spray N_L	97
Table 5.7.	Comparison of Re for small nozzles.....	102
Table 5.8.	Comparison of droplet k_L model predictions for 1/8-A-SS-2 nozzle	103
Table 5.9.	Correlation of spray k_{La}	106
Table 5.10.	Regressed parameters and sensitivity for semi-empirical model.....	113
Table 6.1.	Comparison of pool and wall impact N_L correlations.....	137
Table 6.2.	Comparison of published data with predicted N_L for spray impact.....	138
Table A.1.	Data for Spraying Systems nozzles.....	150
Table A.2.	Correlation of spray flow rate	150
Table A.3.	Sauter mean and volume median droplet diameters (Koehn, 2001).....	151

List of Figures

Figure 1.1.	Spray absorber for flue gas desulfurization by limestone slurry scrubbing.....	7
Figure 1.2.	Estimating N_L per spray level	14
Figure 2.1.	Common spray patterns	19
Figure 2.2	Rayleigh jet breakup due to dilational disturbances	23
Figure 2.3	Centrifugal hollow cone spray nozzle (a) top view (b) side view (c) sheet breakup and spray droplet formation.....	24
Figure 2.4.	Droplet diameters and Reynolds numbers for spray mass transfer data in the literature	32
Figure 3.1.	Levich-Davies model	36
Figure 3.2.	Calculation of sheet area.....	44
Figure 3.3.	Regimes of droplet behavior	47
Figure 3.4.	Comparison of data and model predictions for k_L in droplets	54
Figure 4.1.	Centrifugal hollow cone nozzle operation (Spraying Systems A-series WhirlJet nozzles)	61
Figure 4.2.	Laboratory spray contactor	63
Figure 4.3.	Nozzle piping in the laboratory contactor.....	64
Figure 4.4.	Top cover of the laboratory contactor.....	64
Figure 4.5.	Apparatus for measuring gas phase CO_2 concentrations	66
Figure 4.6.	Gas phase CO_2 concentrations (Nozzle: $\frac{3}{8}$ -A-SS-20, $\Delta P = 10$ psi).....	67
Figure 4.7.	Pilot scale spray contactor	69
Figure 4.8.	Top view of pilot scale contactor.....	70
Figure 4.9.	Overflow sample collector	76
Figure 4.10.	Effect of overflow ratio on sampler mass transfer.....	77
Figure 4.11.	Parity plot of the overflow sampler correlation	79
Figure 4.12.	Quench sample collector.....	81
Figure 4.13.	Quench sampler results.....	84
Figure 5.1.	Sheet breakup (Nozzle: $\frac{3}{8}$ -A-SS-20, $\Delta P = 10$ psi).....	87
Figure 5.2.	Sheet breakup (Nozzle: 3CF-SILCNB-120, $\Delta P = 5$ psi).....	88
Figure 5.3.	Parity plot of sheet breakup correlation (Equation 5.3).....	89
Figure 5.4.	Parity plot of empirical spray N_L correlation (Table 5.5).....	96
Figure 5.5.	Spray mass transfer in laboratory experiments (Nozzle: $\frac{1}{8}$ -A-SS-5, quench sampler).....	98
Figure 5.6.	Spray mass transfer in pilot scale experiments (Nozzle: 3CF-SILCNB-120, quench sampler)	99
Figure 5.7.	Effect of nozzle size on spray mass transfer ($\Delta P = 10$ psi, quench sampler).....	101
Figure 5.8.	Calculation of effective contactor volume.....	104
Figure 5.9.	Parity plot for $k_L a$ correlation (Table 5.9).....	106

Figure 5.10. Comparison of spray mass transfer with Levich-Davies calculation (Nozzle: 1/8-A-SS-5).....	108
Figure 5.11. Comparison of spray mass transfer with Levich-Davies calculation ($\Delta P = 10$ psi).....	110
Figure 5.12. Semi-empirical model results ($\Delta P = 10$ psi).....	114
Figure 5.13. Parity plot of sheet mass transfer coefficients (Predicted - Equation 5.10, calculated - data and Equation 5.12).....	115
Figure 5.14. Model predictions of sheet and droplet k_L as a function of distance (calculations based on physical properties at 22°C).....	116
Figure 5.15. Comparison of semi-empirical model predictions with literature data for droplet k_L	118
Figure 5.16. Comparison of k_L , area, and N_L predictions with experimental data (Nozzle: 1/4-A-SS-10, $\Delta P = 5$ psi, correlated $L_b = 5.03$ cm).....	119
Figure 6.1. Sampler for spray impact into liquid.....	122
Figure 6.2. Comparison of pool sampler and quench sampler results (Solid points – pool sampler, hollow points – quench sampler).....	124
Figure 6.3. Pool mass transfer (Nozzle: 1/4-A-SS-10, model curves from Equation 6.1).....	125
Figure 6.4. Intersecting sprays experimental setup.....	127
Figure 6.5. Top view of nozzles for intersecting sprays experiment.....	127
Figure 6.6. Spray flux profile in intersecting sprays experiment (10.2 cm below nozzles).....	129
Figure 6.7. Effect of spray interaction on mass transfer.....	130
Figure 6.8. Intersecting sprays mass transfer.....	131
Figure 6.9. Wall effect experimental setup (a) side view (b) top view.....	133
Figure 6.10. Comparison of wall effect with wetted wall model.....	135
Figure 6.11. Wall impact mass transfer (model curves from Equation 6.7).....	136
Figure D.1. Pilot facility of the UT Separations Research Program.....	156
Figure D.2. Diagram of piping for the pilot spray column.....	157
Figure D.3. Detailed diagrams of pilot scale spray contactor.....	158
Figure E.1. Sample storage and stability.....	159
Figure F.1. Typical calibration curve for carbonate analyzer.....	163

Nomenclature

a	Interfacial area per unit column volume (cm^{-1})
A_{cs}	Cross-sectional area (cm^2)
A_d	Area of a liquid droplet (cm^2)
A_i	Interfacial area (cm^2)
a_L	Interfacial area per unit liquid volume (cm^{-1})
b	Oscillation amplitude constant (dimensionless)
C	Liquid concentration (mol/cm^3)
c_f	Drag coefficient (-)
D	Diffusion coefficient (cm^2/s)
d	Drop diameter (cm)
$d_{e,i}$	Equivalent spherical diameter of droplet i (cm)
d_{or}	Orifice diameter of nozzle (cm)
d_{vs}	Sauter mean drop diameter (cm)
E	Enhancement factor = k_L/k_L^o (dimensionless)
f	Liquid fraction (dimensionless)
h	Sheet half-thickness (cm)
H_A	Henry's constant for species A ($\text{Pa cm}^3/\text{mol}$)
H_L	Height of liquid phase transfer unit (cm)
k_c	Gas phase mass transfer coefficient for concentration driving force (cm/s)
K_G	Overall gas phase mass transfer coefficient ($\text{mol}/\text{cm}^2 \text{ s Pa}$)
k_G	Gas phase mass transfer coefficient ($\text{mol}/\text{cm}^2 \text{ s Pa}$)
K_L	Overall liquid phase mass transfer coefficient (cm/s)
k_L	Liquid phase mass transfer coefficient (cm/s)
k_L^o	Liquid phase physical mass transfer coefficient (cm/s)
L_b	Sheet breakup length (cm)
L_c	Characteristic length scale (cm)
L_w	Length of wetted wall (cm)
m	Phase equilibrium constant (dimensionless)
N_A	Mass transfer flux of species A ($\text{mol}/\text{cm}^2 \text{ s}$)
n_A	Moles of species A (mol)
N_g	Gas phase transfer units (dimensionless)
n_i	Number of drops with diameter d_i (dimensionless)
N_L	Liquid phase transfer units (dimensionless)
N_{OG}	Overall gas phase transfer units (dimensionless)
P	Pressure (Pa)
Q_L	Liquid flow rate (cm^3/s)
r	Distance from the spray nozzle (cm)
Re	Reynolds number = $L_c U_c \rho / \mu$
Sc	Schmidt number = $\mu / \rho D$

Sh	Sherwood number = kL_c/D
t	Contact time (s)
U	Velocity (cm/s)
U'	Superficial liquid velocity = Q_L/A_{cs} (cm/s)
u*	Interfacial velocity (cm/s)
u _y '	Turbulent velocity fluctuation normal to interface (cm/s)
V	Volume (cm ³)
w	Width (cm)
We	Weber number = $L_c U_c^2 \rho / \sigma$
x	Sheet length (cm)
y	Distance from interface (cm)
z	Column height (cm)

Greek

α	Ratio of maximum to minimum surface area (dimensionless)
δ	Film thickness (cm)
δ_1	Thickness of Levich-Davies laminar sublayer (cm)
δ_2	Thickness of Levich-Davies diffusion sublayer (cm)
ΔP	Nozzle pressure drop (psi)
ε	Rate of energy dissipation by turbulence per unit mass (cm ² /s ³)
φ	Fractional liquid holdup (dimensionless)
ϕ	Flat spray angle (radians)
θ	Spray angle (°)
λ	Thickness of zone of damped turbulence (cm)
μ	Viscosity (g/cm s)
ν	Kinematic viscosity = μ/ρ (cm ² /s)
ρ	Density (g/cm ³)
σ	Surface tension (dynes/cm ²)
τ_{dmp}	Time constant for viscous damping (s)
τ_o	Interfacial shear stress (dynes/cm)
τ_{osc}	Time constant for droplet oscillation (s)
τ_p	Penetration time (s)
u_o	Characteristic turbulence velocity (cm/s)
ω	Empirical constant, found by Amokrane et al to be 0.8 (-)

Subscripts

A	species A
b	at sheet breakup
c	characteristic scale
d	droplet
E	Effective or eddy property
f	final (steady state) value

g gas phase
i at interface
L liquid phase
lm logarithmic mean
o initial value
or at the nozzle orifice
p sampler
s sheet
w wall
 ∞ bulk

Superscripts

* in equilibrium with bulk

Chapter 1: Introduction

Many separations and gas cleaning applications rely on efficient mass transfer in gas-liquid contactors. Various unit operations have been employed to accomplish these separations by transferring a given component from one phase into another. The most common types of contactors include tray columns and packed columns, and a large body of data exists for mass transfer in these systems. Spray columns are also commonly used as gas-liquid contactors for certain separations, but the literature for mass transfer in spray contactors is fairly sparse compared to that for trays and packing. In particular, the liquid phase mass transfer characteristics of sprays have not been well described and further study is warranted.

1.1. APPLICATIONS

Spray towers have traditionally been used as gas-liquid contactors in applications where low gas-side pressure drop is essential and a high degree of separation is not required. Spray nozzles disperse the liquid phase into droplets to provide gas-liquid contact area without the need for column internals such as trays or packing. Since the gas stream flows through a fairly disperse droplet region instead of through a packing element or the froth on a tray, the pressure drop is much lower in spray contactors than in packed or tray columns. The compression of the inlet gas can be a major operating cost, so spray contactors are potentially useful for processes with very high gas flow rates and for those at or below atmospheric pressure. Examples include flue gas cleaning, carbon dioxide (CO₂) capture from flue gas, and vacuum distillation/evaporation.

Another advantage of spray columns over tray or packed columns is that sprays are attractive for use with fouling liquids. Particles in the gas or liquid streams can become lodged in packing elements or in the holes on trays. This fouling reduces the free passage and therefore increases the pressure drop through the contactor. Severe fouling can affect the gas-liquid distribution or completely plug the internals.

On the other hand, since trays and packing are not necessary in a spray column, plugging the column internals is not an issue. Plugging of the spray nozzles may be possible if the liquid contains particulates, such as in slurries. However, many spray nozzles are designed with large open passages to reduce the possibility of plugging (Fair et al., 1984).

Unfortunately, the open nature of a spray tower also makes it susceptible to severe back mixing in the continuous phase. The high velocity spray droplets tend to entrain the surrounding gas and may result in a well mixed gas phase. Thus, true countercurrent operation is difficult to obtain, and spray towers are often designed to provide only one theoretical stage of separation (Fair et al., 1984). Separations that are more difficult require staging the sprays or collecting and re-spraying liquid.

Sprays have also been used to disperse one liquid phase into another liquid in extraction applications. Much literature has been published on spray extraction, including fundamental studies of mass transfer in circulating droplets. The understanding of spray extraction processes may be useful for comparison but may not be directly applicable to gas-liquid systems. The density and viscosity ratios of the dispersed to the continuous phases for liquid-liquid systems are so different from gas-liquid systems that relative velocities and droplet behavior may vary widely. (Clift et al., 1978)

1.2. FLUE GAS DESULFURIZATION

One of the primary applications for spray contactors is in flue gas desulfurization (FGD). In coal-fired power plants, the presence of sulfur in the coal leads to the formation of sulfur dioxide (SO_2). Sulfur oxides pose serious risks to human health, and the need for controlling their emissions has been acknowledged for many years. Furthermore, other oxidation products of SO_2 , such as acidic sulfates, lead to acid rain as well as their more direct health threats.

1.2.1. Historical implementation

In the U.S., the 1970 Clean Air Act called for national ambient air quality standards to limit the ambient concentrations of sulfur oxides and various other pollutants. The Clean Air Act also called for New Source Performance Standards (NSPS) that required all new industrial sources to install the best-demonstrated pollution control technology. The Environmental Protection Agency promulgated standards for the regulated air pollutants in 1971 and worked with the states to develop State Implementation Plans for reducing the emissions of sulfur oxides. FGD systems were regarded as the best available technology for controlling SO₂ when low-sulfur fuels were unavailable. In addition, only FGD technologies were able to achieve the emissions standards in the time required by the Clean Air Act (Train, 1976).

FGD systems installed under the NSPS became operational in about 1977, and additional amendments to the Clean Air Act were passed that year as well. The Lowest Achievable Emission Rate was required for sources in non-attainment areas, and the Best Available Control Technology was required for all other new sources (Gage, 1980). The electric utility industry was required to remove up to 90% of the SO₂ from the flue gas of power plants. The standard was dependent upon the sulfur content of the coal being used, varying from 90% down to 70% removal for the low sulfur coals. In 1990, deregulation allowed the construction of natural gas instead of coal-fired power plants. Since gas did not produce high SO₂ emissions, FGD systems were not installed into new plants. However, FGD continues to be used in retrofits of existing coal-fired facilities

The Clean Air Act amendments of 1990 created a two-phase plan to reduce acid rain caused by SO₂ and nitrogen oxides (NO_x) emissions. Title IV of the Clean Air Act called for SO₂ emissions to be reduced to 10 million tons below 1980 levels. Phase I of the Acid Rain SO₂ Reduction Program ran from 1995 to 1999 and allocated emissions allowances to 261 generating units. In order to comply with Phase I, 52% of the units switched to lower sulfur fuels, which was found to be a

relatively inexpensive compliance option. Another 32% of the units received or purchased sufficient allowances to cover their emissions. Scrubbers were installed in 10% of the units, in some cases over-complying with Phase I in anticipation of the tighter limits of Phase II. With these methods, the units under Phase I reduced SO₂ emissions from 9.3 million tons in 1985 to 4.4 million tons in 1995 (EPA, 1997).

Phase II of program, which began in 2000, affects more than 2,000 units and has more stringent requirements than Phase I. A permanent cap on the number of SO₂ allowances restricts the total emissions to 8.95 million tons (EPA, 2001). Scrubbers may need to be installed to meet the required emissions reductions. Advances in scrubbing technology have achieved removal efficiencies of 95% or more in retrofit applications and 99% or more in new installations (Jozewicz, 1999).

Recently, in 2000 and 2001, energy crises such as the rolling blackouts in California have highlighted concerns over energy production. In May 2001, the Bush administration released a National Energy Policy, which included a higher priority on increased production of oil, coal, gas, and nuclear energy (U.S. DOE, 2001; PBS Frontline, 2001). If more coal-fired power plants are to be constructed, then FGD scrubbing will most likely continue to be an essential part of maintaining environmental standards.

1.2.2. Wet FGD spray scrubbing

Wet scrubbing is the most proven FGD process, and it is commercially well established in most industrialized countries. In wet FGD applications, the SO₂ is absorbed from the flue gas with an aqueous solvent, which is typically sprayed into the flue gas. Wet scrubbing processes comprise 85% of the market for flue gas desulfurization, and 80% of installed FGD systems worldwide are wet scrubbers. The wet lime (CaO) or limestone (CaCO₃) slurry process accounts for 70% of the market for FGD systems (Oskarsson et al., 1997).

The status of SO₂ scrubbing in the U.S. at the end of 1998 is summarized in Table 1.1 (Jozewicz et al., 1999). FGD systems were installed on 235 units

representing 100,000 MW of capacity. Wet FGD technology accounted for 178 units or 82,900 MW of electricity producing capacity. Of these, the lime/limestone processes dominate the applications because of high SO₂ removal efficiency, cost effectiveness, and production of salable byproduct. Although lime is more reactive, the limestone process is preferred over lime because the limestone is less expensive. The preferred process for wet FGD worldwide is the limestone forced oxidation process, in which reaction products are oxidized to gypsum. The gypsum has superior dewatering characteristics, and commercial grade gypsum may be produced and sold for wallboard manufacturing.

Table 1.1. Capacity (MW) and number of units with FGD technology in 1998 (Jozewicz et al., 1999)

Technology		United States	Abroad	World Total
Wet	Limestone	55,540	107,790	163,330
	Lime	14,196	6,976	21,172
	Dolomitic lime	10,292	50	10,342
	Other	2,831	1,558	4,389
	Subtotal MW (number of units)	82,859 (178)	116,374 (356)	199,233 (534)
Dry	Subtotal MW (number of units)	14,386 (49)	11,008 (74)	25,394 (123)
Other	Subtotal MW (number of units)	2,798 (8)	2,059 (13)	4,857 (21)
Total MW (number of units)		100,043 (235)	129,441 (443)	229,484 (678)

Limestone scrubbing is accomplished in various types of contactors, including spray towers, venturi scrubbers, and static and mobile packed beds. However, countercurrent spray contactors are the most commonly used (Brogren and Karlsson, 1997). Spray towers were developed for limestone slurry scrubbing by Chemico, and the first commercial unit was installed in the Texas Utilities Monticello plant (Hewitt

and Saleem, 1980). Spray scrubbers are an attractive technology for flue gas desulfurization because of their low gas-side pressure drop, low maintenance costs, and relatively inexpensive equipment. Since slurry would tend to foul packing or trays, spray scrubbers avoid maintenance costs associated with shutting down and cleaning the column internals (EPA, 2000).

1.2.3. Description of limestone slurry scrubbing in spray towers

In spray towers, the liquid slurry is discharged through nozzles at high velocity, e.g. about 40 ft/s for a typical pressure drop of 10 psi across the nozzle. The slurry exits the nozzle as a contiguous sheet of liquid, and then aerodynamic instabilities cause the sheet to disintegrate into drops (Lefebvre, 1989). The formation of droplets provides gas-liquid contact area and facilitates the mass transfer between the gas stream and the limestone slurry.

A diagram of a limestone slurry scrubbing spray tower is given in Figure 1.1. The flue gas containing SO₂ enters the bottom of the absorber and countercurrently contacts limestone slurry, which is sprayed into the absorber through a series of spray headers. In the figure, only two levels of spray headers are shown, but two to six spray headers may be commonly used. Each spray header contains several nozzles in a grid arrangement. The vertical spacing between the spray headers is typically from four to six feet (1.2 to 1.8 m). The nozzles on a given spray header are positioned to obtain good coverage of the tower cross-section and to prevent gas from bypassing or “sneaking” past the spray. The actual nozzle spacing varies, but according to an experienced practitioner, a rule of thumb for 90° spray nozzles gives a nozzle spacing of about four feet, or 1.2 m (Laslo, 2002).

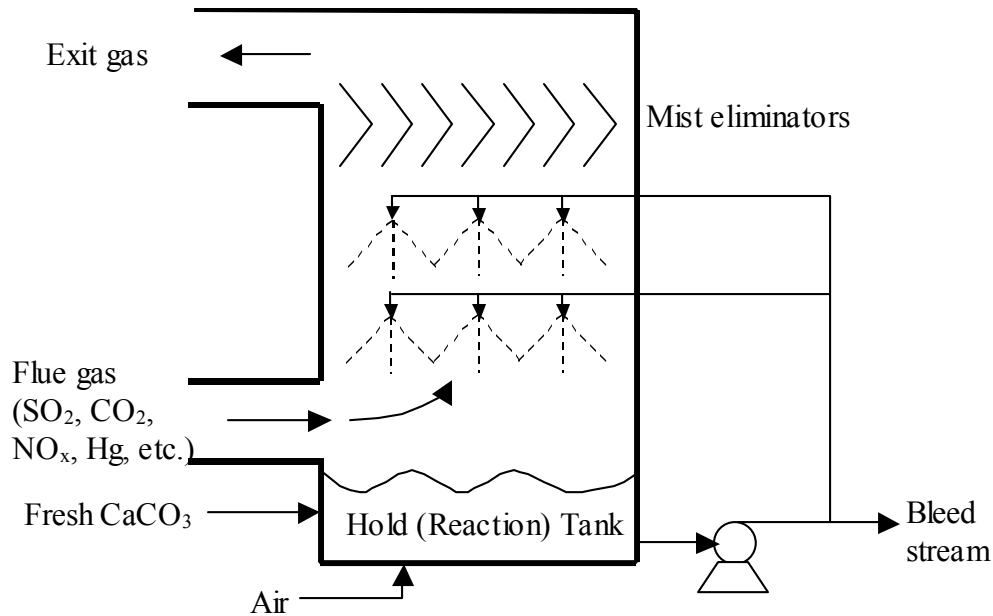


Figure 1.1. Spray absorber for flue gas desulfurization by limestone slurry scrubbing

Since the nozzles often are closely spaced, interaction between the sprays from different nozzles is expected to become significant at some distance. For example, if the nozzle horizontal spacing is four feet, then the spray within a two-foot radius of the nozzle may be essentially independent of sprays from other nozzles, but beyond that two-foot radius, interaction between the sprays may become significant. This spray tower configuration also means that the interior of the spray tower is not completely open but is occupied by a variety of pipes and nozzles associated with the spray headers. Thus, many spray droplets are likely to collide with other sprays, the tower walls, or the piping of adjacent spray headers before impacting and accumulating in the bottom of the absorber.

The SO_2 is absorbed into the spray and reacts with the dissolved limestone, and the cleaned gas passes through mist eliminators to catch any entrained droplets before exiting the top of the absorber. Meanwhile, the spent slurry falls to the bottom of the absorber, into the hold tank or reaction tank. In the hold tank, fresh limestone is added, and if the scrubber is operated in forced oxidation mode, air may be used to

oxidize sulfite species to sulfate. The calcium sulfate is removed in a bleed stream and crystallized for disposal or sale as gypsum byproduct. The fresh slurry is recycled to the spray headers.

1.3. MASS TRANSFER BACKGROUND

The absorption of SO₂ in a limestone slurry scrubber is a complex process involving mass transfer with chemical reaction. In order to understand the performance of a spray scrubber, some background in interfacial mass transfer is needed. The transfer unit approach for modeling and characterization of mass transfer in contacting devices is also introduced.

1.3.1. General interfacial mass transfer

As a molecule of gas is absorbed into a liquid phase, it may encounter significant mass transfer resistance in either phase. The flux of species A may be calculated as the concentration driving force in a given phase multiplied by the mass transfer coefficient in that phase. If species A is involved in a chemical reaction in the liquid boundary layer, then the mass transfer coefficient is modified to include an enhancement factor.

$$N_A = k_g(P_{A\infty} - P_{Ai}) = k_L(C_{Ai} - C_{A\infty}) = k_L^o E(C_{Ai} - C_{A\infty}) \quad (1.1)$$

Thus, the effective mass transfer coefficient for the liquid phase is separated into a physical mass transfer coefficient, which accounts for diffusive and convective contributions to mass transfer, and an enhancement factor, which depends on the chemical reaction kinetics and concentrations of other species that react with species A. The interfacial concentrations are typically unknown, but they are assumed to be in equilibrium at the interface so that the flux equations can be written in terms of overall driving forces and overall mass transfer coefficients.

$$N_A = K_G (P_{A\infty} - P_A^*) = K_L (C_A^* - C_{A\infty})$$

where $P_A^* = H_A C_{A\infty}$ or $C_A^* = \frac{P_{A\infty}}{H_A}$ (1.2)

$$\frac{1}{K_G} = \frac{1}{k_g} + \frac{H_A}{k_L^0 E} \quad \frac{1}{K_L} = \frac{1}{k_g H_A} + \frac{1}{k_L^0 E}$$

In order to characterize the system fully, the chemical reaction kinetics, gas solubility, and the mass transfer coefficients in both phases must be known. However, simplifications or approximations can be made if the overall resistance to mass transfer is considered as the sum of resistances in the gas and the liquid phases. The rate of mass transfer may be gas or liquid phase controlled, depending on where most of the resistance to mass transfer occurs. For relatively soluble gases (small H_A) and/or fast chemical reactions (large E), the mass transfer tends to be gas phase controlled ($K_G \approx k_g$). On the other hand, for relatively insoluble gases, the liquid resistance tends to dominate the mass transfer.

1.3.2. Transfer units

When describing the mass transfer performance of a contactor, the number of mass transfer units is often used. The transfer unit expression can be derived by a material balance on one phase in a differential section of the contactor. In terms of the liquid phase and a liquid phase mass transfer coefficient, mass transfer of species A into the liquid phase results in a concentration change.

$$k_L (C_{Ai} - C_A) dA_i = Q_L dC_A + \frac{dn}{dt} \quad (1.3)$$

At steady state, the accumulation term is zero, and the equation can be rearranged and integrated over the entire column to obtain the expression for the number of liquid phase transfer units for the contactor.

$$N_L = \int_{C_{A,i,n}}^{C_{A,i,out}} \frac{dC_A}{C_{Ai} - C_A} = \int_0^{A_i} \frac{k_L dA_i}{Q_L} \quad (1.4)$$

Similar developments can be used to obtain expressions for the number of gas phase transfer units (N_g), overall gas phase transfer units (N_{OG}), and overall liquid phase transfer units (N_{OL}) in terms of the appropriate mass transfer coefficients and volumetric flow rates.

1.3.2.1. Calculation of column height

Usually, as in the case of a packed column, the above equation would be integrated over a section of the column to determine the height of packing required. In order to perform this integration, several assumptions or simplifications are often made. The differential interfacial area (dA_i) is expressed as the product of the interfacial area per unit contactor volume (a), column cross-sectional area (A_{cs}), and differential column height (dz). An average value of k_L would also be assumed so that all the terms on the right hand side of the equation are constant except for z . Then, the height of a liquid phase transfer unit is defined as the superficial liquid velocity divided by $k_L a$.

$$N_L = \frac{k_L a}{Q_L/A_{cs}} z = \frac{1}{H_L} z \quad (1.5)$$

The concentration integral is slightly more complicated, but a good approximation is the concentration change divided by the log mean concentration driving force. The log mean driving force is an accurate approximation if C_{Ai} is constant or a linear function of C_A . This condition is satisfied for dilute solutions, which obey Henry's Law and for which the L/G ratio does not change over the column. Then, the equilibrium and operating lines are straight, and the log mean is an appropriate average driving force. (King, 1980)

$$N_L = \frac{C_{A,out} - C_{A,in}}{(C_{Ai} - C_A)_{lm}}$$

where $(C_{Ai} - C_A)_{lm} = \frac{(C_{Ai,out} - C_{A,out}) - (C_{Ai,in} - C_{A,in})}{\ln\left(\frac{C_{Ai,out} - C_{A,out}}{C_{Ai,in} - C_{A,in}}\right)}$ (1.6)

1.3.2.2. Application to sprays

The above analysis is useful for packed columns because the cross-sectional area and the interfacial area per unit contactor volume are constant. If the interfacial area is not well distributed over the contactor volume, then the area per unit volume term changes with position. The height of a transfer unit is not constant, and this form of the equation cannot be integrated conveniently to analyze the performance of the contactor. Thus, this type of analysis can be useful for spray columns only far from the spray nozzles, but close to the nozzle, the spray is conical and necessarily not yet well distributed over the contactor cross-section. In the spray scrubber shown in Figure 1.1, nearly all of the contactor volume consists of regions where the spray is conical and not well distributed, so equation (1.5) is of limited use in describing the mass transfer characteristics of the scrubber.

As an alternative, the material balance may be performed on a moving control volume, such as a droplet or other element of fluid.

$$VdC_A = k_L A_i (C_{Ai} - C_A) dt \quad (1.7)$$

The number of transfer units can be defined in terms of concentrations as before, but instead of an interfacial area per unit contactor volume (a), the ratio of area to liquid volume (a_L) is used.

$$N_L = \int_{C_{A,in}}^{C_{A,out}} \frac{dC_A}{C_{Ai} - C_A} = \int_0^t k_L a_L dt = k_L a_L \Delta t \quad (1.8)$$

This type of analysis assumes that the fluid element (droplet) can be considered independent of other fluid elements in the system. For example, equation (1.8) would be an appropriate expression for the N_L of a droplet that does not undergo significant secondary breakup or coalescence with other droplets.

1.4. LITERATURE SUMMARY

1.4.1. Limestone slurry scrubbing

The chemical reactions in the limestone slurry have been studied extensively under well-characterized mass transfer conditions (Gage and Rochelle, 1992), and computer simulations have been employed to study the effect of different parameters on SO₂ removal. Examples include the work of Noblett et al. (1995), Agarwal (1995), Brogren and Karlsson (1997), and DeVincentis (1998). However, in these models, the liquid mass transfer coefficient usually must be provided or assumed, and the simulations are used to study the effect of other parameters on SO₂ removal. For example, Brogren and Karlsson assumed liquid mass transfer coefficients of 0.07 cm/s near the nozzle and 0.02 cm/s away from the nozzle. DeVincentis assumed a ratio of k_L^o/k_g equal to 200 atm·cm³/mol.

Brogren and Karlsson calculated the gas phase mass transfer coefficient and the chemical reactions and showed that the mass transfer is liquid phase controlled in much of the absorber. Near the nozzles at the top of the absorber, their calculated gas phase resistance is 60% of the total mass transfer resistance. Near the nozzles at the bottom of the absorber, the mass transfer is 40% gas phase controlled. With the lower k_L values away from the nozzles, Brogren and Karlsson found that the gas phase resistance only accounted for 15% of the total. Therefore, the liquid phase mass transfer is an important parameter for limestone slurry scrubbing in spray towers, and it should be better understood.

1.4.2. Mass transfer in limestone slurry scrubbing

Alternatively, one might attempt to regress liquid mass transfer coefficients from actual plant data. However, in commercial applications, the spray tower often has several spray nozzles positioned at different levels and orientations. Multiple nozzles may be placed at the same height and/or at various other heights within the tower. In addition, nozzles may be directed upward as well as downward.

Consequently, the sprays from different nozzles may interact with each other and can form complex patterns. The interaction of these sprays can make the regression of liquid phase mass transfer coefficients difficult.

Nevertheless, a rough estimate of the liquid phase mass transfer in a limestone slurry scrubber can be made. The base case parameters of DeVincentis (1998), given in Table 1.2, may be assumed representative values for a spray scrubber.

Table 1.2. Parameters for base case simulation of limestone slurry scrubbing (DeVincentis, 1998)

Spray levels	4
L/G per level	25 gal/mcf
Total N_g	6.9
k_L°/k_g	200 atm·cm ³ /mol

Using the definitions of N_L and N_g , the ratio of the transfer units is calculated from the mass transfer coefficients and the volumetric flow rates of gas and liquid.

$$\frac{N_L}{N_g} = \frac{k_L^\circ A_i}{Q_L} \frac{Q_g}{k_g RT A_i} = \frac{1}{RT} \frac{k_L^\circ/k_g}{Q_L/Q_g} \quad (1.9)$$

For consistent units, the RT term in equation (1.9) converts the gas phase mass transfer coefficient from k_g for a partial pressure driving force to k_c for a concentration based driving force. (Hines and Maddox, 1985; among others) With these values, a total N_L for the spray scrubber was estimated at 3.8.

The presence of four spray levels leads to the question of how to distribute the total N_L among the different sprays. If each spray header contributes equally to the total N_L , then an N_L per spray header of 0.95 would be expected. However, 25 gal/mcf of fresh liquid is introduced at each spray level. If the spray is only active in the level where it is introduced, then the liquid from each spray header may be considered independently. This situation would be consistent with all of the mass transfer occurring at the nozzle and independently of other sprays. Conceptually,

these assumptions would be equivalent to removing the spray from the bottom of each spray header as shown in Figure 1.2a. Each of the spray levels would have an N_L of 3.8.

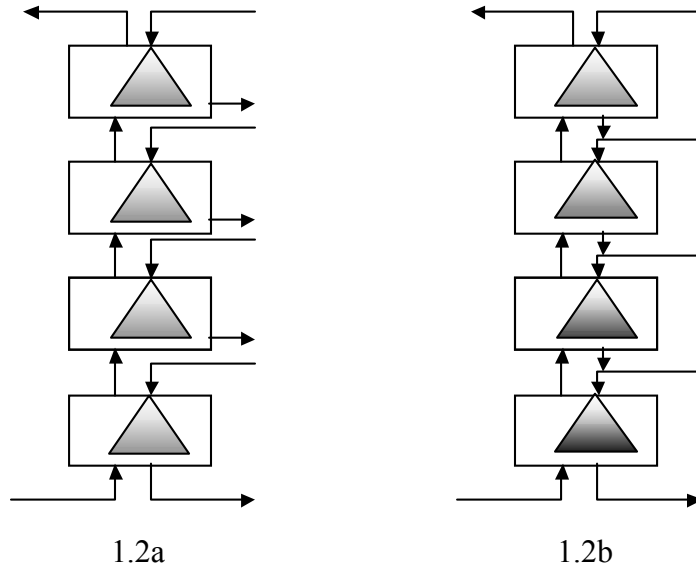


Figure 1.2. Estimating N_L per spray level

If the spray levels are not independent, then liquid from one spray header could remain active in subsequent spray levels. DeVincentis used this approach (Figure 1.2b) in modeling the spray tower. At the bottom of each spray level, the spent slurry from above was mixed with fresh slurry and sprayed into the next level. Thus, the L/G increases as the liquid flows down the absorber. DeVincentis assumed a constant k_L^o/k_g and a profile of N_g values for the spray levels. The N_g values for the lower spray levels decrease slightly because less efficient mass transfer and/or droplet agglomeration were expected. The N_g profile and the corresponding N_L values are given in Table 1.3. An additional section was included at the bottom of the absorber to model the region between the last spray level and the reaction tank. No new slurry was added to this section.

Table 1.3. Spray level mass transfer units

Spray level	N_g	N_L
1 (top)	1.9	4.2
2	1.7	1.9
3	1.5	1.1
4	1.3	0.7
Bottom	0.5	0.3

Therefore, estimates of N_L for each spray header in a limestone slurry scrubber cover a wide range, from 1 to 4, depending on the assumed interaction between the sprays. Uncertainty in the k_L^o/k_g and N_g parameters from DeVincentis would also affect the estimate of N_L . For example, Agarwal performed modeling and parameter estimation for limestone slurry scrubbing in a turbulent contact absorber. The k_L^o/k_g and N_g parameters were regressed for a large-scale contactor and found to be $271 \pm 103 \text{ cm}^3\text{atm/mol}$ and 2.97 ± 0.54 , respectively. The parameters had high negative covariance, and Agarwal reported elliptical confidence regions to represent uncertainty in the estimates.

1.4.3. Other spray literature

Relatively little data are available for mass transfer in sprays, and many of them may not be applicable to FGD systems. Most of the literature for mass transfer in sprays has been limited to small spray droplets, about $200 \mu\text{m}$ in diameter, but the droplets in limestone slurry scrubbing are typically in the $2000 \mu\text{m}$ range. Some data has been published for droplets in the appropriate size range, but the experiments focused on single droplets at or below terminal velocity. In the spray, droplets are formed at high velocity and decelerate during fall, but it is not clear that they would ever reach terminal velocity in a commercial scrubber.

Previous researchers measured the bulk concentrations of the gas and liquid in and out to determine the mass transfer performance of the spray. However, this

approach neglected mass transfer during sampling and wall effects, which lead to overestimates of the spray mass transfer. Since the overall removal is usually the goal of a scrubber, this error may not be significant if characterizing a particular unit. However, extrapolating such data to new designs may be problematic because the mass transfer may not be occurring in the spray as expected. The other sources of mass transfer not only inflate the magnitude of the mass transfer, but they may also differ from spray droplet mass transfer in their dependences on distance, velocity, etc.

A more detailed review of the literature and theory for mass transfer in sprays is given in Chapters 2 and 3.

1.5. RESEARCH OBJECTIVES AND SCOPE OF WORK

The primary objective of this work is to measure the liquid phase mass transfer in sprays representative of those found in flue gas desulfurization. The resulting data improves the fundamental understanding of mass transfer in gas-liquid systems, particularly in large droplets at high velocity and soon after droplet formation. In addition, this work provides a more detailed understanding of the processes at work in a spray contactor and their relative significance for liquid phase mass transfer. Data for mass transfer during spray droplet formation, fall, and impact are presented that demonstrate the large magnitude of mass transfer during droplet formation and impact relative to mass transfer to falling droplets.

To avoid wall effects, local measurements of the spray were conducted so that the mass transfer as a function of distance could be measured more accurately. Consequently, this work also involved designing laboratory and pilot scale experimental spray columns and methods for liquid sample collection from a high velocity gas-liquid stream. Sample collection devices and methods were developed to measure mass transfer during spray impact and sample collection. The sampling effect was minimized in order to measure the mass transfer performance of the spray accurately. The description of the equipment and the validation of the experimental methods are the subject of Chapter 4.

Data for the spray N_L as a function of operating parameters such as nozzle size, distance from the nozzle and nozzle pressure drop are presented in Chapter 5. Semi-empirical correlations and theoretical interpretations of the mass transfer observed in the spray are also discussed. Spray impact mass transfer is examined in Chapter 6 to measure the significance of the effects and to address the question of where mass transfer occurs in a real spray contactor. Chapter 7 summarizes the conclusions for mass transfer in sprays and during spray impact. Finally, the implications of this work and recommendations for further research are discussed in more detail in Chapter 8.

These measurements of the liquid phase mass transfer in spray contactors should be useful for describing the performance of wet FGD limestone slurry scrubbers. This understanding can also have a strong influence on the selection, design, and innovation of nozzles, spray towers, and other types of gas-liquid contactors.

Chapter 2: Literature Review

Properties of sprays are reviewed and summarized below. First, a brief survey of the general characteristics of sprays and spray nozzles is presented. The basic processes of spray droplet formation are introduced so that a discussion of mass transfer before and after droplet formation can follow. The basic description also lays the foundation for a more theoretical discussion in the following chapter. Finally, the literature for liquid phase mass transfer in sprays is reviewed. Special attention is given to sample collection issues and wall effects because they limit the applicability of data from one column to another system.

2.1. SPRAY NOZZLES

Several kinds of spray nozzles are available and may be classified by the spray pattern produced and the mode of spray formation. Nozzles are selected for a particular application based on the desired spray characteristics, such as the flow rate, spray pattern, or the droplet size. In addition, the nozzle style and the nozzle material are usually selected for chemical compatibility and resistance to erosion and/or plugging.

2.1.1. Spray patterns

Spray nozzles can generate a variety of patterns, including flat spray, full cone, and hollow cone spray patterns (Figure 2.1). The flat spray pattern is a thin, triangular spray and has a rectangular or elliptical cross section. The full, or solid, cone spray pattern is a conical spray with a circular impact area, which makes full cone nozzles useful for applications like liquid distribution onto packing (Trompiz and Fair, 2000). The hollow cone spray pattern is a conical spray with a ring shaped impact pattern. A hollow cone spray nozzle also generates smaller droplets than a full cone spray of comparable flow rate. Since the smaller droplets have greater area

per unit volume, hollow cone sprays are sometimes favored for heat and mass transfer applications.

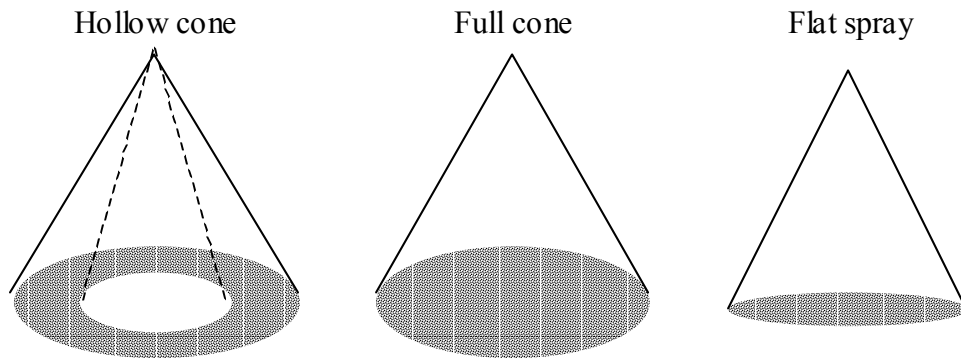


Figure 2.1. Common spray patterns

2.1.2. Nozzle designs

Several types of nozzles are also widely used and may be classified by the nozzle geometry or mode of spray formation. Fan spray nozzles have narrow, elongated orifices, either rectangular or oval shaped. When the liquid flows through the orifice, a thin flat sheet of liquid is formed. As the sheet extends, it tends to spread and the thickness of the sheet decreases until the sheet breaks up due to aerodynamic instabilities.

Jet impingement nozzles consist of a liquid jet and an impact surface. After the jet impinges on the surface, the deflected liquid spreads and forms a sheet of liquid that expands radially and then disintegrates. Spiral nozzles are similar in principle because the liquid impinges on the spiral “pigtail” and is deflected to form a conical sheet of liquid. The spiral can also be designed so that two or more concentric cones are formed, and a full cone spray pattern is generated.

In centrifugal nozzles, also called pressure swirl or tangential nozzles, the fluid enters a hollow chamber through one or more tangential inlets and swirls around inside the chamber before exiting the orifice of the nozzle. The rotational flow inside the whirl chamber results in the formation of an air core, and the liquid exits the

nozzle orifice as a conical liquid sheet, which then breaks up into droplets. In some nozzles, the rotational flow is generated by turning vanes inside the nozzle body instead of tangential inlets.

The most common type of spray nozzle in limestone slurry scrubbing is the centrifugal hollow cone nozzle. The centrifugal nozzles have large open passages, which are less likely to become obstructed by slurry particles. These nozzles generate hollow cone sprays by the breakup of a conical sheet of liquid. Since some types of nozzles generate full cone sprays by forming concentric conical sheets, the mass transfer with the hollow cone nozzles should be indicative of these types of full cone nozzles as well.

2.1.3. Drop size distributions

Spray nozzles generate a spectrum of droplet sizes, and various mathematical forms have been used to characterize the droplet size distribution. The log-normal distribution describes many particle size distributions found in nature. If the droplet size is assumed to result from a large number of small impulses and their effects are proportional to the droplet size, the log-normal distribution can be derived theoretically (Marshall, 1954).

$$f(d) = \frac{1}{\sqrt{2\pi}d\sigma_g} \exp\left[-\frac{(\ln d - \ln d_{ng})^2}{2\sigma_g^2}\right] \quad (2.1)$$

where $f(d)$ is the distribution function, the number of droplets of diameter d

σ_g is the geometric standard deviation

d_{ng} is the number geometric mean drop diameter

Several empirical distribution functions have also been developed to represent the droplet size distribution. The Rosin-Rammler distribution is the most widely used empirical distribution function (Lefebvre, 1989).

$$Q(d) = 1 - \exp\left[-\left(\frac{d}{x}\right)^q\right] \quad (2.2)$$

where $Q(d)$ is the volume fraction in droplets of diameter less than d
 q and x are empirical distribution parameters

The distribution parameter x is a representative droplet diameter, for which $Q(d) = 1 - 1/e$. Thus, 63.2% of the spray volume is contained in droplets whose diameter is less than x . The parameter q can be interpreted as a measure of the spread of the distribution. If q is large, then the spread of the distribution is small and the spray is more uniform. The distributions from most spray nozzles are described well by values of q between 1.5 and 4.

In practice, the drop size distribution is simplified by reporting mean or characteristic diameters, which are chosen to represent the important qualities of the spray for a given application. According to ASTM standard E799-92, various characteristic drop sizes may be represented systematically by

$$d_{ij}^{(i-j)} = \frac{\sum_k d_k^i}{\sum_k d_k^j} = \frac{\int d^i f(d) dd}{\int d^j f(d) dd} = \frac{d_{i0}}{d_{j0}} \quad (2.3)$$

For example, in mass transfer applications, the ratio of surface area to liquid volume is important so the Sauter or surface-volume mean diameter is often used. The Sauter mean is the diameter of a spherical droplet that has the same surface to volume ratio as the entire spray. Several characteristic droplet diameters are given in Table 2.1 along with some fields of application.

Table 2.1. Characteristic diameters for droplet size distributions

Name(s)	Symbol	Application
Arithmetic mean	d_{10}	Evaporation rates, comparisons
Surface area mean	d_{20}	Surface area controlled processes (e.g. absorption)
Volume mean	d_{30}	Hydrology
Surface-diameter mean	d_{21}	Adsorption
Evaporative mean	d_{31}	Evaporation, molecular diffusion
Volume/surface (Sauter) mean	d_{32}	Mass transfer
Mean diameter over volume (DeBroukere or Herdan mean)	d_{43}	Combustion
Volume median	$d_{V0.5}$	

Usually, the volume median diameter is reported by the nozzle manufacturer to characterize the droplet size for a given spray. Data for $d_{V0.5}$ is often readily available as a function of operating pressure for nozzles spraying water under laboratory conditions. If the droplet size distribution is described by the Rosin-Rammler distribution, the parameter q can be used to calculate the other characteristic diameters from the volume median. For the Sauter mean diameter,

$$\frac{d_{V0.5}}{d_{32}} = 0.693^{1/q} \Gamma\left(1 - \frac{1}{q}\right) \quad (2.4)$$

Data provided by the Spraying Systems Company for their centrifugal hollow cone nozzles give the Sauter mean diameter as a function of the volume median (Appendix A). This data is consistent with a q value of 2.2.

2.2. SPRAY FORMATION

The primary function of a spray nozzle is the dispersion of one liquid into another fluid, and the act of spray formation can be accompanied by mass transfer. Therefore, some background on the fluid dynamics of droplet breakup is essential to a complete understanding of the mass transfer in sprays. The goal of this section is merely to describe the basic phenomena that lead to spray droplet formation. This introduction shows that the spray consists of two distinct regions: (1) a liquid continuous region before and/or during breakup and (2) the spray droplet region. A

more detailed discussion of the theory and fluid dynamics of breakup is reserved for Chapter 3.

2.2.1. Jet breakup

A simple example of droplet formation is Rayleigh's classic example of cylindrical jet breakup (Rayleigh, 1878). Rayleigh showed that a cylindrical jet of inviscid fluid was unstable to symmetric disturbances (Figure 2.2).

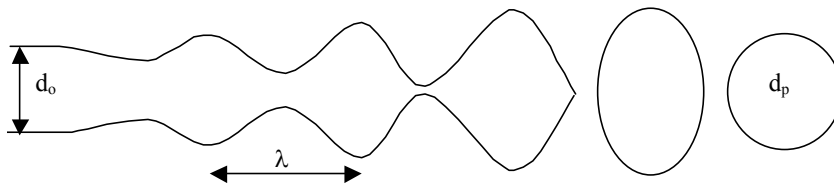


Figure 2.2 Rayleigh jet breakup due to dilational disturbances

For a cylinder of fluid with diameter d_0 , rotationally symmetric sinusoidal disturbances with wavelength $\lambda > d_0$ will tend to grow. Eventually, the amplitude of the disturbance becomes as large as the jet radius, and the jet is pinched off. The volume of fluid within one wavelength then contracts into a droplet of diameter d_p . In addition, a linear stability analysis shows that the fastest growing disturbance has $\lambda = 4.51d_0$, so the breakup of an inviscid cylindrical jet would be expected to generate droplets with $d_p = 1.89d_0$.

2.2.2. Sheet breakup

In centrifugal spray nozzles, a conical sheet of liquid is formed instead of a jet. As the liquid moves farther away from the nozzle, the cone expands and the sheet thins. The breakup of sheets occurs by a wavy mechanism (Figure 2.3), as opposed to the dilational, symmetric disturbances that govern jet breakup (Fraser et al., 1962). In the sheet, asymmetric disturbances grow, and waves form. These waves thin the sheet even more, until it breaks into ribbons. The ribbons contract into cylindrical ligaments oriented perpendicular to the direction of motion, and the ligaments then disintegrate similar to Rayleigh's inviscid jet.

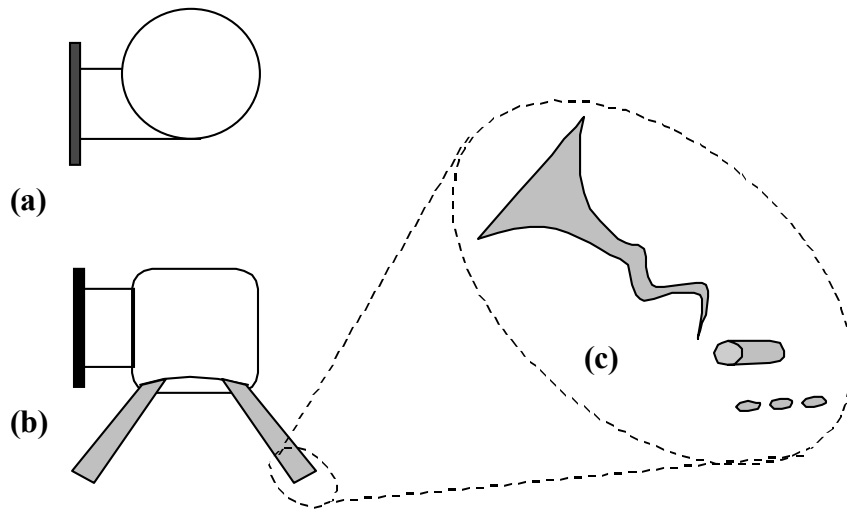


Figure 2.3 Centrifugal hollow cone spray nozzle (a) top view (b) side view (c) sheet breakup and spray droplet formation

2.3. MASS TRANSFER IN SPRAYS

Relatively little data is available for mass transfer in sprays, compared to trays or packed gas-liquid contactors. In addition, much of the data consists of bulk measurements for the entire contactor, where the mass transfer is measured by an overall concentration change between the inlet and the outlet gas and/or liquid streams. With such measurements, mass transfer during droplet formation, spray interaction, wall effects, and sample collection are often neglected. All of these effects become indistinguishable from spray mass transfer, and the overall results are frequently interpreted as droplet mass transfer even though several fundamentally different processes may be at work. As a result, limited reliable information exists for mass transfer in sprays as a function of distance or for the relative importance of mass transfer occurring in different parts of the spray contactor.

Table 2.2. Literature on liquid phase mass transfer in sprays

	Nozzles	$d_{v0.5}$ (μm)	Column (m)		N_L
			D	Z	
Pigford and Pyle, 1951	Full cone (1-6)	~ 200	0.80	1.32	1.2 - 3.5
Mehta and Sharma, 1970	Full cone	420 - 600	0.21	1.23	~0.9 - 1.6
Epstein, 1975	Spiral (full?) cone nozzles on 2-4 headers	*	2.4	6.4	*
Lin et al., 1977	Flat spray	180 - 380	0.4	0.2	1.0 - 3.0
Simpson and Lynn, 1977	Jet impingement, fan, centrifugal	~150	0.45	1.37	~3.5
Pinilla et al., 1984	Full cone	3400 - 3800	0.45	1.30	*
Jarvis and Burke, 1988	Single full cone nozzle on 6 headers	600 - 1600	1.5	7.2	*
McWhirter et al., 1995	(Surface aeration)	*	n/a	n/a	0.6 - 0.7
Taniguchi et al., 1997	Full cone	100 - 300	0.18	0.50	*
Dimiccoli et al., 2000	Full cone	~100	*	*	*

* = Values were not reported

2.3.1. Transfer units

Pigford and Pyle (1951) measured the number of gas and liquid phase transfer units in a 0.80 m diameter spray contactor with one to six spray nozzles. Oxygen was desorbed from water and the liquid concentrations of the inlet and outlet were analyzed to obtain a total N_L for the unit. In experiments with six full cone nozzles, the N_L of the contactor was approximately proportional to the total liquid flow rate. This proportionality could also be interpreted as a square root dependence on the nozzle pressure drop. N_L was independent of gas flow rates until about 600 lb/ft²hr, which corresponds to a gas velocity of about 0.7 m/s or the terminal velocity of a spherical water droplet approximately 180 μm in diameter. Since the volume median diameter of the droplets in these experiments was about 200 μm , a significant fraction of the spray might be entrained at the higher gas velocities.

By reducing the number of nozzles from six to three and increasing the nozzle pressure by a factor of four, N_L of the contactor was increased by 2.8 times at the

same total liquid flow rate. If the sprays for the different nozzles did not interact, then this result implies that N_L varied with $(\Delta P)^{0.74}$. The effect of nozzle size was estimated by changing the number and size of the nozzles and attempting to maintain constant nozzle pressure and liquid flow rate. Reducing the nozzle orifice diameter by 27% had a small effect, but the nozzle pressure also differed by 33% so no effect of nozzle size was observed. Experiments at two nozzle heights (0.66 and 1.32 m) showed that N_L was not proportional to distance and that mass transfer rates were higher close to the nozzle. The N_L at half the nozzle height was 0.76 times that for the taller contactor, so N_L varied with $z^{0.4}$.

Pilot scale FGD work with spray scrubbers was conducted for the EPA and the Electric Power Research Institute (EPRI). Epstein (1975) reported data for SO_2 absorption using a venturi/spray tower, turbulent contact absorber (TCA), and a marble bed absorber. The number of gas phase transfer units was determined by absorbing SO_2 into sodium carbonate. Experiments with limestone as the absorbent were also conducted and the mass transfer was found to be liquid phase controlled. From the definitions of the number of transfer units and K_G (see Chapter 1),

$$N_{OG} = \frac{K_G A}{Q_g} = \left(\frac{1}{N_g} + \frac{m Q_g}{E Q_L} \frac{1}{N_L} \right)^{-1} \approx \frac{E Q_L}{m Q_g} N_L \quad (2.5)$$

Note that in Equation 2.5, N_L is defined in terms of the physical mass transfer coefficient (k_L^o), and m is a phase equilibrium constant similar to a Henry's Law constant. The equilibrium pressure of SO_2 over the solution was assumed zero, and the scrubber performance was modeled as follows.

$$N_{OG} = \frac{y_{in} - y_{out}}{(y - y^*)_{lm}} \approx \ln \left(\frac{y_{in}}{y_{out}} \right) \quad (2.6)$$

The enhancement factor was assumed to vary with the slurry pH, and the physical mass transfer was assumed to vary with the gas velocity and the liquid to gas ratio. The concentration of SO_2 in the gas inlet was not found to have a statistically

significant effect. The resulting SO₂ removal was fitted to a function of gas velocity (U_g) in ft/s, the liquid to gas ratio (L/G) in gal/mcf, and slurry pH.

$$\frac{y_{in} - y_{out}}{y_{in}} = 1 - \exp \left[-0.018 U_g^{0.36} \left(\frac{L}{G} \right)^{0.74} \left(1 + 5.2 \times 10^{pH-7} \right) \right] \quad (2.7)$$

In order to extract N_L values from the SO₂ removal data, values of m and E must be determined. If the solubility of SO₂ in water and the regression for E as a function of pH are used, then N_L values between 3.8 and 6.6 are computed. However, the presence of chemical equilibrium reactions in the bulk solution increases the overall solubility of SO₂ in the system. On the other hand, if the solution approaches saturation, then Equation 2.5 is no longer valid and the solubility is effectively reduced. DeVincentis (1998) found that equilibrium limitations could be significant in spray scrubbing systems.

Jarvis and Burke (1988) also conducted sodium tests to obtain N_g values in three absorber configurations: a spray tower, counterflow trays, and a packed column. Limited data for N_{OG} was also obtained for limestone scrubbing, and the values ranged from 0.5 to 1.0. These values were significantly lower than the N_g values, such that the ratio N_g/N_{OG} ranged from 2.8 to 4.0. As discussed earlier, extracting values for N_L from this data also requires estimates of m and E. However, in this instance, data for E were not available.

2.3.2. Mass transfer coefficients

Mehta and Sharma (1970) also studied mass transfer in a spray column and reported values of k_g, k_L, and a. Experiments with a full cone nozzle (estimated d_{v0.5} = 420 to 600 μm) were conducted in a spray column 0.205 m in diameter and 1.23 m tall. Values of k_La were reported from 0.004 to 0.015 s⁻¹ for superficial liquid rates of 19,000 to 41,000 kg/m²hr. From the column dimensions and Equation 1.5, the N_L for the contactor varied from 0.93 to 1.62. Some initial attempts were made to separate the liquid flowing down the walls from the spray region in the center of the column.

However, distinguishing the two was not possible because of splashing of the liquid from the wall.

Pinilla et al. (1984) measured mass transfer coefficients ($k_g a$, k_L , and a) and axial dispersion in a spray tower 0.45 m in diameter. A full cone centrifugal nozzle was used to generate droplets 3400 to 3800 μm in diameter. For a nozzle height of 1.30 m, the volumetric gas phase mass transfer coefficient ($k_g a$) was determined by absorbing SO_2 into NaOH solution. These values for $k_g a$ were then used to extract values for k_L and area from the absorption of CO_2 into a carbonate/bicarbonate solution with sodium arsenite as a catalyst. For liquid rates of 1.0 to 1.5 $\text{kg}/\text{m}^2\text{s}$, the values of k_L ranged from 23×10^{-5} to 5×10^{-5} m/s , and the area was about 90 to 130 m^{-1} . These results correspond to $k_L a$ values between 0.021 and 0.007 s^{-1} , very close to the results of Mehta and Sharma even though the liquid flow rates were ten times smaller in the work of Pinilla et al. However, given the column dimensions, the N_L values calculated from Equation 1.5 were between 25 and 5.

Given the column dimensions, the high liquid flow rates, and large droplet sizes, wall effects were probably still significant in the results of Pinilla et al. In both the work of Mehta and Sharma and of Pinilla et al., much of the liquid would be expected to impact the sides of the column and flow down the walls. Thus, these data may not be applicable to sprays in the large open design of a limestone slurry scrubber because such wall effects would not be present.

2.3.3. Mass transfer during spray droplet formation

Lin et al. (1977) and Simpson and Lynn (1977) both commented on the significance of mass transfer in the sheet before/during droplet formation. Lin et al. measured the stripping of butane and F-22 refrigerants from water in a vacuum spray column using a flat spray nozzle. The column diameter was wide enough that spray did not contact the walls before reaching the bottom of the column. However, spray impact at the bottom of the column still could have contributed to the total mass transfer. The spray nozzle had an orifice diameter of 0.038 cm and generated droplets

with Sauter mean diameters of 180 to 380 μm depending on flow rate. The sheet breakup was estimated between 1 and 2 cm, and N_L measurements were performed at nozzle heights of 6, 13, and 20 cm. N_L values between 1.5 and 2.5 were obtained within 0.20 m of the nozzle and increased linearly with distance. Lin et al. proposed the following correlation to represent their data.

$$N_{OL} = 2.4 \times 10^{-3} We_g^{0.2} \left(982 + \frac{z}{d_{or}} \right) \quad (2.8)$$

where $We_g = \frac{\rho_g U_L^2 d_{or}}{\sigma}$

This correlation assumed that the N_{OL} of the sheet and the droplets have the same dependence on gas density (ρ_g) and liquid velocity (U_L). The exponent on the Weber number indicates that the gas pressure has a small effect on the mass transfer and that N_{OL} varies with $U_L^{0.4}$ or $(\Delta P)^{0.2}$. If this correlation is extrapolated back to the point of sheet breakup, then two thirds or more of the total mass transfer occurs in the sheet and only one third in the droplets. Lin et al. also noted that the mass transfer in the sheet did not agree with predictions based on simple laminar flow. The experimental N_{OL} values of 1.5 to 2.5 were 5-10 times higher than predicted and had the opposite dependence on liquid velocity.

Simpson and Lynn (1977) also performed desorption experiments with carbon dioxide, oxygen, butane, and Freon 114 in a vacuum spray chamber. Experiments with jet impingement, fan, and centrifugal nozzles showed that the mass transfer performance was much greater than predicted for diffusion into stagnant spheres. For the centrifugal nozzle at a height of 0.26 m, a 97% approach to equilibrium was achieved ($N_L = 3.5$), compared with 35% predicted for diffusion into a stagnant droplet. Even at nozzle heights of 2.0 to 6.0 cm, the measured approach to equilibrium was about 90% ($N_L = 2.3$). The sheet breakup length was estimated between 1.0 and 2.5 cm, so Simpson and Lynn concluded that most of the mass transfer was occurring in the sheet.

Simpson and Lynn also compared the observed mass transfer performance with a theoretical model developed by Hasson et al. (1964) for sheets of fan spray nozzles. The Reynolds numbers for the sheets indicated semi-turbulent conditions, and fair agreement with the model was achieved if an effective diffusion coefficient of one to three times the molecular diffusion coefficient is used. The fan nozzles were operated in the turbulent flow regime, and the results could be correlated with an average effective diffusion coefficient of eight times the molecular diffusion coefficient. When the jet impingement nozzles were operated in the laminar flow regime, the theoretical model matched the experimental data well. Under turbulent conditions, the N_L was higher than predicted and independent of flow rate. The N_L did exhibit some dependence upon the nozzle orifice diameter and the diffusion coefficient for the system being tested. The major weaknesses of the model were its inability to predict the sheet length, the transition to turbulence, or the turbulent enhancement of the mass transfer.

As in other work, these studies used overall measurements of the contactor performance and attributed all of the mass transfer to the spray. Unlike the literature discussed in the previous section, Lin et al. and Simpson and Lynn did attempt to distinguish between the sheet (or droplet formation region) and the spray droplets. However, they did not take into account the mass transfer that could be occurring during spray impact on the walls or the bottom of the spray column. If these effects were constant for all experimental conditions, then all of the measured N_L values may simply be slightly higher than the true N_L values for the spray region. More likely, the extra mass transfer varied with liquid velocity, flow rate, etc. If so, then not only the magnitude but also the dependence of N_L on distance, velocity, and nozzle size becomes suspect.

2.3.4. Spray droplet mass transfer

Taniguchi et al. (1997) performed CO_2 absorption experiments in a 0.18 m diameter spray column. A full cone spray nozzle with a 0.78 mm orifice produced

volume mean diameters of 100 to 300 μm . Water or aqueous sodium hydroxide solution was sprayed into a chamber that was supplied with air and CO_2 . The number fluxes of drops, the drop sizes and the CO_2 concentrations of the drops were measured at various distances from the nozzle. The droplet volume mean diameter was correlated with the liquid flow rate, and mass transfer coefficients were obtained from the observed absorption of CO_2 . The results for the mass transfer coefficients compared favorably with a solid sphere penetration model. Thus, the authors concluded that oscillation and circulation within the drop as well as drop coalescence and breakup were not significant. However, Dimiccoli et al. (2000) also performed CO_2 absorption experiments with a similar nozzle (full cone, $d_{30} = 123 \mu\text{m}$) and concluded that a stagnant droplet model was less reliable than an internally well-mixed droplet model based on Levich's theory.

2.3.5. Surface mass transfer

McWhirter et al. (1995) developed a model for mass transfer in surface aerators that separated the process into a liquid spray mass transfer zone and a surface reaeration mass transfer zone. Based on a regression of data from a full scale surface aerator, the k_{La} of the surface zone was high enough that 63-66% of the overall oxygen transfer was expected to occur in the surface zone and only 34-37% in the spray zone. The surface aerator had a different configuration from a spray column for gas scrubbing, but the results suggest that significant mass transfer can occur on the surface of a liquid when spray impacts.

2.4. SUMMARY

Most of the data in the literature may not be easily applied to commercial limestone slurry scrubbing spray columns. The approximate droplet diameters and gas phase Reynolds numbers for the spray literature are graphed in Figure 2.4. The line for terminal velocity in Figure 2.4 represents the data available in the literature for mass transfer in single droplet experiments. Typical nozzles in FGD spray scrubbers generate droplets of about 2000 μm , whereas most of the spray literature

deals with droplets in the 200 μm range (Figure 2.4). Larger droplets are expected to experience more internal circulation and oscillation. These effects may be less significant for absorption into smaller drops but may be the dominating mechanism for mass transfer in droplets for limestone slurry scrubbing. Furthermore, very little data exists on the effect of nozzle size and scale up issues.

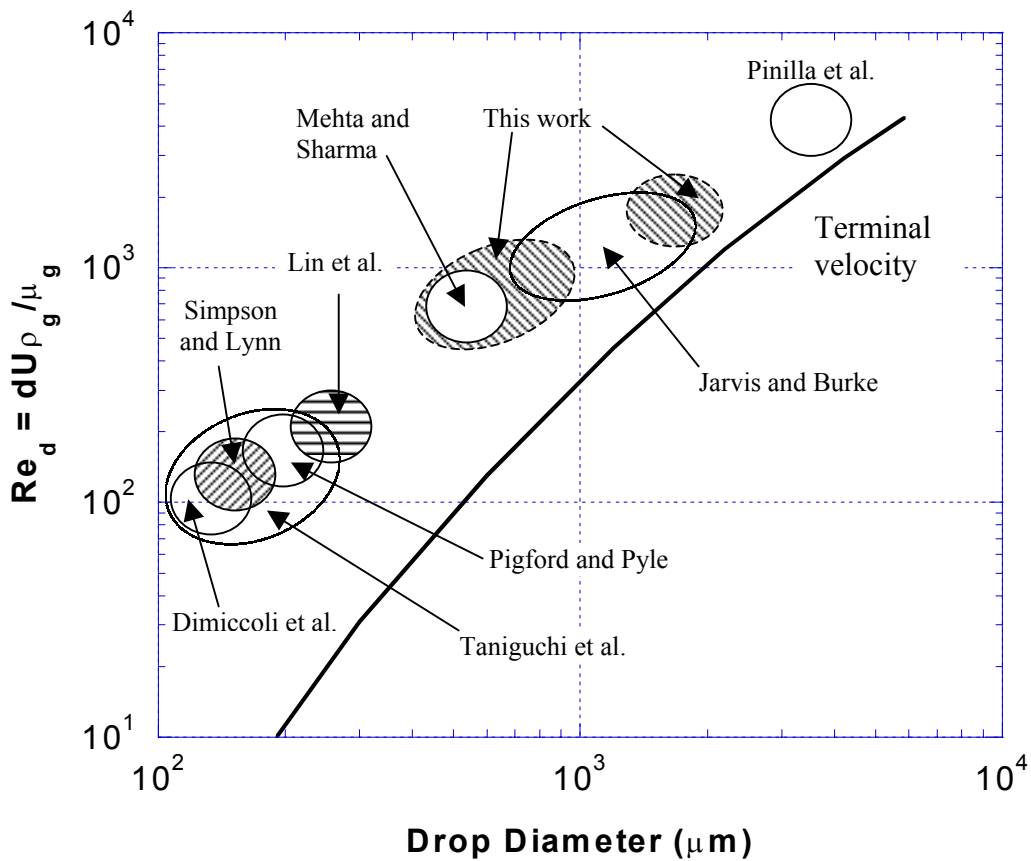


Figure 2.4. Droplet diameters and Reynolds numbers for spray mass transfer data in the literature

Therefore, the major contributions of this work are to be higher quality data for the liquid phase mass transfer in gas-liquid sprays. This work also focuses on sprays with large droplets and the effects of nozzle size, both of which have little data in the literature. Reliable sampling methods and local measurements of the spray, as opposed to measurements of overall contactor performance, were necessary to isolate

the contribution of the spray to the mass transfer and in order to avoid wall effects. The local measurements also give a clearer understanding of the variation of mass transfer with distance and the relative contribution of mass transfer in the sheet. The significance of wall effects and mass transfer during spray impact are also examined to gain a more complete picture of liquid phase mass transfer in spray contactors.

More data for liquid phase mass transfer as a function of distance would also improve the design and optimization of nozzle selection, spacing, and orientation in spray contactors for limestone slurry scrubbing and other applications as well. This data would include the relative significance of mass transfer in different sections of the contactor. At least a few investigators have commented on the importance of the sheet/droplet formation region and spray impact onto a liquid surface. In addition, other types of spray impact may prove to be important, such as wall effects or interaction between sprays. However, most data in the literature has neglected these effects and reported bulk measurements for the overall contactor performance. Thus, it is difficult to separate mass transfer in the spray from sample collection or spray impact effects.

Chapter 3: Theory

3.1. GENERAL MODELS FOR K_L

Fluid dynamics impact the mass transfer, and any fundamental model for mass transfer must be based upon an understanding of the fluid flow near the interface. Several models have been proposed for the prediction of mass transfer coefficients. In each model, essential characteristics of the liquid flow field are approximated by a simplified mathematical expression. Often the flow representation includes a hypothetical parameter (e.g. film thickness or penetration time), which may or may not be possible to predict independently. If not, then these parameters are treated as adjustable and used to match experimental data. Given the assumed representation of the flow, the conservation equation is solved to obtain the flux and concentration profile, and the mass transfer coefficient is calculated as the flux divided by the concentration driving force.

3.1.1. Film theory

According to film theory, all of the mass transfer resistance occurs in a thin, stagnant film near the gas-liquid interface. Beyond some film thickness (δ), the fluid is well mixed, and the mass transfer resistance is negligible. The presence of turbulence in the liquid phase would tend to reduce the film thickness by enhancing convective mass transfer and mixing. For a dilute component diffusing through a stagnant planar film, the concentration profile is linear from the interface ($y = 0$) to the film thickness ($y = \delta$), where the concentration is equal to the bulk concentration.

Since the concentration profile is linear, the slope is constant and the mass transfer coefficient can be represented as follows.

$$N_A = -D_A \frac{dC_A}{dy} = D_A \frac{C_{Ai} - C_{A\infty}}{\delta} \quad (3.1)$$

$$k_L = \frac{N_A}{C_{Ai} - C_{A\infty}} = \frac{D_A}{\delta} \quad (3.2)$$

Film theory is a useful conceptual model, but it has several weaknesses that limit its applicability. The film theory model predicts a linear dependence of k_L on D_A , but experimentally k_L usually depends on $D_A^{1/2}$. In addition, since the film thickness is usually unknown, it can only be treated as an adjustable parameter and the model is not predictive. Finally, the assumption of the stagnant film is not physically realistic because it leads to a discontinuity in the concentration profile at $y = \delta$.

3.1.2. Penetration theory

Higbie (1935) proposed that the fluid at the interface could be represented as stagnant for some short period of time. After this penetration time (τ_p), the fluid is completely mixed, and the process begins again. For transient planar diffusion into a stagnant fluid, the flux and the concentration profile are a function of the exposure time. The mass transfer coefficient is calculated by averaging the flux over the penetration time and dividing by the concentration driving force as follows.

$$N_A = \sqrt{\frac{D_A}{\pi t}} (C_{Ai} - C_{A\infty}) \quad (3.3)$$

$$k_L = \frac{\frac{1}{\tau_p} \int_0^{\tau_p} N_A dt}{(C_{Ai} - C_{A\infty})} = 2 \sqrt{\frac{D_A}{\pi \tau_p}} \quad (3.4)$$

Again, this model has only one unknown parameter (τ_p instead of δ), but τ_p has the advantage that it can be determined independently in some situations. For liquid flow through packing, the penetration time can be estimated by the time required to flow down a packing element. At the bottom of the packing element, the liquid is mixed before continuing down to the next packing element. Using the penetration theory as a predictive model depends on the presence of a mixing phenomena and the ability to calculate the frequency of that mixing.

However, even as an empirical model, penetration theory is preferred over film theory because penetration theory correctly predicts that k_L varies with $D_A^{1/2}$. Thus, data for different chemical systems may be compared by correcting for the diffusion coefficients. For example, k_L data collected for CO_2 absorption may be used to predict k_L for SO_2 by multiplying k_{L,CO_2} by $(D_{\text{SO}_2}/D_{\text{CO}_2})^{1/2}$.

3.1.3. Levich-Davies turbulent model

The theory by Levich (1962) and modified by Davies (1972) describes mass transfer in a turbulent liquid. Turbulent velocity fluctuations normal to the interface provide convective mass transfer. However, surface tension restrains turbulent eddies as they approach the interface. When an eddy from the bulk approaches the interface, the surface is deformed. Surface tension opposes this deformation and prevents the eddy from splashing through the interface.

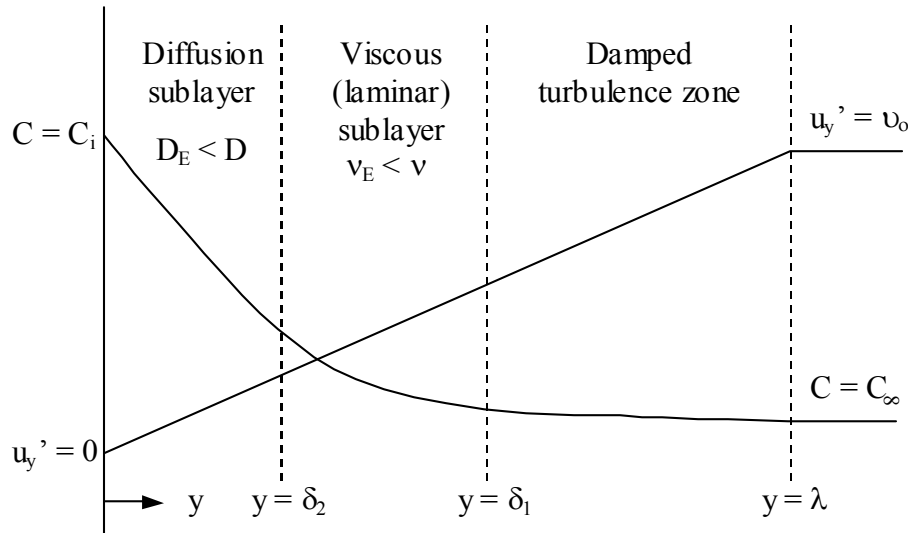


Figure 3.1. Levich-Davies model

Thus, the turbulent velocity fluctuations in the y direction are damped within some distance of the interface. Levich called this region a zone of damped turbulence with thickness λ . Beyond this region ($y > \lambda$), the velocity fluctuations are constant at v_o and related to the degree of turbulence in the bulk liquid. Within the zone of

damped turbulence ($y < \lambda$), the turbulent transport varies with the magnitude of velocity fluctuations (u_y'). Much closer to the interface, the damping of u_y' is so great that the flow is equivalent to laminar flow. In this viscous sublayer ($y < \delta_1$), the turbulent kinematic viscosity due to eddy motion is less than the molecular value. Very close to the interface is a region mathematically equivalent to a diffusion sublayer ($y < \delta_2$), where turbulent transport is less than molecular diffusion.

The thicknesses of the sublayers are calculated as a function of v_o , the characteristic turbulence velocity or friction velocity. The flux through each region of the analysis is evaluated and equated to obtain the following expression for the mass transfer coefficient.

$$k_L = 0.32D^{1/2}v_o^{3/2}\rho_L^{1/2}\sigma^{-1/2} \quad (3.5)$$

To model mass transfer in a turbulent jet, Davies and Ting (1967) assumed that the turbulence is formed in the pipe before the liquid exits the orifice. After the orifice, no new eddies form and velocity gradients in the liquid phase become negligible because the frictional resistance of the gas is negligible. The characteristic velocity is calculated according to the Blasius friction factor correlation for pipe flow.

$$v_o = \sqrt{\frac{\tau_o}{\rho_L}} = 0.2U\text{Re}^{-1/8} \quad (3.6)$$

$$k_L = 0.028\text{Re}^{1.312}\left(\frac{\mu^3 D}{\rho^2 d^3 \sigma}\right)^{1/2} \quad (3.7)$$

$$\text{Sh} = 0.028\text{Re}^{5/16}\text{Sc}^{1/2}\text{We}^{1/2} \quad (3.8)$$

The numerical coefficient and the dependence of k_L on Re and D were verified experimentally for turbulent jets. However, no effect of jet diameter was observed, and for the small jets, the numerical coefficient was found to be 0.019 instead of 0.028. Davies and Hameed (1971) absorbed gas into turbulent jets of kerosene, where the surface tension was much lower than for water. Their results agreed with the theoretical predictions for the exponents of Re , D , and d , but the numerical coefficient was 0.016.

Srinivasan and Aiken (1988) developed a similar expression for mass transfer in closely spaced, well-mixed droplets soon after formation. Considering a stream of closely spaced droplets to be similar to a cylindrical jet, they also applied the Blasius correlation to obtain v_0 . The results were in reasonable agreement with the predicted dependence on Re , We , and Sc . However, the numerical factor was found to be 0.14.

3.1.4. Other turbulent models

Other models for mass transfer in turbulent flow exist in the literature. For example, Lamont and Scott (1970) proposed a relation between the mass transfer coefficient and the hydrodynamic behavior of turbulent eddies near the interface. The small dissipative eddy structures were assumed to control the mass transfer, so that k_L may be calculated from the rate of energy dissipation by turbulence per unit mass (ε).

$$k_L \propto (\varepsilon v)^{1/4} \left(\frac{v}{D} \right)^{-1/2} \quad (3.9)$$

Values for ε may be calculated for wetted walls (Prasher and Fricke, 1974) or for pipe flow (Lamont and Scott, 1970). Detailed velocity measurements can also be used to obtain ε from the definition

$$\varepsilon = -\frac{3}{2} \frac{\partial u^2}{\partial t} \quad (3.10)$$

Lamont and Scott applied this method to predict the mass transfer coefficient for a turbulent flow downstream of a grid in a wind tunnel. Alternatively, the following scaling analysis could be applied to estimate k_L .

$$\varepsilon \propto \frac{U_c^2}{\tau_c} \propto \frac{U_c^3}{L_c} \quad (3.11)$$

$$\frac{k_L}{U_c} \propto \frac{1}{U_c} \left(\frac{U_c^3}{L_c} v \right)^{1/4} \left(\frac{v}{D} \right)^{-1/2} \propto Re^{-1/4} Sc^{-1/2} \quad (3.12)$$

In addition to the model of Lamont and Scott, others such as the models of Levich-Davies and Fortescue and Pearson (1967) can be expressed in dimensionless form as shown below (George et al., 1994).

$$\frac{k_L}{U_c} \propto \text{Re}^a \text{We}^b \text{Sc}^c \quad (3.13)$$

According to George et al. (1994), the exponent on the Reynolds number (a) varies among the available models between $-1/2$, $-1/4$, and $1/2$. Many of the mass transfer models do not consider the effect of surface tension ($b = 0$). Only Levich and Davies propose a Weber number dependence of $1/2$. Most absorption models predict that k_L varies with the Schmidt number to the $-1/2$ power, although an exponent of $-2/3$ has been suggested when the interface resembles a wall (Amokrane et al., 1994).

The mass transfer coefficient is also commonly expressed in dimensionless form as the Sherwood number (Sh). Equation 3.13 can be rearranged to obtain an expression for Sh .

$$Sh = \frac{k_L}{U_c} \text{Re} \text{Sc} \propto \text{Re}^{a+1} \text{We}^b \text{Sc}^{c+1} \quad (3.14)$$

3.2. LIQUID SHEETS

As mentioned in the previous chapter, the liquid exiting a centrifugal spray nozzle forms a hollow conical sheet. The cone expands with distance, and the thickness of the sheet decreases. Although the contact time of the sheet is typically very small, significant mass transfer could occur in the sheet due to high k_L or interfacial area.

3.2.1. Sheet hydrodynamics

As a prelude to discussing mass transfer in the sheet, the fluid dynamics of the sheet should be understood. According to the idealized mechanism of Fraser et al. (1962), liquid sheets in gases at atmospheric pressure become wavy due to aerodynamic instabilities. The magnitude of the wavy disturbance grows and the sheet becomes even thinner, until ribbons of fluid detach from the sheet at each half wavelength (between the crests and troughs). The ribbons contract into cylindrical ligaments oriented perpendicular to the direction of flow. Finally, the ligaments break up according to the Rayleigh mechanism to form droplets.

3.2.1.1. Flow regimes

Fraser et al. (1962) observed the behavior of flat sheets using fan spray nozzles and flash photography. They determined that the flat sheets became semi turbulent at Re of 10,000 to 30,000 and fully turbulent at Re of 18,000 to 37,000 where Re was defined in terms of the hydraulic mean diameter at the orifice. However, the breakup length of the sheet did not change significantly even though the flow changed from laminar to turbulent conditions.

Chigier (1991) described flow through a two-dimensional liquid sheet airblast atomizer with and without airflow. The liquid exits the nozzle through a slit and forms a two dimensional sheet, which can be used to study wave growth and the frequency of disturbances on the liquid surface. In experiments at Re of 1470 without airflow, small distortions were observed on the sheet, and the flow changed from laminar to turbulent conditions.

3.2.1.2. Sheet breakup

The breakup of liquid sheets has been studied for many years by a variety of investigators. The sheet breakup process has been modeled with linear stability analysis by Dombrowski and Hooper (1962) and Dombrowski and Johns (1963). They presented predictions for the breakup of viscous sheets due to asymmetric disturbances. Dombrowski and Hooper proposed the following relationships.

$$\begin{aligned} L_b \left(\frac{\rho_g}{\rho_L} \right)^{3/2} &= 2.6 \ln \left(\frac{\eta_b}{\eta_o} \right) \frac{\sigma}{\rho_L U^2} && \text{for short waves} \\ \frac{L_b^2 \rho_g}{K \rho_L} &= 1.5 \ln \left(\frac{\eta_b}{\eta_o} \right) We_b^{1/2} \frac{We_b + 1}{(We_b - 1)^2} && \text{for long waves} \end{aligned} \quad (3.15)$$

where $We_b = \frac{\rho_L U^2 h_b}{\sigma}$

$$K = 2hx$$

The parameter K is a constant that relates the sheet thickness to the sheet length for the flat sheet. The ratio of the disturbance amplitude at breakup (η_b) to the

amplitude of the initial disturbance (η_o) was assumed constant. The $\ln(\eta_b/\eta_o)$ term was set equal to 12 to match experimental data for sheet breakup of flat sprays. This value was also based on previous work with liquid jets.

Senecal et al. (1999) extended the work of Dombrowski and Johns by relaxing assumptions inherent in the previous analysis. Senecal et al. modeled the sheet in two dimensions whereas Dombrowski and Johns considered variations in only one dimension. In addition, Senecal et al. relaxed the assumption that long wavelength disturbances were responsible for the breakup process and found different regimes for breakup by long waves and short waves. Long wavelength disturbances dominate the sheet breakup process for low gas phase Weber numbers, and short waves control for We_g greater than 27/16.

$$L_b = \left\{ \begin{array}{l} U_{abs} \left(3 \ln \left[\frac{\eta_b}{\eta_o} \right] \right)^{2/3} \left(\frac{J \rho_L \sigma}{\rho_g^2 U^4} \right)^{1/3} \quad \text{for long waves} \left(We_g < \frac{27}{16} \right) \\ \frac{U_{abs}}{\omega_{max}} \ln \left(\frac{\eta_b}{\eta_o} \right) \quad \text{for short waves} \left(We_g > \frac{27}{16} \right) \end{array} \right\}$$

where $J = ht = \frac{hx}{U_{abs}}$ (3.16)

$$\omega_{max} = \max \left(-2v_L k^2 + \sqrt{4v_L^2 k^4 + \frac{\rho_g}{\rho_L} U^2 k^2 - \frac{\sigma k^3}{\rho_L}} \right)$$

For the long wave regime, the growth rate (ω) varies as the sheet thickness changes, and an integration over time is performed. The sheet was approximated by assuming the time and the sheet thickness were related by a constant J. The growth rate is a function of the wave number of the disturbance, and the wave with the greatest growth rate controls the breakup in the short wave regime. Then, the breakup length is determined by the absolute velocity of the sheet (U_{abs}) and the time required for the disturbance to grow. Based on the work of Dombrowski and Hooper, Senecal et al. also assumed that the $\ln(\eta_b/\eta_o)$ term was equal to 12.

Analyses that are more complex have also been performed in recent years. Ibrahim (1998) applied a second order nonlinear perturbation analysis to the breakup process. The nonlinear analysis verified that the sheet disintegrates into ligaments at each half wavelength. Nonnenmacher and Piesche (2000) performed computational fluid dynamic (CFD) simulations for spray atomization assuming laminar flow in the nozzle and in the sheet.

3.2.2. Sheet mass transfer

Hasson et al. (1964) developed a model for diffusive heat transfer in a laminar fan spray sheet. Making the analogy between heat and mass transfer, Simpson and Lynn (1977) restated Hasson's model in this form.

$$\frac{C_{in} - C}{C_{in} - C^*} = 1 - \frac{8}{\pi^2} \sum_{n=1}^{\infty} \frac{1}{(2n-1)^2} \exp[-\lambda_n^2 \zeta]$$

where $\lambda_n = \frac{\pi}{2}(2n-1)$ (3.17)

$$\zeta = \frac{4 D x^3 \phi U}{3 Q_L^2}$$

ϕ = flat spray angle

The predictions of this model were tested for flat spray nozzles by Tamir and Rachmilev (1972) and Simpson and Lynn (1977). Simpson and Lynn also attempted to apply the model to centrifugal spray nozzles, but the applicability of the model was hindered by turbulent flow conditions. They correlated their results by introducing effective diffusion coefficients of 10 times the molecular value. Demyanovich (1991) also applied the Hasson model to liquid sheets formed by the impingement of two individual sheets. The collision of the two sheets led to turbulent mixing, and effective diffusion coefficients of 5 to 167 times the molecular value were used to correlate the data.

3.2.3. Sheet model

The linear stability models qualitatively describe the sheet breakup for the spray nozzles in this work, but quantitatively the models tend to over-predict the sheet breakup length (L_b). Therefore, as in the work of Simpson and Lynn, empirical observations of the sheet breakup length are used in the present model.

3.2.3.1. Sheet k_L

Simpson and Lynn also demonstrated that a fundamental diffusion model accurately described the mass transfer in a flat laminar sheet. However, in this work, the Reynolds number for the sheet at the nozzle exit is high enough that the flow could be turbulent. In order to model turbulent sheets for their centrifugal nozzles, Simpson and Lynn empirically determined effective diffusion coefficients. The turbulent flow of the sheet complicates the modeling of mass transfer, but if k_L , area, and contact time can be predicted separately, then Equation 1.8 may be used to determine the N_L of the sheet.

Instead of relying on a completely empirical effective diffusion coefficient, the k_L is calculated by one of the models for turbulent mass transfer. The Levich-Davies model for turbulent jets was selected as a predictive model. If the turbulent jet model is modified by including an empirical factor of 3.0, the resulting model for the sheet k_L better matches the experimental data in this work.

3.2.3.2. Sheet area

The area of the sheet can be calculated, knowing the nozzle geometry and flow properties, if a few assumptions are made.

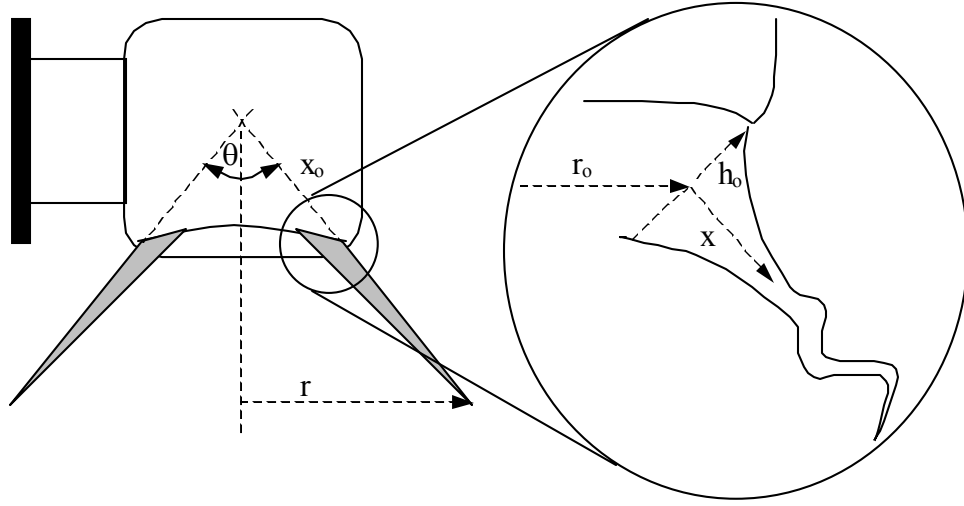


Figure 3.2. Calculation of sheet area

The cross-sectional area of the sheet is a function of the sheet half-thickness (h) and given by

$$A_{cs} = \frac{Q_L}{U} = 2\pi r(2h) \quad (3.18)$$

At the nozzle exit ($x = 0$),

$$r_o = \frac{d_{or}}{2} - h_o \cos\left(\frac{\theta}{2}\right) \quad (3.19)$$

Combining Equations 3.18 and 3.19 gives, at the nozzle exit,

$$\frac{Q_L}{U_o} = 4\pi h_o \left(\frac{d_{or}}{2} - h_o \cos\left[\frac{\theta}{2}\right] \right) \quad (3.20)$$

This equation is quadratic in h_o and can be solved analytically. Physically, the sheet thickness has to be less than the radius of the orifice. For only one of the solutions is $2h_o < d_{or}/2$. Therefore, the initial sheet half-thickness is

$$h_o = \frac{d_{or}}{2 \cos\left(\frac{\theta}{2}\right)} \left(1 - \sqrt{1 - \frac{4Q_L \cos\left(\frac{\theta}{2}\right)}{U_o \pi d_{or}^2}} \right) \quad (3.21)$$

Since the sheet experiences little frictional resistance from the gas phase, the sheet velocity U_o is assumed constant and given by

$$U_o = \sqrt{2\Delta P/\rho_L} \quad (3.22)$$

Since U_o is constant and the liquid can be considered incompressible, the cross-sectional area for flow is constant and h must decrease with distance from the nozzle.

$$h = \frac{A_{cs}}{4\pi r} = \frac{Q_L/U_o}{4\pi(x_o + x)\sin(\frac{\theta}{2})} \quad (3.23)$$

The surface area of the sheet can be related to the length along the sheet surface in the x direction. The waviness of the sheet is neglected in the following analysis. Recalling that the sheet has both a top and a bottom surface, the rate of change of surface area with distance from the nozzle is

$$\frac{dA_i}{dx} = 2 \cdot 2\pi r \frac{ds}{dx} = 4\pi \left[(x_o + x)\sin\left(\frac{\theta}{2}\right) \right] \left[1 + \left(\frac{dh}{dx}\right)^2 \right]^{1/2} \quad (3.24)$$

Differentiating Equation 3.23 gives

$$\frac{dh}{dx} = \frac{Q_L/U_o}{4\pi\sin(\frac{\theta}{2})(x_o + x)^2} - 1 \quad (3.25)$$

From Equation 3.25, the magnitude of dh/dx is the greatest at the nozzle exit ($x = 0$). Noting that

$$x_o = \frac{r_o}{\sin(\frac{\theta}{2})} \quad (3.26)$$

Then, the rate of change of the sheet half-thickness (h) with distance (x) was calculated to be small ($\sim 10^{-2}$) for the nozzles used in this work so that

$$1 + \left(\frac{dh}{dx}\right)^2 = 1 + \left(\frac{Q_L/U_o}{4\pi\sin[\frac{\theta}{2}]}\right)^2 \left(\frac{1}{x + x_o}\right)^4 \approx 1 \quad (3.27)$$

This simplification linearizes the calculation and allows an analytical integration to give the area of the sheet. Since the volume of liquid contained in the sheet is given by the flow area multiplied by the sheet length, the area per unit volume of the sheet can be calculated.

$$A_s = 4\pi \left(r_o x + \frac{x^2}{2} \sin \left[\frac{\theta}{2} \right] \right) \quad (3.28)$$

$$a_s = \frac{A_s}{\left(\frac{Q_L}{U_o} \right) x} = \frac{2\pi U_o}{Q_L} \left(d_{or} - 2h_o \cos \left[\frac{\theta}{2} \right] + x \sin \left[\frac{\theta}{2} \right] \right) \quad (3.29)$$

3.2.3.3. *Sheet N_L*

At the point where the sheet breaks into droplets, x is L_b . Since the sheet velocity is constant, the contact time is calculated by dividing the sheet length by the velocity. Thus, the overall k_L , a , and t of the sheet are determined, and Equation 1.8 simplifies to give the sheet N_L .

$$N_{Ls} = \ln \left(\frac{C_{in}}{C_b} \right) = k_{Ls} a_s \frac{L_b}{U_o} \quad (3.30)$$

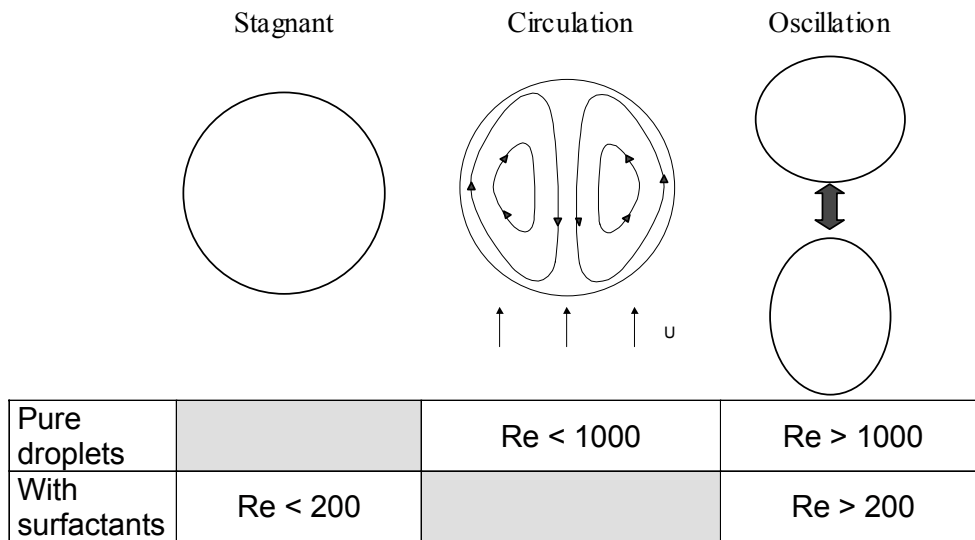
3.3. SINGLE DROPLETS

Relatively little literature is available on liquid phase mass transfer in spray systems. However, several models have been developed for mass transfer in a single droplet of liquid. The main difference between the models is in the assumed droplet hydrodynamics and mechanism of mass transfer.

3.3.1. Droplet hydrodynamics

3.3.1.1. *Flow regimes*

Liquid droplets can exhibit different types of flow behavior: stagnant, circulating, or oscillating (Figure 3.3). The stagnant droplet is the simplest case, for which there is no motion of the surface or in the interior of the droplet. Circulation arises because when a droplet moves through another fluid the relative velocity results in shear forces at the interface. The liquid at the interface is swept to the rear of the droplet, and a circulation pattern can then develop.



(Criteria for transitions taken from Clift, et al., 1978)

Figure 3.3. Regimes of droplet behavior

Circulation streamlines for a fluid sphere in creeping flow ($Re \sim 0$) were calculated by Hadamard (1911) and Rybczynski (1911). For flow conditions at finite Re , numerical solutions of the Navier-Stokes equation can be performed to obtain the flow field inside a circulating spherical or spheroidal droplet (Caussade and Saboni, 1990; Amokrane and Caussade, 1999; Piarah et al., 2001). These calculations assumed droplets of constant shape and therefore are not applicable to oscillating droplets.

The droplet can also deform due to pressure forces around the droplet in the continuous phase. Any pressure variations that result from turbulent velocity fluctuations or wake shedding can give rise to droplet shape oscillations. These oscillations can also induce internal circulation. The streamlines for small spherical harmonic oscillations of an inviscid droplet were derived by Lamb (1945) and discussed by Hughes and Gilliland (1952). Numerical simulation has recently been employed to describe large oscillations of viscous droplets with internal circulation (Mashayek and Ashgriz, 1998).

3.3.1.2. Flow transitions

The onset of steady droplet oscillation depends on several factors, most notably the droplet Reynolds number and the presence or absence of surfactants (Clift et al., 1978). In pure systems, small water droplets falling in air are spherical and may exhibit circulation. Larger droplets deform into an ellipsoid and continue circulating. For even larger droplets, oscillation begins when Re reaches values on the order of 1000. In contaminated systems, the presence of surfactants inhibits circulation, thereby significantly increasing drag and decreasing mass transfer rates. The shear force at the interface is believed to sweep the surfactants to the rear of the droplet and result in a surface concentration gradient. The resulting surface tension gradient exerts a Marangoni force along the interface, which opposes the shear force, inhibits circulation, and increases drag. Spherical and ellipsoidal drops with surfactants remain stagnant until oscillation begins at Re of about 200. This Re is the minimum necessary for vortex shedding from the wake of the droplet (Schroeder and Kintner, 1965). Surfactants may also decrease the magnitude of droplet oscillation (Clift et al., 1978).

Other criteria have also been proposed for the transition from droplet circulation to oscillation. Correlations by Klee and Treybal (1956), Hu and Kintner (1955), Johnson and Braida (1957), Edge and Grant (1971), and Grace et al. (1976) were discussed by Skelland et al. (1987) and are shown in Appendix B. These correlations were developed for a liquid droplet moving at terminal velocity through another liquid phase, and they may not be easily extrapolated to the case of liquid droplets in a gas. In any case, for an air-water system, these correlations predict the critical droplet size for steady oscillations to be about 1700 μm .

3.3.1.3. Oscillation frequency

The time scale of oscillations may be estimated from the natural frequency for the oscillation of liquid droplets derived by Lamb. For spherical harmonic oscillations with small amplitude, Lamb calculated the frequency for each harmonic

mode. The most important mode is the oscillation between an oblate spheroid and a prolate spheroid, and the corresponding time scale is given below.

$$\tau_{\text{osc}} = \frac{\pi}{4} \sqrt{\frac{(\rho_L + \frac{2}{3}\rho_g)d^3}{\sigma}} \quad (3.31)$$

Since the liquid density is much greater than the gas density,

$$\tau_{\text{osc}} = \frac{\pi}{4} \sqrt{\frac{\rho_L d^3}{\sigma}} \quad (3.32)$$

According to this relationship, the period for the natural mode of oscillation of a 1000 μm water droplet in air is 2.9 ms. Schroeder and Kintner conducted experiments to observe droplet oscillation in several liquid-liquid systems and proposed a modification to Lamb's derivation that takes into account the amplitude of the oscillation. If the dispersed phase is denoted by L and the continuous phase by g, then their equation is

$$\tau_{\text{osc}} = \frac{\pi}{4} \sqrt{\frac{(\rho_L + \frac{2}{3}\rho_g)d^3}{b\sigma}} \quad (3.33)$$

where $b = 1 - \frac{d_{\text{max}} - d_{\text{min}}}{2d_{\text{avg}}}$

For very small oscillations, the parameter b approaches one and Equation 3.33 approaches Equation 3.31. Unfortunately, this data is not usually known and is difficult to measure. Schroeder and Kintner found that the frequency of oscillation was very consistent, but the amplitudes were very erratic. In order to use Equation 3.33 to predict the oscillation frequency, they correlated their amplitude data empirically as follows.

$$b = 0.805d^{0.225} \quad (3.34)$$

A theoretical development by Subramanyam (1969) included the effects of the surface tension and the viscosities of the two phases. However, since the density and viscosity ratios between the two phases are so large, Subramanyam predicted a very small deviation from Lamb's time constant.

3.3.1.4. Oscillation damping constant

The effect of viscosity in the droplet is primarily to dampen the magnitude of oscillations. In the linear analysis of small oscillations, viscosity does not affect the frequency of oscillations, only their amplitude. According to Lamb, the time scale for viscous damping of oblate-prolate oscillations can be expressed as follows.

$$\tau_{\text{dmp}} = \frac{\mu d^2}{20\rho} \quad (3.35)$$

When droplets are formed, the breakup process often results in shape oscillations, which are then damped by viscous forces. Immediately after formation, the droplet is non-spherical, and surface tension tends to pull it into a spherical shape. Inertia prevents the fluid from stopping at the spherical state, and oscillations begin. The frequency of the oscillation is expected to be that predicted by Lamb, and the magnitude of the oscillation decays exponentially as $\exp(-t/\tau_{\text{dmp}})$ until the droplet reaches its steady state behavior. Since the oscillations at high Re are driven by vortex shedding, these oscillations are not completely damped out, and they persist at steady state (Schroeder and Kintner, 1965).

Deviations from the theoretical damping constant may occur if significant eddying motion occurs within the droplet. The eddying would increase the rate of energy dissipation and increase the rate of amplitude decrease (Hughes and Gilliland, 1955).

3.3.2. Droplet mass transfer

For stagnant drops, k_L may be calculated purely by solving the diffusion equation. The presence of circulation within the drop increases the mass transfer rate compared to diffusion alone. If the droplet is oscillating and these oscillations are strong enough to mix the contents of the drop, the internal resistance to mass transfer will become constant. Drop oscillation increases the mass transfer coefficient compared to a non-oscillating drop.

Most of the models for mass transfer in droplets were developed for liquid-liquid extraction systems. However, for a liquid droplet falling through air, the large differences in the densities and viscosities of the two phases may result in much higher terminal velocities and different flow regimes. For a given droplet size, the motion of droplets in extraction may be dominated by circulation, whereas oscillation may be more important at the high drop velocities found in gas-liquid systems (Clift et al., 1978).

Table 3.1. Models for k_L in droplets

Stagnant	Higbie (1935) penetration theory (short times)	$k_L = 2\sqrt{\frac{D}{\pi t}}$
	Stagnant diffusion (long times)	$Sh \rightarrow \frac{2\pi^2}{3} \approx 6.58$
Circulating	Steady circulation (Kronig and Brink, 1950)	$Sh \rightarrow 17.66$
	Handlos and Baron (1957)	$k_L = \frac{0.00375 U}{1 + \frac{\mu_L}{\mu_g}}$
	Ruckenstein (1967)	$k_L = 2\sqrt{\frac{DU}{\pi d}}$
	Laddha and Degaleesan (1978)	$k_L = \frac{0.023 U}{Sc_L^{0.5}} = 0.023 U \sqrt{\frac{\rho_L D}{\mu_L}}$
	Local model (Amokrane et al., 1994)	$k_L = \omega \sqrt{\frac{Du_*}{d}}$ $u_* = \sqrt{\frac{\tau}{\rho_L}} = U \sqrt{\frac{c_f \rho_g}{2\rho_L}}$
Oscillating	Angelo et al. (1966)	$k_L = 2\sqrt{\frac{D}{\pi\tau_{osc}} \left(1 + \alpha + \frac{3\alpha^2}{8}\right)}$

3.3.2.1. Stagnant diffusion

For stagnant drops, the diffusion equation can be solved to obtain the concentration and the mass transfer coefficient as a function of time.

$$\frac{C_o - C}{C_o - C^*} = 1 - \frac{6}{\pi^2} \sum_{n=1}^{\infty} \frac{1}{n^2} \exp\left[-n^2 \pi^2 \left(\frac{4Dt}{d^2}\right)\right] \quad (3.36)$$

$$\text{Sh} = \frac{2\pi^2}{3} \sum_{n=1}^{\infty} \exp\left[-n^2 \pi^2 \left(\frac{4Dt}{d^2}\right)\right] / \sum_{n=1}^{\infty} \frac{1}{n^2} \exp\left[-n^2 \pi^2 \left(\frac{4Dt}{d^2}\right)\right] \quad (3.37)$$

For short contact times, penetration theory may be used to predict k_L from pure diffusion. For long contact times, an analytical solution for the Sherwood number asymptotically approaches a value of 6.58.

3.3.2.2. *Steady circulation*

Kronig and Brink assumed that the circulation rate within the drop was steady and much faster than the mass transfer rate so that the concentration profiles in the drop followed the circulation streamlines. The diffusion-convection equation can be solved to obtain

$$\frac{C_o - C}{C_o - C^*} = 1 - \frac{3}{8} \sum_{n=1}^{\infty} A_n^2 \exp\left[-16\lambda_n \left(\frac{4Dt}{d^2}\right)\right] \quad (3.38)$$

$$\text{Sh} = \frac{32}{3} \sum_{n=1}^{\infty} A_n^2 \lambda_n^2 \exp\left[-16\lambda_n \left(\frac{4Dt}{d^2}\right)\right] / \sum_{n=1}^{\infty} A_n^2 \exp\left[-16\lambda_n \left(\frac{4Dt}{d^2}\right)\right] \quad (3.39)$$

This model for circulation results in a mass transfer rate about 2.5 times the rate of diffusion into a stagnant sphere and an asymptotic Sh of 17.66. Although the Kronig and Brink model was derived for a sphere in creeping flow, it is still a good approximation for circulating ellipsoidal drops that do not oscillate (Clift et al., 1978).

3.3.2.3. *Turbulent circulation*

The models of Handlos and Baron, Ruckenstein et al., and Laddha and Degaleesan are used to correlate mass transfer in circulating droplets in liquid-liquid extraction. Amokrane et al. advocated using the interfacial friction velocity instead of the relative velocity of the droplet as the appropriate velocity scale. Using experimental data and drag correlations for water droplets in air, they determined their empirical parameter ω to be 0.8.

3.3.2.4. Oscillation

Angelo et al. generalized the penetration theory to account for surface deformations. Their oscillation model assumes that the surface area of the droplet oscillates sinusoidally and that the contents of the droplet mix completely after each oscillation. The mass transfer coefficient can then be calculated from the frequency and magnitude of the oscillation. The theoretical natural frequency for droplet oscillation derived by Lamb was used. The magnitude of the oscillation is typically difficult to measure or predict. However, at typical values of 0.3, the magnitude does not greatly impact the prediction of the Angelo oscillation model so it can be neglected (Hsu and Shih, 1993).

3.3.2.5. Mass transfer data

Figure 3.4 compares model predictions with the data in the literature for mass transfer in droplets. Usually, the mass transfer during droplet formation was not included, and the data are for droplets falling in air at or below their terminal velocities. Walcek et al. (1984) studied the absorption of SO₂ into water droplets falling through air at terminal velocity. Droplets smaller than 1000 μm in diameter exhibited steady circulation and followed the Kronig and Brink model, but larger droplets showed unsteady flow and mass transfer greater than predicted. Garner and Lane (1959) also reported CO₂ absorption rates much higher than Kronig and Brink predictions for 4220 and 5850 μm drops.

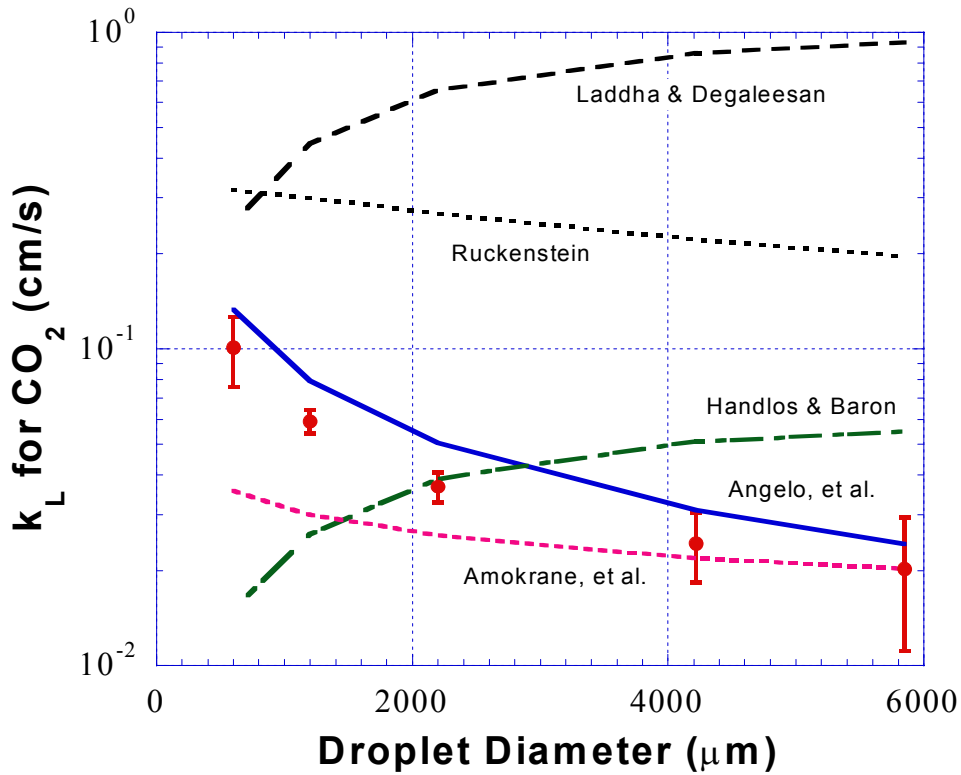


Figure 3.4. Comparison of data and model predictions for k_L in droplets

Kaji et al. (1985) also used SO_2 to study absorption into 2200 μm drops. Single droplets were formed with a hypodermic needle and allowed to fall through an absorption chamber. The calculated mass transfer coefficient for the droplet decreased slightly as the drop fell through the absorption chamber. The formation of the drop was hypothesized to produce a high circulation rate, which was then quickly damped by viscous forces within the droplet. For 600 and 1200 μm droplets, Altwicker and Lindhjem (1988) obtained results for CO_2 absorption and found that the mass transfer coefficient remained approximately constant despite gravitational acceleration. Hughes and Gilliland observed that the droplet mass transfer coefficient decayed with time according to Lamb's time constant for viscous damping.

For single droplets falling in gases, the Ruckenstein model and the Laddha and Degaleesan model overestimate the mass transfer coefficient for drop diameters

between 600 and 6000 μm . The Handlos and Baron model predicts that k_L increases with drop diameter, because the terminal velocity of the droplet increases with drop size. However, the data suggest the opposite relationship between k_L and drop size. Both the models of Angelo and Amokrane qualitatively fit the data much better, although the Amokrane model predicts lower mass transfer than observed for drop sizes less than about 4000 μm . The drop oscillation model of Angelo slightly overestimates the mass transfer for all drop sizes and values of α (the magnitude of the oscillation). Hsu and Shih (1993) noted that the Angelo model was relatively insensitive to α . The accuracy of the model was improved if α was set to zero, and the oscillation frequency was half of that predicted by Lamb.

3.3.3. Droplet model

Hughes and Gilliland studied hydrodynamics and mass transfer for water droplets and found that after drop formation the mass transfer coefficient decayed exponentially, consistent with Lamb's time constant for viscous damping of oscillations. These relationships are combined to model the mass transfer coefficient of droplets soon after formation.

$$k_{Ld} = k_{Ldo} - (k_{Ldo} - k_{Ldf}) \left(1 - \exp\left[-t/\tau_{\text{dmp}}\right] \right) \quad (3.40)$$

$$k_{Ldf} = 2 \sqrt{\frac{D}{\pi\tau_{\text{osc}}}} \left(1 + \varepsilon + \frac{3\varepsilon^2}{8} \right) \approx 2 \sqrt{\frac{D}{\pi\tau_{\text{osc}}}} \quad (3.41)$$

The liquid phase mass transfer coefficient of the droplet immediately after formation (k_{Ldo}) may be assumed or set equal to the mass transfer coefficient of the sheet (k_{Ls}). The mass transfer coefficient then decays exponentially to the steady state value (k_{Ldf}) for droplet oscillation.

The area per unit volume of a spherical droplet is $6/d$. The droplet diameters under each set of operating conditions were obtained or interpolated from data provided by the nozzle manufacturer (Appendix A). If droplet coalescence and secondary breakup are neglected, the droplet diameter and, therefore, the area per unit

volume are constant. The contact time of the droplet is determined by a drag calculation, given the initial velocity of the droplet and its diameter. A numerical integration is performed to obtain the total N_L for the spray as a function of time. Since the droplet trajectory is also determined from the drag calculation, the spray N_L may be given as a function of distance and compared with experimental data.

$$N_{Ld} = \ln\left(\frac{C_b}{C_{out}}\right) = \frac{6}{d} \int_{t_b}^t k_{Ld} dt' \quad (3.42)$$

3.4. SUMMARY

The spray is modeled by considering the sheet and droplets separately. The sheet mass transfer coefficient is predicted using the Levich-Davies turbulence model. Alternatively, other similar correlations for Sh as a function of Re, We, and Sc may be used to calculate k_{Ls} . The area of the sheet is estimated based on the nozzle geometry, and the contact time is determined by the nozzle pressure drop and the sheet length.

The droplet k_L is calculated using a model based on the Angelo et al. oscillation model and decays according to Lamb's theoretical time constant as discussed by Hughes and Gilliland. The area of the droplet is given by the droplet size data, which is readily available from the nozzle vendor. Lastly, the contact time of the droplet can be determined from a drag calculation.

Thus, the mass transfer coefficients, interfacial areas, and contact times are calculated and combined to obtain the N_L of each region of the spray. Adding the N_L for the sheet and the droplets gives the total N_L for the spray.

$$N_L = N_{Ls} + N_{Ld} = k_{Ls} a_s \frac{L_b}{U_o} + \frac{6}{d} \int_{t_b}^t k_{Ld} dt' \quad (3.43)$$

Chapter 4: Experimental Methods

One of the major challenges of this research was to develop the experimental methods necessary to measure the mass transfer in sprays. As a result, much of the work entailed design and construction of equipment, development of the sample collection system, and validation of the experimental methods.

4.1. BASIS AND RATIONALE

Desorption of carbon dioxide (CO_2) in an air-water system was used to study the liquid phase resistance to mass transfer. The water was buffered at a pH of 4.5 with a citric acid/sodium citrate solution. The low pH ensured that the CO_2 remained as CO_2 and was not converted to bicarbonate or carbonate ion, which would not contribute to the mass transfer driving force.

Desorption was used as opposed to absorption so that more precise measurements could be taken. For large values of N_L , the system would approach equilibrium, and the mass transfer driving force for absorption would be low compared to the CO_2 concentration. Thus, for absorption, the driving force would become difficult to compute with precision since it would be the difference between two relatively large numbers.

The direction of mass transfer was not expected to have a significant effect on the mass transfer performance. In liquid-liquid extraction, transfer from the dispersed to the continuous phase can lead to gradients in the interfacial tension and can promote coalescence (Seibert and Fair, 1988). However, the aqueous concentrations of CO_2 in the present work were low and expected to have little effect on the air-water surface tension. In addition, coalescence was not expected to be as significant in the conical section of the spray (where the droplet trajectories tend to diverge) as it might be in a packed liquid-liquid extractor.

4.1.1. Liquid phase controlled mass transfer

The low solubility of CO₂ in water tends to favor liquid phase control of the mass transfer. As an order of magnitude approximation of the significance of gas side resistance, estimates of the mass transfer coefficients and the Henry's Law coefficient may be compared. The expression for the overall mass transfer coefficient can be manipulated to obtain the fractional gas side resistance, shown below.

$$\frac{K_G}{k_g} = \left(1 + \frac{H_{CO_2}}{E \cdot k_L^o / k_g} \right)^{-1} \approx 0.0078$$

where $H_{CO_2} = 25.6 \frac{\text{atm}}{\text{M}}$ at 20°C (Liley et al., 1984) (4.1)

$E = 1$ for CO₂ - water at pH = 4.5

$k_L^o / k_g \approx 200 \frac{\text{atm-cm}^3}{\text{mol}}$ (DeVincentis, 1998)

Thus, for the CO₂-air-water system, the gas phase mass transfer resistance is expected to contribute only 0.78% of the total resistance, and the mass transfer is over 99% liquid phase controlled.

Since the solubility of CO₂ is low, the concentration change in the gas phase also tends to be low. Thus, measurements of the liquid phase concentration are necessary to calculate the mass transfer performance with precision. Accurate liquid phase measurements require that representative, reproducible samples of the spray be collected. The liquid in the spray moves at high velocity (~10 m/s) and entrains surrounding gas. An ideal sample collection method would be able to decelerate the liquid and separate the gas without providing any extra opportunities for mass transfer. Addressing this problem is the subject of Section 4.5.

4.1.2. Equilibrium limitations

Pure CO₂ gas was sparged into the water feed to the nozzle. The target liquid concentrations of CO₂ were low to ensure that all of the gas dissolved in the piping before reaching the spray nozzle. The CO₂ concentrations at the nozzle inlet were about 2.0 mM, low compared to equilibrium with one atmosphere of pure CO₂ (39 mM at 20°C) to avoid spontaneous evolution of CO₂ bubbles in the piping or across

the nozzle. The inlet to the spray column did not have to be saturated to pure CO₂, as long as the analytical methods were precise enough to measure the CO₂ desorption. However, the CO₂ concentration had to be high enough to avoid approaching equilibrium with air. If a large number of liquid phase transfer units were observed, then a higher inlet concentration would have been necessary to avoid approaching equilibrium with CO₂ in ambient air (~300 ppm).

If the desorption of CO₂ does not approach equilibrium, then the ambient concentration of CO₂ can be neglected. At 20°C, air with 300 ppm CO₂ would be in equilibrium with a liquid concentration of 0.0117 mM. The concentration of CO₂ in the liquid outlet had to be significantly greater in order to avoid equilibrium limitations. For example, if the outlet concentration were 0.25 mM, then the error associated with neglecting the gas concentration in the calculation of the mass transfer driving force would be

$$\frac{C - (C - C^*)}{C - C^*} = \frac{C^*}{C - C^*} \approx \frac{0.0117}{0.25 - 0.0117} = 4.9\% \quad (4.2)$$

Experiments were conducted with approximate inlet concentrations of 2 mM CO₂. For N_L values less than 2.1, the outlet concentration is greater than 0.25 mM, and the error from neglecting the ambient CO₂ is less than 5%.

4.1.3. Calculation of N_L

If the mass transfer is liquid phase controlled and does not approach equilibrium, then the calculation of N_L is straightforward since the CO₂ concentration in air is low.

$$N_L = \frac{C_{A,out} - C_{A,in}}{(C_{Ai} - C_A)_{lm}} \approx \ln \left(\frac{C_{A,in}}{C_{A,out}} \right) \quad (4.3)$$

since $C_{Ai} \approx C_A^* \ll C_A$

The liquid phase concentrations were measured at the inlet to the nozzle and at various positions in the spray. Using these concentrations, the number of liquid phase transfer units (N_L) was calculated as a function of distance from the nozzle.

However, the calculation of k_L is complicated by the fact that the interfacial area and the liquid holdup of the spray are difficult to measure. Average values for k_L are normally calculated from the superficial liquid velocity, Sauter mean droplet diameter, and fractional holdup. Unfortunately, separating k_L from A_i for a spray is more complicated, especially close to the nozzle (see Appendix C). The Sauter mean droplet diameter can be measured (e.g. photographically), but determining the holdup is more difficult. Calculating holdup may require measurements or estimates of the droplet velocities.

4.2. DESCRIPTION OF APPARATUS

Data in the literature suggest that the relative velocity of droplets does not have a significant effect on the liquid mass transfer (Altwicker and Lindhjem, 1988; Kaji et al., 1985). In addition, since the velocity of the spray can be as high as 40 ft/s, the gas velocity contributes little to the relative velocity of the drops. If high gas velocity is not required, then the gas flow rate only has to be sufficient to prevent CO₂ from accumulating in the gas phase and decreasing the mass transfer driving force.

Liquid samples were collected immediately upstream of the nozzle to measure the CO₂ concentration entering the spray column. Since the nozzle flow rate is a function of pressure drop across the nozzle, the nozzle pressure was monitored and used to control the flow rate of water. The CO₂ desorbed from the spray, and then the water and any residual CO₂ was recycled.

4.2.1. Nozzles

The spray nozzles used in these experiments were centrifugal hollow cone nozzles, manufactured by the Spraying Systems Company. Some of the important nozzle properties are listed in Table 4.1, and additional data may be found in Appendix A. The nozzle designations indicate the inlet pipe size, nozzle style, material, and capacity. For example, the 1/8-A-SS-5 nozzle has a 1/8 inch pipe connection, is one of the Spraying Systems A series WhirlJet nozzles, is constructed of stainless steel, and has a capacity of 0.5 gpm at 10 psi nozzle pressure.

Table 4.1. Nozzle properties (data provided by the Spraying Systems Company)

Nozzle	d_{or} (inches)	Q_n (gpm)*	$d_{v0.5}$ (μm)*	θ ($^\circ$)**
1/8-A-SS-0.5	3/64	0.05	365	58
1/8-A-SS-2	5/64	0.2	435	61
1/8-A-SS-5	1/8	0.5	500	67
1/4-A-SS-10	11/64	1.0	645	70
3/8-A-SS-20	1/4	2.0	910	70
3CF-SILCNB-120	2 1/16	143	1670	73

* At a nozzle pressure drop of 10 psi

** At a nozzle pressure drop of 20 psi

The liquid enters the nozzle tangentially and forms a vortex in the hollow chamber of the nozzle before exiting through the orifice as a thin, conical sheet (Figure 4.1). The sheet thins and disintegrates as described in the previous chapters to form the spray droplets.

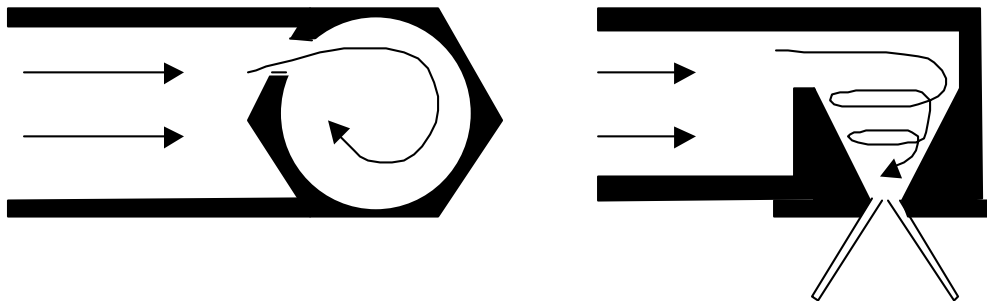


**Figure 4.1. Centrifugal hollow cone nozzle operation
(Spraying Systems A-series WhirlJet nozzles)**

In experiments using spray nozzles, the mass transfer performance of the spray could not be easily measured because the spray mass transfer could not be distinguished from mass transfer due to sample collection. The measured mass transfer could be extrapolated to zero distance to estimate the sampling effect, but high mass transfer rates near the nozzles made this difficult. In addition, this approach would have neglected variations in the sample collection effect with distance from the nozzle.

For measurements of mass transfer during sample collection, liquid jets were used for the most part, instead of spray nozzles. The jets had less interfacial area ($a_L = 4/d_{\text{jet}}$) and therefore slower mass transfer rates. In addition, since the jets did not thin or breakup as soon as sheets did, the simpler fluid mechanics of the jet also made extrapolating mass transfer data to zero distance much simpler for jets than for sprays.

Jet orifices for the sampler characterization experiments were prepared by drilling holes of known diameter in ¼ inch Swagelock® cap fittings (model SS-400-C). The jet orifices had diameters from 1/64 to 1/16 inch, and the thickness of the fittings were 0.227 inches. Therefore, the orifices had length to diameter ratios of 14.5 to 3.6. During initial sampler characterization experiments, the jet length (as measured from the orifice to the top of the sampler) was varied between 0 and 10 inches, and the N_L of the jet was extrapolated back to zero distance to determine the sampler N_L . However, over this range of jet lengths, the N_L of the jet typically changed by about 0.15 transfer units, which was only slightly more than the experimental error. Therefore, in later experiments, shorter jet lengths (0 – 1 inch) were used, and the N_L of the jet was neglected.

4.2.2. Laboratory contactor

The laboratory spray contactor consisted of a clear acrylic tank (3' x 4' x 2') and a sampling arm. (Figure 4.2) The piping was constructed with ½ inch schedule 80 PVC pipe and fittings. Pump 1 was a 3.5 gpm diaphragm pump (ITT Jabsco model 30801-0115), which circulated water through the system and delivered the liquid to the spray nozzle. The water in the experiment was buffered at a pH of 4.5 using a 5 mM citric acid/sodium citrate solution to ensure that all of the bicarbonate (HCO_3^-) and carbonate (CO_3^{2-}) species were converted to dissolved CO_2 .

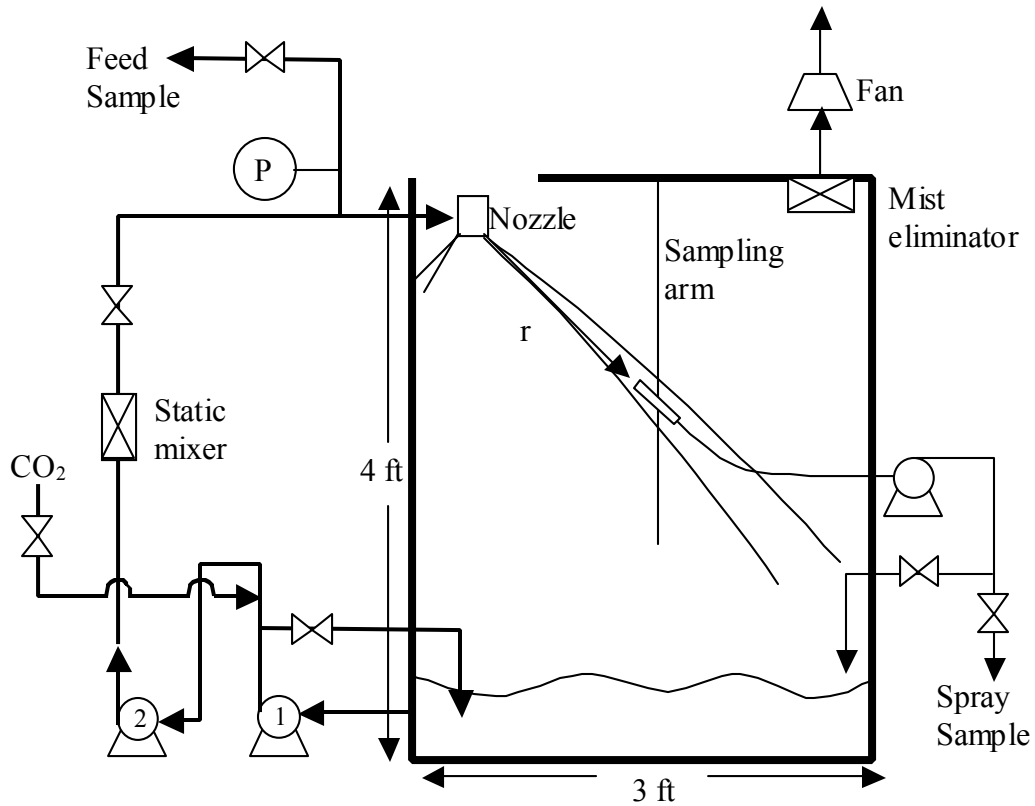


Figure 4.2. Laboratory spray contactor

Figure 4.3 shows more details of the piping of the spray nozzle. A ½ inch PVC tee was installed upstream of the nozzle. The differential between the liquid pressure at the tee and atmospheric pressure was monitored with a Validyne DP15-42 pressure transducer and a CD379-1-2 digital readout. The feed sample line made of ¼ inch polypropylene tubing was also connected to the tee, and the flow rate through the sample line was controlled with a needle valve.

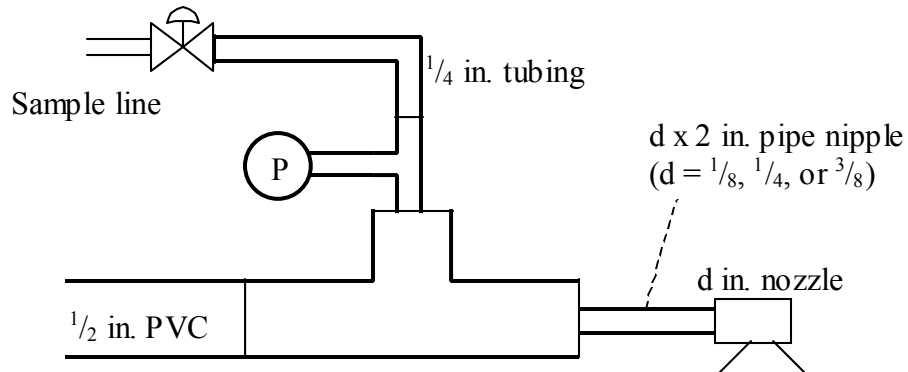


Figure 4.3. Nozzle piping in the laboratory contactor

At the other branch of the tee, the pipe size was changed from 1/2 inch to the nozzle size (1/8, 1/4, or 3/8) using a reducing bushing. A 2 inch pipe nipple connected the nozzle to the feed piping. The CO₂ solution was sprayed into the contactor, and samples of the spray were collected as a function of distance from the nozzle. Several designs for the spray sample collection device are discussed later in Section 4.5.

The top of the contactor (Figure 4.4) was covered except for a section by the nozzle. During operation, the spray coming out of the nozzle entrained air into the contactor through this opening. Air filter media (NaturalAire Cut-to-fit) was used to cover the narrow opening where the sampling arm could be moved closer or farther from the nozzle. The gas passed through a mist eliminator made of the same air filter media, and fan on top of the apparatus swept gas out of the contactor.

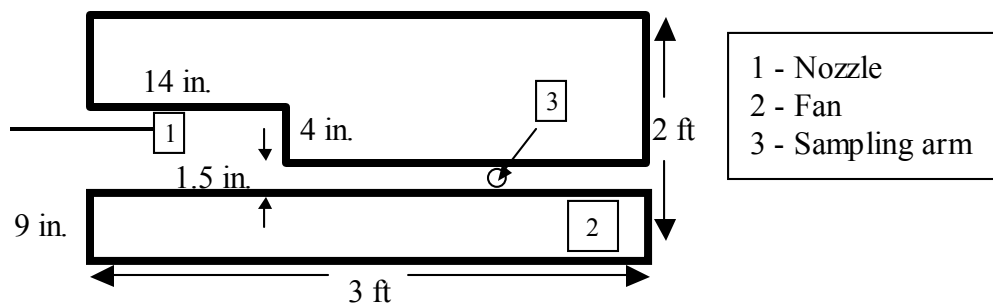


Figure 4.4. Top cover of the laboratory contactor

4.2.2.1. *CO₂ delivery and dissolution*

Pure CO₂ gas was delivered via a Brooks mass flow controller through ¼ inch stainless steel tubing and sparged into the PVC piping upstream of the nozzle. The flow rate of CO₂ was set to obtain a feed concentration of about 2 mM. Pump 2 (March centrifugal pump, model MDX-3) and an inline mixer (Koflo static in-line mixer, model ½-4OC-4-12-2)) were used to ensure that the CO₂ was well mixed and dissolved. The second pump also increased the maximum pressure at which the spray nozzle could be operated.

The centrifugal pump was connected to the rest of the piping system by ½-inch PVC reinforced Tygon[®] hose. Since the Tygon[®] hose and the inline mixer were clear, the dissolution of the CO₂ could be observed visually. In addition, the feed sample line was translucent. If the CO₂ was not dissolving completely, then bubbles could be observed in the feed sample line.

4.2.2.2. *Gas phase CO₂ concentrations*

A 106 cfm fan (Pamotor model 4600XP) was used to prevent the accumulation of desorbed CO₂ in the gas phase and to ensure that the concentration in the gas did not approach equilibrium with the liquid. To verify that the gas phase concentration of CO₂ was low, an experiment was performed with the largest nozzle in the laboratory (¾-A-SS-20). Since this experiment had the greatest liquid rate, the most CO₂ would be stripped out of solution, and the approach to equilibrium was expected to be the closest for this experiment.

Gas samples were taken from the experiment as shown in Figure 4.5. The samples were collected through an inverted funnel (3 inch diameter) pointed away from the nozzle in order to limit the amount of liquid entering the sample line. The funnel reduced the gas velocity at the mouth of the sample line and thus reduced the entrainment of liquid into the sample. A vacuum pump (Barnant model 400-1901, 18 lpm) transferred the gas through ¼ inch polypropylene tubing to a water knockout flask and finally a Horiba PIR 2000 infrared CO₂ gas analyzer.

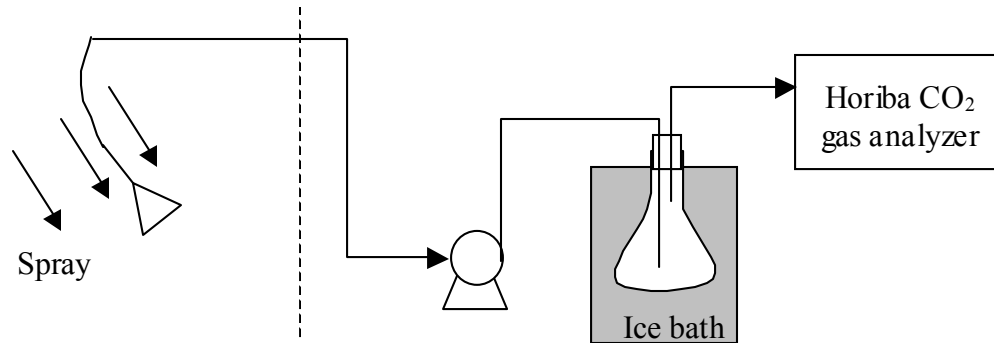


Figure 4.5. Apparatus for measuring gas phase CO₂ concentrations

The measured gas phase concentrations of CO₂ are graphed as a function of position in the spray contactor in Figure 4.6. The spray region is shown by the dashed band extending diagonally downward from the origin. The average ambient concentration of CO₂ during the experiment was 340 ppm. The gas phase concentrations in the spray contactor were higher and ranged from 450 to 490 ppm. The higher gas concentrations were found near the nozzle even though the gas and liquid flows might have been expected to resemble cocurrent flow more than countercurrent flow. The higher concentrations near the nozzle may be due to high mass transfer rates there, but the gas phase appears to be fairly well mixed.

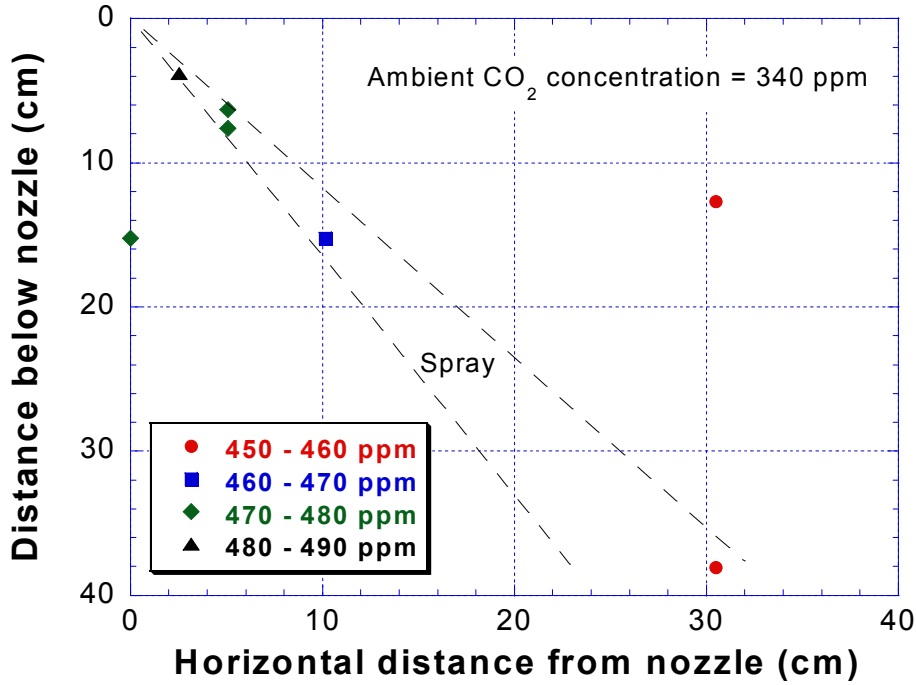


Figure 4.6. Gas phase CO₂ concentrations (Nozzle: $\frac{3}{8}$ -A-SS-20, $\Delta P = 10$ psi)

Although the gas phase CO₂ concentrations were higher than ambient levels, they were still relatively low compared to equilibrium with the liquid in the spray. The liquid entered the column with a CO₂ concentration of about 2 mM. If the N_L of the spray were 2.0, then the spray at the bottom of the column would have a CO₂ concentration of 0.27 mM. At 20°C, the gas concentration of 460 ppm would be in equilibrium with a liquid concentration of 0.018 mM. Thus, the error from neglecting the gas concentration in the calculation of the mass transfer driving force may be estimated as shown in section 4.1.2.

$$\frac{C - (C - C^*)}{C - C^*} = \frac{C^*}{C - C^*} \approx \frac{0.018}{0.27 - 0.018} = 7.1\% \quad (4.4)$$

If the N_L of the spray were less than 2.0, then the estimated error would be lower as well. For example, an N_L of 1.0 would result in an estimated error of only 2.5%.

4.2.3. Pilot scale contactor

As mentioned in the previous chapter, mass transfer in small droplets may not be representative of commercial systems if the small droplets are circulating and the larger droplets undergo shape oscillations. To address scale up issues, experiments were also conducted with a commercial spray nozzle. A large portion of the initial work involved designing and building a pilot scale spray contactor that is more representative of commercial spray scrubbers. The large scale of this experimental apparatus presented several challenges. However, in the absence of rotation in the spray, the droplets and the solute concentration were not expected to have any angular dependence. In other words, the droplet size and solute concentration were expected to vary only in the radial and axial directions. As a result, liquid sampled only in a small angle of the spray pattern should be representative of the entire spray.

A larger scale spray contactor, shown in Figure 4.7 (see Appendix D for more detailed diagrams), was constructed at the Separations Research Program pilot facility on the Pickle Research Campus of The University of Texas at Austin. The pilot scale system is analogous to the laboratory contactor, except that it was designed to contact only a small fraction of the total spray. This design reduced the amount of CO₂ necessary to maintain the steady state feed concentration.

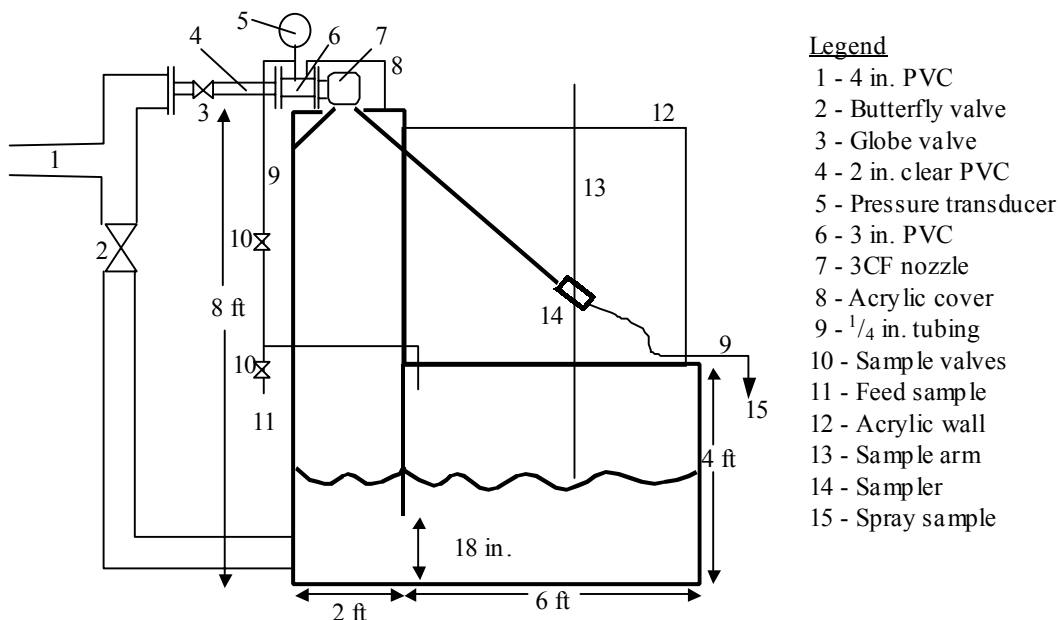


Figure 4.7. Pilot scale spray contactor

The tank was constructed of $\frac{3}{4}$ " polypropylene and consisted of two sections. As indicated in the figure, the tank was filled with city water to a depth of approximately 24 inches to ensure a liquid seal at the bottom of the two sections. Anhydrous citric acid and sodium carbonate powder were added to achieve a citrate concentration of 5 mM and adjust the pH to 4.5. The city water was found to have significant carbonate concentrations, but lowering the pH converted these species to dissolved CO_2 .

The water was circulated through the system with a 250 gpm centrifugal pump (Ingersoll-Rand model 3x2x6 HOC). Pure CO_2 was supplied via a rotameter through $\frac{3}{8}$ inch black polyethylene tubing. The black polyethylene was used because it was inexpensive and more stable for outdoor use in sunlight than the standard clear or white tubing. The rotameter was calibrated up to 0.38 mol/min CO_2 at laboratory conditions. During the pilot scale experiments, the CO_2 flow rate was held constant at a level to achieve about 2 mM CO_2 in the feed to the spray contactor. Since the

actual feed concentration was measured independently, the flow rate of CO₂ did not have to be known exactly.

The CO₂ was sparged into the feed piping approximately 50 feet upstream of the nozzle to ensure that the gas bubbles would have time to dissolve. A short section of clear PVC pipe immediately before the nozzle also allowed visual inspection of the flow.

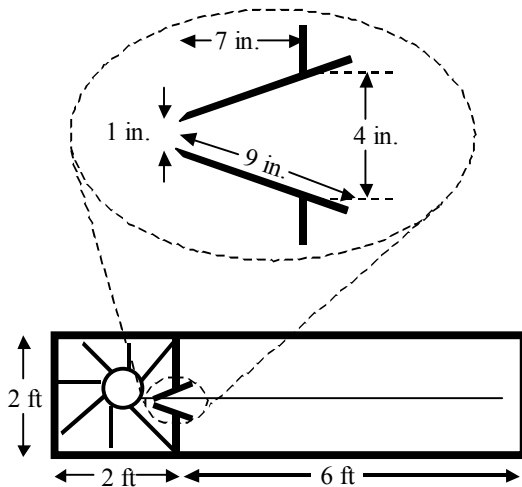


Figure 4.8. Top view of pilot scale contactor

The nozzle sprayed the CO₂ solution into the first section, where most of the liquid was collected and recycled. A small ray of the spray passed between a pair of baffles into the second section of the contactor. The baffles were designed with sharp edges and angled so that the rest of the spray would be deflected and not interfere with the ray of interest. After the spray passed between the baffles, it entered the second section of the column, where samples were collected and analyzed. The second section of the contactor had clear acrylic walls to allow observation of the spray behavior and sample collection.

The top of the second section and the end opposite the nozzle were open to the atmosphere to allow ambient air to circulate and remove desorbed CO₂ from the contacting zone. Since only a small fraction of the spray was sampled, the circulation

of ambient air should be sufficient to remove desorbed CO₂ from the spray tower. The spray fell into the outer section of the tank, and then the liquid was recycled.

4.3. SAMPLE STORAGE

In order to stabilize the samples and minimize additional losses of CO₂ after sample collection, the samples were stored in a NaH₂PO₄/Na₂HPO₄ buffer solution to raise the pH to about 7.5. Increasing the pH prevented desorption during sample storage, handling, and analysis by converting much of the dissolved CO₂ into HCO₃⁻. Since the pK_a of CO₂ is 6.3, raising the pH to 7.5 reduced the driving force for CO₂ desorption by more than a factor of ten.

The phosphate buffer solution was prepared by dissolving NaH₂PO₄ in deionized water and adding 5 M NaOH solution to adjust the pH to 7.5. Bicarbonate and carbonate species were commonly found as impurities in the phosphate salts, and the NaOH stock solution tended to absorb CO₂ from air. Therefore, after the NaOH was added to the phosphate solution, the concentration of carbonate species was about 1.0 mM, whereas 0.2 mM at pH 7.5 would be in equilibrium with air. To reduce the background level of CO₂, the buffer solution was stirred and sparged with air for three hours. Finally, the solution was diluted to a final phosphate concentration of 0.5 M. The final buffer solution typically had total carbonate species concentration of about 0.2 mM.

The liquid spray samples generally contained about 2 mM CO₂ and 5 mM citrate buffer solution (pH 4.5). Glass 16 mL sample vials were prepared with 1.0 mL of phosphate buffer solution. Liquid samples were transferred directly from the sample collectors into the sample vials and the phosphate solution. Whenever possible, the outlet of the sample port was placed below the liquid surface in the vial. Then, the vials were capped with minimal gas headspace and shaken to ensure good mixing of the sample with the phosphate buffer. As suggested by ASTM standard D513-92, the sample vials were stored in an ice chest or refrigerator until they were analyzed. Additional data on sample storage and stability is included in Appendix E.

4.4. SAMPLE ANALYSIS

Several analytical methods were considered for measuring the change in CO₂ liquid concentrations. Altwicker and Lindhjem (1988) measured the pH change when dissolved CO₂ reacted with NaOH solution. Taniguchi et al. (1997) used a back titration method with Ba(OH)₂ and HCl. However, the precision with which concentration may be calculated from pH measurements is limited. For example, if the pH is known within 0.01 pH units, then the hydrogen ion concentration is only known within about 2%. Two methods for measuring liquid phase CO₂ concentrations were used in this work: a gas-sensing electrode and a total carbonate analyzer.

4.4.1. CO₂ electrode

ASTM standard D513-92 describes procedures for using a gas-sensing electrode to measure CO₂ in water samples. In the Orion 95-02 CO₂ electrode, CO₂ diffuses across a gas permeable membrane, and a pH electrode measures the pH change of the internal filling solution. Since these electrodes also use pH measurements to determine concentration, they may have precision limitations similar to those discussed for titration. In addition, the electrode reading can drift, or the membrane can be damaged. Other volatile weak acids, such as acetic acid, also diffuse across the membrane and affect the measurement.

A more important issue for the experiments in this work was related to the internal filling solution. If the total concentration of the sample solution is significantly less than that of the electrode internal filling solution, then water also diffuses across the membrane. The water dilutes the internal filling solution and results in electrode drift.

Nevertheless, the CO₂ electrode is portable and continuous measurements may be taken relatively easily. Thus, the CO₂ electrode was used to obtain rough, on-line values for the feed concentration in some experiments. By monitoring the feed concentration, steady state operation could be verified and maintained.

4.4.2. Total carbonate analyzer

Liquid phase CO₂ concentrations were determined with a total carbonate analyzer. During analysis, an aliquot of sample was acidified to convert all carbonate species (CO₂, HCO₃⁻, and CO₃⁼) to CO₂ and liberate CO₂ gas. The CO₂ was stripped out of solution by an inert gas (N₂) that contains negligible CO₂. The gas exiting the analyzer was then dried, and the CO₂ concentration of the gas stream was measured with a Horiba PIR 2000 CO₂ gas analyzer by infrared spectroscopy. The response of the analyzer was recorded on a Soltec 1242 chart recorder. See Appendix F for a more detailed description of the procedure.

Standard solutions of 1.0 mM NaCO₃ were prepared and analyzed with the total carbonate analyzer. By varying the volume of standard solution being analyzed (10 to 100 μL), the analyzer response was calibrated to give the moles of carbonates as a function of the peak height on the chart recorder. The standard error of the calibration curve was typically about 1 to 2%, and replicate analyses indicated that the procedure was reproducible within about 1%. Then, an aliquot of sample was analyzed to determine the total carbonate concentration in the solution. Since the pH of the water in the spray experiment was 4.5, all the carbonate in solution may be assumed to be in the form of CO₂.

4.5. SPRAY SAMPLER DEVELOPMENT

Liquid samples were taken from the feed line to determine the concentration of CO₂ at the inlet to the test system. Liquid samples were collected from the spray and analyzed to obtain concentrations of CO₂. A sampling device and methods had to be developed to minimize the desorption of CO₂ from the samples during the collection event. Measurements of the mass transfer in a spray are sensitive to wall effects and the method of sample collection. Gas entrainment, secondary drop breakup, and turbulent surface renewal can result when the high velocity spray impacts the tower walls, liquid surfaces, or the sample collection device itself.

Most of the literature for spray towers have neglected sample collection effects and assumed that all of the mass transfer is due to the spray droplets. Little or no data exists for mass transfer during spray impact or sample collection, and methods for sample collection have been crude. In single droplet studies, more care has been taken, and methods include isolating collected droplets from the gas stream with an oil film (Amokrane et al., 1994; Kaji et al., 1985; Taniguchi et al., 1997) and collecting the droplets in NaOH solution so that dissolved CO₂ reacts before it can desorb into the gas (Altwicker and Lindhjem, 1988).

Several different sampler designs are discussed in the following sections. The performance of each sampler was tested in laboratory experiments with liquid jets and, in some cases, laboratory scale spray nozzles. The goals of the sampler development were to measure and characterize the mass transfer in each sample collector and then to minimize that mass transfer so that the mass transfer of sprays could be measured accurately.

4.5.1. Simple sampler results

Initial designs collected samples continuously to minimize the contact time for extra mass transfer to occur. The sampler consisted of an open tube with a 3/4" inside diameter. Maintaining the liquid level in the sampler was problematic. If the liquid level in the sampler was high, then turbulent mixing, splashing, and frothy behavior was observed. In addition, increasing the liquid level also increased the residence time of liquid in the active mass transfer zone. However, if the liquid level was too low, then gas was entrained into the outlet of the sampler and into the sample line. The entrained gas and the two-phase flow in the tubing were expected to lead to too much additional desorption of CO₂. At higher sample flow rates and/or higher spray velocities, gas entrainment became even more of an issue.

Mass transfer results with the open sampler and a 1/64" (0.04 cm) jet are given in Table 4.2. The "high" liquid level refers to a level near the top of the sampler, approximately 3" of liquid. The "low" liquid level indicates that only about

1” of liquid was maintained in the sampler. Gas entrainment into the sample line was common at the low liquid level.

Table 4.2. N_L values for open sampler and 0.04 cm jet

Liquid level	$\Delta P = 5$ psi	$\Delta P = 10$ psi
High	0.220	0.519
Low	0.557	0.809

Both the velocity of the liquid entering the sampler and the liquid level in the sampler had strong effects on the mass transfer in the sampler. As the data at the low liquid levels shows, the losses of CO₂ due to gas entrainment into the sample line increased the sampler N_L dramatically. At the higher liquid level, less mass transfer was observed, but N_L was still significant and a strong function of the liquid velocity. Improving the reproducibility of the sampler by reducing the dependence of the sampler N_L on spray velocity was an important goal so that the effect of pressure on spray mass transfer could be measured.

4.5.2. Overflow sampler

The overflow sampler consisted of an acrylic tube ($\frac{3}{4}$ ” i.d. x 4” length) packed with NaturalAire air filter media. Samples were collected and withdrawn continuously through $\frac{1}{4}$ inch Tygon tubing with a peristaltic pump (Masterflex model 7521-40) to minimize the residence time of liquid in the sampler. The purpose of the packing was to reduce splashing and turbulent mixing and to facilitate gas-liquid separation. The spray flux was measured by adjusting the sample flow rate to maintain a constant liquid level in the sampler. However, during operation the packing was flooded so that it did not contribute additional interfacial area for mass transfer. A fraction of the spray that was intercepted by the sampler was pumped out of the bottom, and the rest was allowed to overflow. The ratio of overflow to sample flow rate was varied to minimize the sampler mass transfer.

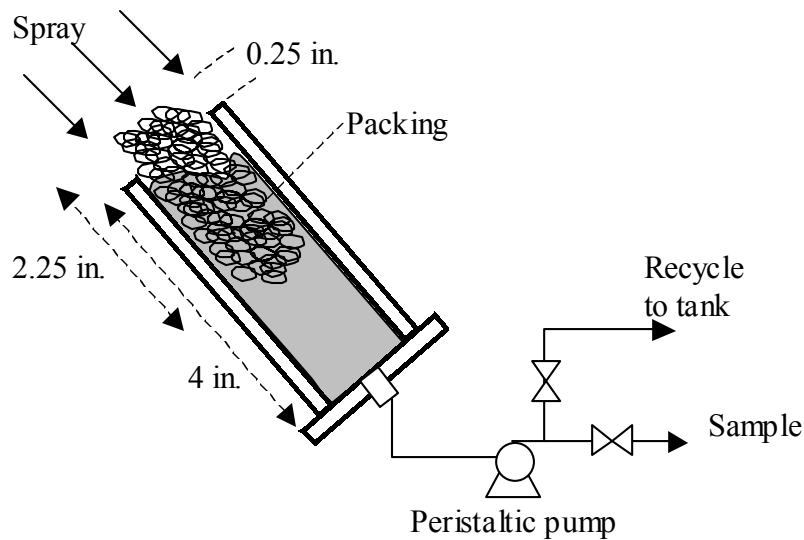


Figure 4.9. Overflow sample collector

4.5.2.1. Overflow sampler development

CO₂ desorption experiments were conducted to characterize the mass transfer occurring during sample collection. The mass transfer was measured in the laboratory contactor as a function of distance at several operating pressures and for several nozzles. Cylindrical liquid jets were used in most of the characterization experiments because the mass transfer as a function of distance was more easily determined, particularly close to the nozzle. By extrapolating to zero distance, the mass transfer in the jet was eliminated, and the mass transfer in the sampler was determined under each set of conditions. Experiments were also conducted with the smaller spray nozzles to verify that the results for jets and sprays were consistent.

Initial experiments with the 1/8-A-SS-0.5 spray nozzle were used in the development of the overflow sampling methods. Measurements were taken at two distances from the nozzle (0.32 and 0.64 cm) and with two different packing configurations (Figure 4.10). In the low packing arrangement, the top of the packing was 0.64 cm below the top of the sampler. In the high packing arrangement, the packing extended 0.64 cm above the top of the sampler. The spray flux was

measured by adjusting the sample flow rate to maintain a constant liquid level in the sampler. Then, the sample flow rate was reduced so that some of the liquid overflowed. Samples were collected at several flow rates to determine the optimal conditions to minimize the sampler mass transfer.

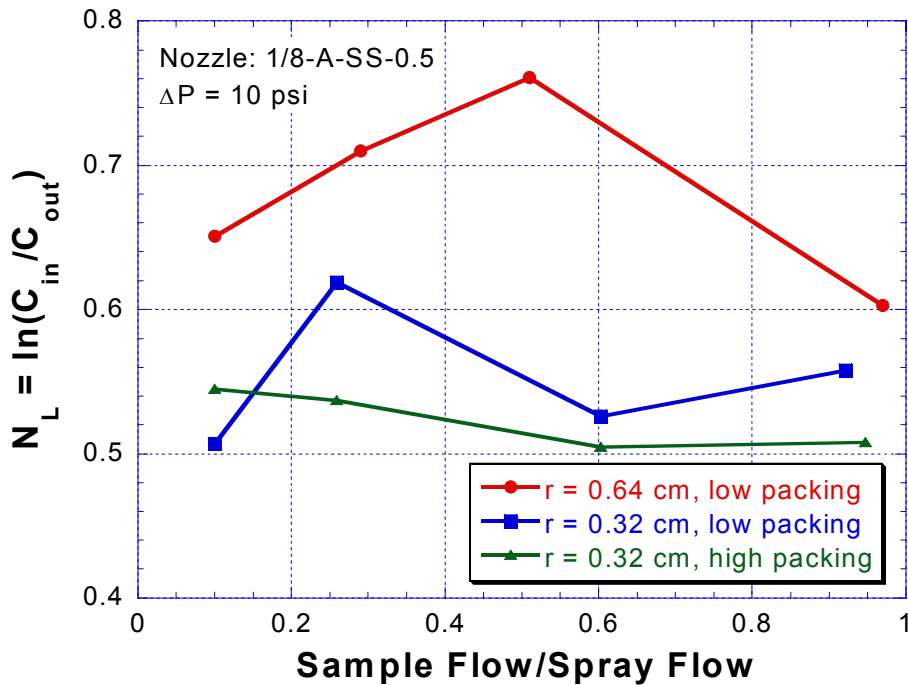


Figure 4.10. Effect of overflow ratio on sampler mass transfer

Increasing the packing to a level at or slightly above the liquid surface had a small effect on the mass transfer. The N_L for the high packing case was consistently lower than for the low packing. No consistent trend was observed for the effect of the overflow ratio on the sampler mass transfer. In later experiments, the high packing level was used, and sample flow was set at 80-100% of the spray flow in order to reduce the time required to collect samples.

4.5.2.2. *Overflow sampler mass transfer*

Significant mass transfer was measured during spray impact in the overflow sample collection device (Table 4.3). The number of liquid phase transfer units for the sampler was correlated as a function of the liquid velocity and liquid fraction

(Equation 4.4). The liquid velocity was calculated from the nozzle pressure drop (Equation 3.22), and the liquid fraction (f) was calculated by normalizing the measured sample flow rate (Q_p) by the cross-sectional area of the sampler and the liquid velocity. The liquid fraction is a convenient parameter because it is dimensionless and should be constant for a given liquid jet experiment.

Table 4.3. Overflow sampler characterization

Cylindrical jet diameter	ΔP (psi)	Q_p (cm ³ /min)	Flux (cm/s)	U (m/s)	f = Flux/U	N_L	
						Measured	Calculated
0.04 cm	5	59	0.34	8.3	4.13×10^{-4}	0.32	0.35
	10	87	0.51	11.7	4.34×10^{-4}	0.49	0.46
	20	118	0.69	16.6	4.17×10^{-4}	0.66	0.61
0.09 cm	5	302	1.77	8.3	2.13×10^{-3}	0.18	0.28
	10	431	2.52	11.7	2.14×10^{-3}	0.32	0.37
0.12 cm	5	490	2.87	8.3	3.45×10^{-3}	0.36	0.26
	10	676	3.95	11.7	3.37×10^{-3}	0.42	0.34
	20	970	5.67	16.6	3.42×10^{-3}	0.57	0.45
0.16 cm	5	926	5.42	8.3	6.52×10^{-3}	0.28	0.24
	10	1310	7.66	11.7	6.52×10^{-3}	0.28	0.31
	20	1852	10.83	16.6	6.52×10^{-3}	0.30	0.41
Spray nozzle							
1/8-A-SS-0.5	10	150	0.88	11.7	7.49×10^{-4}	0.40	0.43
	20	215	1.26	16.6	7.56×10^{-4}	0.58	0.56
1/8-A-SS-2	10	224	1.31	11.7	1.12×10^{-3}	0.30	0.40

The N_L of the overflow sampler ranged from 0.2 to nearly 0.7 at the high spray velocities and low sample flow rates. The N_L was correlated with the velocity in cm/s and with the liquid fraction.

$$N_L = 5.01 \times 10^{-4} U^{0.81} f^{-0.14} \quad (4.5)$$

The sampler N_L was found to have a strong dependence on the spray velocity and a weak negative dependence on the liquid fraction. The higher velocities imparted greater turbulence to the liquid and entrained more gas into the sampler,

both of which tended to increase the sampler mass transfer. At higher liquid fractions, the higher sample flow rates reduced the residence time of the liquid in the sampler, thereby reducing the sampler mass transfer. A parity plot of the overflow sampler N_L correlation is shown in Figure 4.11. The correlation also predicts the sampler N_L for the two small spray nozzles, indicating that the sampler N_L data with jets and sprays should be equivalent.

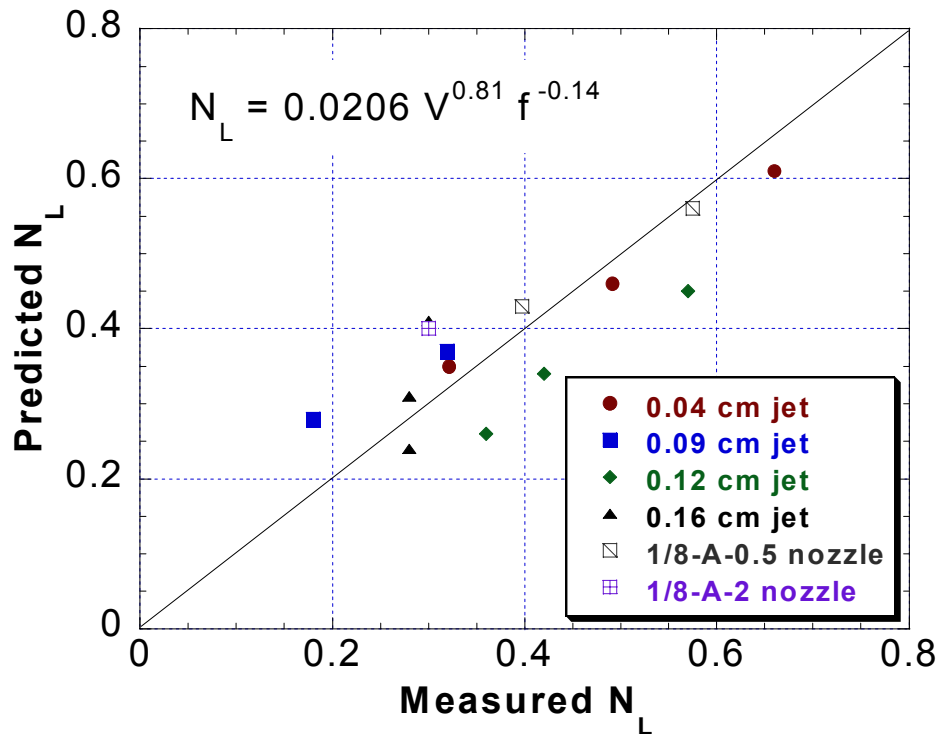


Figure 4.11. Parity plot of the overflow sampler correlation

Based on the work of other researchers, N_L values of 1 to 2 were expected for the spray, but a great deal of mass transfer was found to occur in spray impact or sample collection. Thus, mass transfer during sample collection with the overflow sampler was a large fraction of the expected values for the spray N_L . As little as half of the total observed mass transfer may be due to the spray, and the rest of the mass transfer may be occurring at the walls, at spray impact on column internals, or at the liquid surface in the bottom of the spray tower. Spray column designs can take

advantage of the exceptionally high N_L per unit contactor volume during impact by limiting the amount of contactor volume occupied by the droplets. Impact surfaces could be positioned immediately below the spray nozzles so that the high velocity sprays impact the surfaces. The liquid could be collected and recycled to the reaction tank or fed to the next spray header.

4.5.3. Quench sampler

The quench sampler was designed to further reduce the mass transfer during sample collection. Like the overflow sampler, the quench sampler consisted of an acrylic tube packed with air filter media. Liquid was pumped out of the sampler, and the peristaltic pump was used to measure the spray flux. However, during sample collection, a 0.1 M sodium hydroxide (NaOH) solution was also continuously fed to the top of the sampler through a 0.040-inch orifice. The orifice was drilled at a 45° angle so that the hydroxide solution was directed down into the sampler. The angle reduced losses of hydroxide solution out the top of the sampler and facilitated mixing of the hydroxide and the liquid in the sampler.

The NaOH solution and the sample stream were controlled by the same peristaltic pump drive so that the ratio of NaOH solution to sample flow rate was held constant. The NaOH solution was delivered through ¼ inch i.d. tubing, and the sample stream was withdrawn using ⅛ inch i.d. tubing. The ratio of the flow rates for the two peristaltic pumps was 1.0:3.5. The NaOH solution mixed with the collected spray and reacted to convert dissolved CO₂ into bicarbonate ion, which does not desorb out of solution.

Over time, the NaOH solution tended to absorb CO₂ from air, so care was taken to minimize and account for the background concentration of carbonate species in the solution. The quenching solution was prepared from NaOH pellets and deionized water in a collapsible plastic bag. The collapsible reservoir allowed solution to be withdrawn without exposing the solution to air or developing a vacuum. The background concentration in the quenching solution had to be

measured and subtracted from the total carbonate concentration of spray samples. Typically, the total carbonate concentration of the NaOH solution was 0.3 to 0.4 mM.

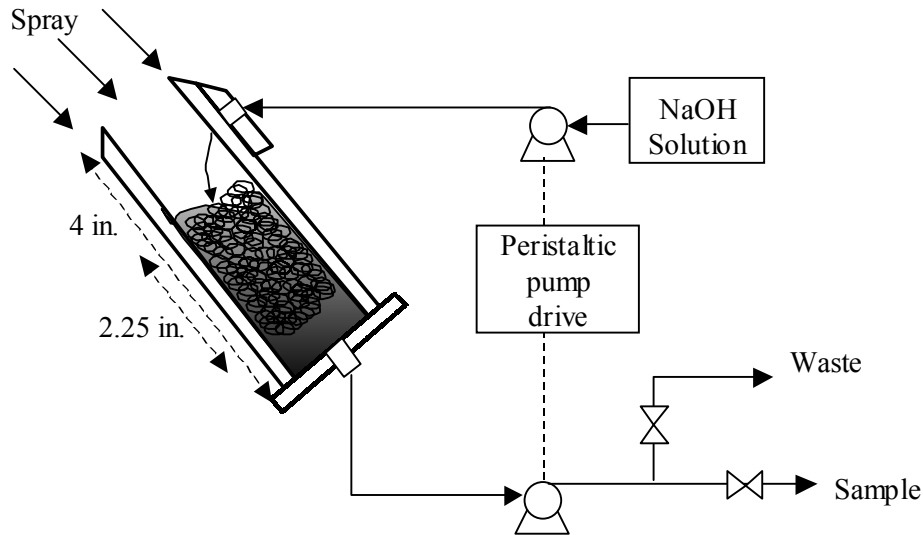


Figure 4.12. Quench sample collector

4.5.3.1. Quench sampler development

As with the overflow sampler, CO₂ desorption experiments were conducted with the 0.04 cm jet to characterize the mass transfer and to continue developing the quench sampler design. Factorial experiments were performed with high/low liquid levels and with/without quenching, and results are shown in Table 4.4. The high liquid level means that the surface of the liquid in the sampler was at the top of the packing, and the low level means that the liquid level was about 2" below the top of the packing. Again, gas entrainment was observed at the low liquid level. Although these experiments were operated with no overflow, the results for the runs without quenching were similar to the correlated values for the overflow sampler N_L , as expected.

Table 4.4. N_L data for quench sampler development (0.04 cm jet, high and low liquid levels)

ΔP (psi)	Overflow correlation	Not quenched		Quenched	
		High level	Low level	High level	Low level
5	0.32	-0.04	0.38	0.06	0.01
10	0.49	0.47	0.31	-0.02	0.16
20	0.66	0.67	0.71	0.23	0.44

When the basic solution was used to quench the mass transfer in the sampler, the N_L decreased markedly. On average, the sampler N_L at high liquid levels with quenching were lower than those at low liquid levels. The higher level ensured that the spray and the quenching solution mixed as soon as possible. When the spray entered the sampler, it immediately encountered the quenching solution, and the turbulence of the impact and collection facilitated the mixing of the spray with the NaOH. The quench sampler N_L also exhibited less dependence on the liquid level and was more reproducible than the N_L for the non-quenched sampler. Since the liquid level was somewhat difficult to control, reducing the dependence of the sampler N_L on liquid level was advantageous. Thus, the quench sampler successfully eliminated much of the sampler N_L and was operated with the liquid level at the top of the packing in subsequent experiments.

4.5.3.2. Quench sampler mass transfer

Results for the quench sampler are given in Table 4.5 and in Figure 4.13, where some of the data with the overflow sampler is included for comparison. The average values and standard deviations for the quench sampler N_L at each pressure are shown as well. Little or no effect of the jet diameter was observed. At nozzle pressures up to 10 psi (velocities up to 11.7 m/s), the N_L in the quench sampler was effectively zero, compared to about 0.4 for the overflow sampler under similar conditions. At 20 psi, data with for larger jet still showed no mass transfer in the

sampler. For the smaller jet at high pressure, the mass transfer may be significant, but it is still much less than the 0.66 transfer units for the overflow sampler.

Table 4.5. Quench sampler characterization

Jet	ΔP (psi)	Q_p (cm ³ /min)	Flux (cm/s)	U (m/s)	$f = \text{Flux}/V$	N_L
0.04 cm	5	68	0.40	8.3	4.81×10^{-4}	0.06
	10	90	0.53	11.7	4.48×10^{-4}	-0.02
	20	132	0.77	16.6	4.65×10^{-4}	0.23
0.12 cm	5	473	2.77	8.3	3.33×10^{-3}	-0.02
	10	680	3.97	11.7	3.38×10^{-3}	0.08
	20	968	5.66	16.6	3.41×10^{-3}	-0.04
Jet at 45° angle						
0.04 cm	5	60	0.35	8.3	4.23×10^{-4}	-0.24
	10	87	0.51	11.7	4.33×10^{-4}	0.01
	20	126	0.74	16.6	4.44×10^{-4}	0.18
0.04 cm	5	64	0.38	8.3	4.53×10^{-4}	0.06
	5	64	0.38	8.3	4.53×10^{-4}	0.06
	10	91	0.53	11.7	4.54×10^{-4}	0.05
	10	91	0.53	11.7	4.54×10^{-4}	0.00
	20	129	0.76	16.6	4.56×10^{-4}	0.06
	20	129	0.76	16.6	4.56×10^{-4}	0.07
0.12 cm	5	480	2.81	8.3	3.38×10^{-3}	0.07
	5	480	2.81	8.3	3.38×10^{-3}	-0.06

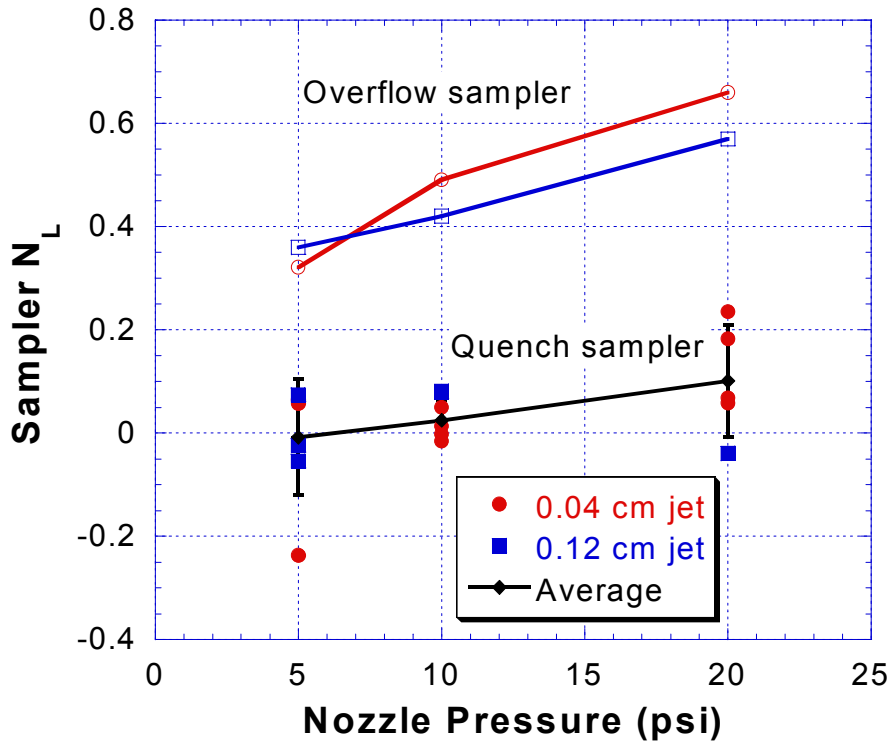


Figure 4.13. Quench sampler results

In most of the sampler characterization experiments, the jet and the sampler were oriented vertically, but the sampler was pointed at the nozzle during spray experiments as shown in Figure 4.9. Therefore, experiments were also conducted with the jet and the sampler at a 45° angle to check for an effect of sampler orientation. The results agree with the earlier experiments, and provide an estimate of the uncertainty in the sampler N_L measurements. Since the effect of jet diameter was not statistically significant, average values and standard deviations were calculated for N_L at each operating pressure. A negative N_L was measured for one run at 5 psi but it can be neglected as a statistical outlier since the standardized residual is large (Montgomery, 1997).

The N_L of the quench sampler is negligible except perhaps at the highest velocity and lowest flow rate, where it reaches a maximum of 0.1 ± 0.1 . These conditions are the same as those for the highest overflow sampler N_L . Alternatively,

a more conservative conclusion would be that the quench sampler N_L is 0.0 ± 0.2 over the entire range of velocities and flow rates. The quench sampler N_L was assumed to be zero in the subsequent spray experiments. In any case, the quench sampler significantly reduces the mass transfer during sample collection compared to the overflow sampler. Thus, the quench system was used to measure mass transfer in all the subsequent spray experiments, and the sampler N_L was neglected.

Chapter 5: Spray mass transfer

Using the experimental methods and quench sampling described in the previous chapter, the mass transfer performance of sprays was measured directly. As discussed earlier, the spray consists of distinct regions. Immediately after exiting the nozzle, the liquid exists as a continuous sheet expected to have high k_L and area but extremely short contact time. During the breakup process, the sheet disintegrates into ligaments and then droplets. The ligaments and droplets might be expected to have similar k_L and area, but the lifetime of the ligaments is insignificant compared to that of the droplets. Therefore, the ligaments were neglected, and only the sheet and the droplets are considered in the interpretation of the spray mass transfer performance.

5.1. SHEET OBSERVATIONS

The transition between the sheet and the droplet regions had to be measured before the mass transfer in different parts of the spray could be separated. In the laboratory experiments, this transition was easily determined. The sheet behavior was observed with a strobe light, and the breakup length was measured directly. At the nozzle exit, the sheet appears smooth. Even though turbulence may be present in the liquid, the surface of the sheet is expected to be smooth immediately after exiting the nozzle because the liquid was just in contact with the wall of the orifice. Similar observations were made by Davies (1972) in a study of turbulent jets. Farther from the nozzle, waves can be seen on the surface of the sheet, and the sheet eventually breaks into ligaments and droplets.

A photograph of the sheet emanating from the $\frac{3}{8}$ -A-SS-20 nozzle operated at 10 psi pressure drop is given in Figure 5.1. The sheet was illuminated from above by a small laboratory strobe light. Because of the relatively low light, the shutter speed of the camera was relatively slow, and the sheet breakup point is not as clear in the photograph as it was for visual observations. However, the smooth surface of the sheet and the appearance of waves can be easily seen in Figure 5.1.

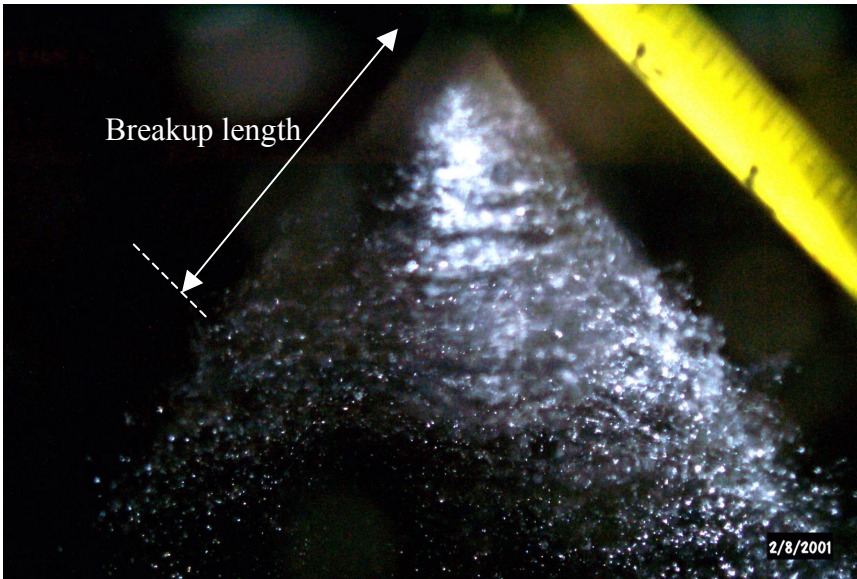


Figure 5.1. Sheet breakup (Nozzle: $\frac{3}{8}$ -A-SS-20, $\Delta P = 10$ psi)

The behavior of the sheet for the large nozzle was also observed, but the sheet breakup was difficult to measure. In flash photographs (Figure 5.2), the surface and the length of the sheet appeared irregular. Since the scale of turbulence is limited by the size (i.e. pipe diameter), the irregularities may be due to larger scales of turbulent eddies, which would not have been present in the laboratory experiments. The condition of the nozzle also may have affected the sheet. Even right next to the nozzle, the surface of the sheet was not smooth. The small nozzles were new and made of stainless steel, but the large nozzle was used and somewhat worn. It was made of silicon carbide and was obtained from R. Håkansson of ABB (Håkansson, 1998). The roughness of the nozzle surfaces could have contributed to the irregularities in the sheet.

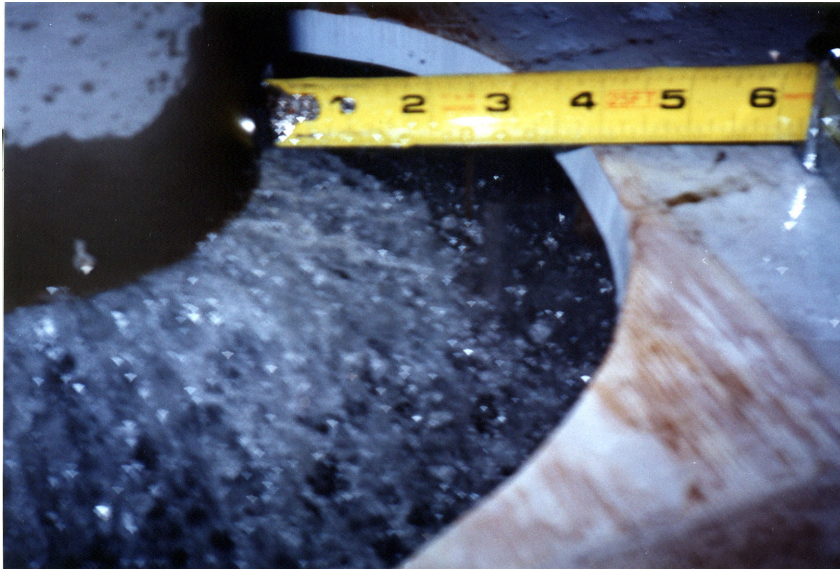


Figure 5.2. Sheet breakup (Nozzle: 3CF-SILCNB-120, $\Delta P = 5$ psi)

The 3CF nozzle did not have a distinct sheet length that was easily measured. From Figure 5.2, the sheet breakup length could be anywhere from 2.0 to 3.5 inches. The sheet for the large nozzle appears significantly different from the sheet for the $\frac{3}{8}$ inch nozzle. On the sheet from the small nozzle, waves could be seen developing perpendicular to the direction of flow. With the large nozzle, there seem to be ligaments oriented in the direction of flow. These ligaments could be the result of surface irregularities as previously discussed, or they could indicate a different type of breakup phenomena.

5.1.1. Breakup length

The sheet breakup length (L_b) was measured for each laboratory nozzle at each operating pressure. A strobe light was used to illuminate the sheet under low ambient light so that the sheet breakup could be more easily determined. The initial thickness of the sheet (h_0) and the initial velocity (U_0) were calculated according to Equations 3.21 and 3.22 and used to calculate the Reynolds and Weber numbers for the sheet. Then, sheet breakup lengths for the small nozzles were correlated with the sheet Reynolds and Weber numbers, defined below.

$$\text{Re}_o = \frac{h_o U_o \rho_L}{\mu_L} \quad (5.1)$$

$$\text{We}_o = \frac{h_o U_o^2 \rho_L}{\sigma} \quad (5.2)$$

The result of the empirical correlation for sheet breakup is given in Equation 5.3 below, and a parity plot of the correlation is given in Figure 5.3.

$$\frac{L_b}{d_{or}} = 4740 \text{Re}_o^{-0.8} \text{We}_o^{0.07} \quad (5.3)$$

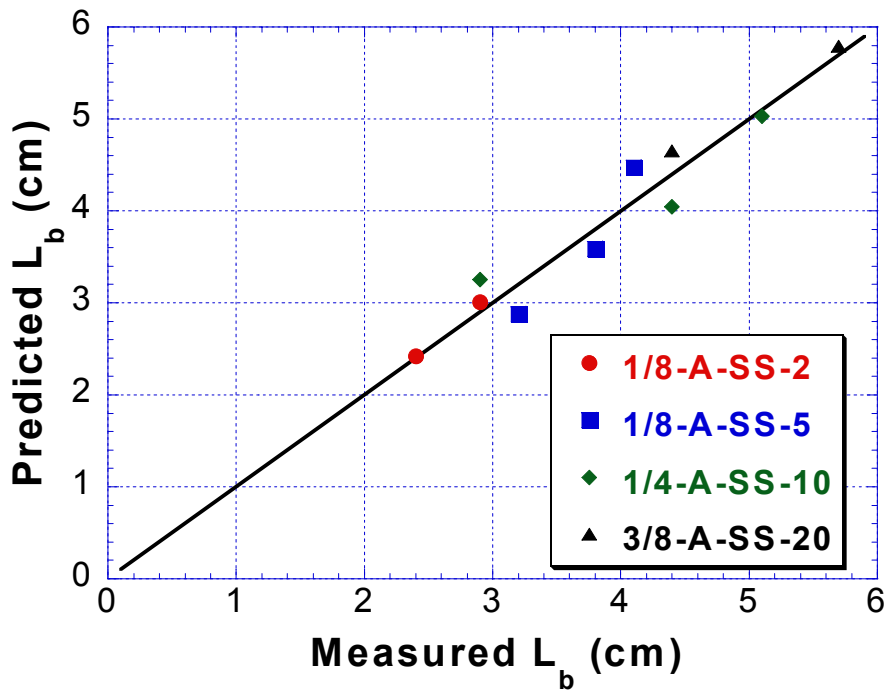


Figure 5.3. Parity plot of sheet breakup correlation (Equation 5.3)

In Table 5.1, the measured breakup lengths are compared with the predictions of Equation 5.3 and the breakup models of Dombrowski and Hooper (1962) and Senecal et al. (1999). Both of the theoretical models overpredict the sheet breakup lengths for all of the nozzles at the operating conditions used in laboratory work. As previously discussed, sheet breakup measurements for the 3" nozzle were not possible. The nozzle vendor also did not have data available for the sheet lengths of

the nozzles. Therefore, the prediction of the empirical correlation was used to estimate the sheet length of the 3” nozzle.

Table 5.1. Sheet breakup measurements and model predictions

Nozzle	ΔP (psi)	h_o (μm) ¹	Re_o	We_o	Sheet breakup length (cm)			
					Measured	Correlated ²	D&H ³	Senecal ⁴
1/8-A-SS-2	10	194	2278	371	2.9	3.0	7.0	4.3
	20	194	3216	742	2.4	2.4	4.7	3.3
1/8-A-SS-5	5	311	2580	297	4.1	4.5	13.2	7.3
	10	310	3642	594	3.8	3.6	8.4	5.6
	20	310	5140	1186	3.2	2.9	6.0	4.3
1/4-A-SS-10	5	427	3548	409	5.1	5.0	14.2	8.9
	10	427	5008	817	4.4	4.0	9.9	6.9
	20	426	7069	1630	2.9	3.2	7.4	5.3
3/8-A-SS-20	5	621	5154	594	5.7	5.8	16.6	11.1
	10	620	7275	1186	4.4	4.6	12.2	8.7
3CF-SILCNB-120	5	5101	42348	4883		10.5	60.6	80.6
	10	5089	59750	9744		8.5	46.8	40.5
	20	5076	84283	19437		7.1	36.3	20.3

¹Calculated from Equation 3.21

²Predicted values from correlation (Equation 5.3)

³Model predictions of Equation 3.15 (Dombrowski and Hooper, 1962)

⁴Model predictions of Equation 3.16 (Senecal et al., 1999)

5.1.2. Calculated properties at breakup

The wavelengths of the disturbances that result in sheet breakup are large relative to the droplet diameters. Therefore, when the sheet breaks, its thickness ($2h_b$) is smaller than the diameter of droplets that will be produced. As a result, the area per unit volume of the sheet can be much greater than that of the droplets. From Equation 3.23, the sheet length can be used to estimate a sheet thickness at breakup.

$$h_b = h_o \left(\frac{x_o}{x_o + L_b} \right) \quad (5.4)$$

At the breakup point, the area per unit volume of the sheet may be calculated easily. Consider a flat, two-sided sheet with width w , length dx , and thickness $2h$. Then, the area per unit volume at the point of breakup is

$$a_b = \frac{2wdx}{2hwdx} = \frac{1}{h_b} \quad (5.5)$$

The cumulative area per unit volume of the entire sheet (from $x = 0$ to $x = L_b$) may be calculated as described in Chapter 3. The rate of change of sheet thickness is greatest at the nozzle exit, so if $\left. \frac{dh}{dx} \right|_{x=0} \ll 1$ then Equation 3.29 may be used to calculate the area per unit volume of the sheet (a_s). Although the calculated values for a_s are very high, the short contact time of the sheet (t_s) will limit the amount of mass transfer that can take place. The area and other calculated properties of the sheet at breakup are given in Table 5.2.

Table 5.2. Calculated sheet properties at breakup

Nozzle	ΔP (psi)	h_b (μm)	a_b (cm^{-1})	$\left. \frac{dh}{dx} \right _{x=0}$	a_s (cm^{-1})	t_s (ms)	d_{32} (μm)*	a_d (cm^{-1})
1/8-A-SS-2	10	10	979	-0.0639	934	2.6	335	179
	20	12	835	-0.0669	806	1.5	307	195
1/8-A-SS-5	5	18	555	-0.0623	532	5.4	439	137
	10	21	474	-0.0652	459	3.1	403	149
	20	25	405	-0.0682	398	1.7	370	162
1/4-A-SS-10	5	29	339	-0.0632	329	6.1	498	120
	10	34	290	-0.0661	285	3.4	458	131
	20	40	249	-0.0691	248	2.0	420	143
3/8-A-SS-20	5	52	191	-0.0642	188	7.0	578	104
	10	61	164	-0.0672	164	4.0	531	113
3CF- SILCNB-120	5	1403	7.1	-0.0702	8.3	12.6	1334	45
	10	1570	6.4	-0.0732	7.6	7.3	1225	49
	20	1722	5.8	-0.0761	7.1	4.3	1125	53

* See data from Spraying Systems (Appendix A)

The values in Table 5.2 were computed using the correlated breakup lengths from Equation 5.3. For comparison, estimates of the area per unit volume for the droplets are also included in the table. The Sauter mean diameters of the droplets were calculated based on data provided by Spraying Systems (Appendix A). Then, from the definition of d_{32} , the area per unit volume for the droplets is given by

$$a_d = \frac{\pi d_{32}^2}{\frac{1}{6} \pi d_{32}^3} = \frac{6}{d_{32}} \quad (5.6)$$

For the laboratory nozzles, the calculated areas of the sheet are much greater than the areas of the droplets. However, the difference between a_s and a_d decreases as

the nozzle size increases. In fact, for the 3CF nozzle, the sheet area was actually calculated to be lower than the droplet area.

5.2. MASS TRANSFER RESULTS

The results of the laboratory spray experiments with the quench sampler are shown in Table 5.3. Although the temperature in the spray experiments was not controlled, the temperature of the liquid was measured and found to be between 20 and 25°C. At operating pressure drops of 5, 10, and 20 psi, the N_L of the spray is given as a function of distance from the nozzle. The variation of spray flux or sample flow rate (Q_p) limits the range of distance over which measurements can be made during a given experiment. Data is not presented for the 1/8-A-SS-2 nozzle at 5 psi or the 3/8-A-SS-20 at 20 psi. For the small nozzle, the spray is not fully developed at such a low pressure. For the larger nozzle, the laboratory apparatus could not deliver the high liquid flow rate and dissolve the CO₂ at the same time.

In Table 5.4, similar results for the pilot scale experiments with the 3CF nozzle are given. As in the laboratory experiments, the liquid temperature was measured, and at steady state, it was found to be between 35 and 40°C. Data was also collected as a function of angular position in the spray. At each distance, the angles are coded such that “0” corresponds to the central core of the spray, where the spray flux is highest. Sample points on the inside and outside fringes of the spray are denoted as “-” and “+” respectively. Most of the data outside of the core of the spray is slightly lower than the measurements taken at the center of the spray. However, the difference is not statistically significant when compared to the variance in the rest of the data.

Table 5.3. Spray mass transfer in laboratory experiments (T = 20-25°C)

Nozzle	$\Delta P = 5 \text{ psi}$				$\Delta P = 10 \text{ psi}$				$\Delta P = 20 \text{ psi}$			
	L_b (cm)	r (cm)	Q_p (cm ³ /min)	N_L	L_b (cm)	r (cm)	Q_p (cm ³ /min)	N_L	L_b (cm)	r (cm)	Q_p (cm ³ /min)	N_L
1/8-A-SS-2					2.9	1.3	180	0.62	2.4	1.3	234	0.66
						2.5	103	0.82		5.1	90	1.18
						3.8	80	0.79		8.9	46	1.21
						5.1	42	1.07				
						1.4	189	0.58		1.7	207	0.75
						2.9	112	0.77		3.2	133	0.86
						4.5	73	0.98		4.5	60	0.69
						6.2	30	0.65		6.2	45	1.14
1/8-A-SS-5	4.1	1.3	391	0.21	3.8	1.3	481	0.21	3.2	2.5	411	0.56
		2.5	232	0.38		2.5	262	0.39		5.1	246	0.60
		5.1	150	0.46		6.4	146	0.50		10.2	88	0.64
		8.9	138	0.56		10.2	78	0.53		15.9	38	0.89
		14.0	42	0.57		19.7	8	0.71		22.2	12	0.86
1/4-A-SS-10	5.1	5.7	224	0.36	4.4	3.6	464	0.31	2.9	3.6	626	0.52
		10.2	103	0.52		9.2	125	0.49		8.1	275	0.60
		18.3	15	0.50		13.7	46	0.59		14.8	64	0.65
						18.3	5	0.64		18.3	36	0.69
						24.0	5	0.63				
		3.5	350	0.28		3.5	447	0.44		8.6	234	0.44
		8.6	143	0.40		8.6	184	0.40		13.7	90	0.46
		13.7	58	0.40		13.7	68	0.48		18.7	46	0.54
		18.7	23	0.47		18.7	23	0.51		23.8	25	0.53
						23.8	11	0.56				
						3.5	628	0.44				
						13.7	76	0.54				
						19.1	25	0.41				
						23.8	23	0.47				
	3/8-A-SS-20	5.7	3.2	916	0.16	4.4	3.5	996	0.18			
		7.6	374	0.27		7.6	497	0.38				
		12.7	164	0.39		12.1	188	0.37				
		17.8	82	0.41		17.8	86	0.61				
		24.1	40	0.39		25.4	38	0.51				
		38.7	10	0.45		40.6	10	0.53				

**Table 5.4. Spray mass transfer in pilot scale experiments
(Nozzle: 3CF-SILCNB-120, T = 35-40°C)**

P (psi)	r (m)	Angle (°)	Coded angle	Q _p (cm ³ /min)	Flux cm/s	N _L
5	0.80	51	0	294	1.72	0.33
	1.01	49	0	238	1.39	0.15
	1.19	48	0	194	1.13	0.29
	1.38	47	0	158	0.92	0.30
	1.74	42	-	36	0.21	0.19
	1.74	44	0	78	0.45	0.36
	1.74	44	0	78	0.45	0.37
	1.74	47	0	98	0.57	0.35
	1.75	49	+	30	0.17	0.26
	10	0.74	49	0	407	2.38
0.74		49	0	407	2.38	0.24
0.93		45	-	234	1.37	0.31
0.94		49	0	274	1.60	0.33
1.24		47	0	210	1.23	0.35
1.25		51	+	162	0.95	0.37
1.25		51	+	162	0.95	0.44
1.25		51	+	114	0.67	0.45
1.62		46	0	138	0.81	0.34
1.81		46	0	114	0.67	0.38
1.82		44	-	86	0.50	0.35
1.82		48	0	110	0.64	0.38
1.82		48	0	110	0.64	0.47
1.82		48	0	110	0.64	0.36
1.82		48	0	102	0.60	0.44
1.82	50	+	30	0.17	0.32	
20	1.33	50	0	204	1.19	0.56
	1.53	46	-	194	1.13	0.27
	1.53	48	0	226	1.32	0.34
	1.69	44	-	122	0.71	0.28
	1.69	46	0	202	1.18	0.38
	1.69	49	0	170	0.99	0.51
	1.71	51	+	62	0.36	0.19

In both the laboratory and pilot scale data, the measured N_L values for the spray are low compared to expectations. Based on the discussion and literature review in Chapters 1 and 2, the spray could have been expected to provide 1 to 3 transfer units, but values measured in this work typically ranged from 0.5 to 1.0. This

discrepancy is most likely because previous researchers included the contributions of sample collection and wall effects in their reported values of N_L . Since great care was taken to validate the sample collection methods in this work, the current data should be more representative of the mass transfer occurring in the spray itself.

The unexpectedly large difference between this data and previous work also highlights the significance of mass transfer during spray impact. The mass transfer in a real spray contactor may occur in the spray region, on the walls, or in the accumulated liquid at the bottom of the absorber. Typically, the last two sources are neglected, and the overall performance is attributed to the spray. However, as high velocity liquid impacts surfaces, gas entrainment and turbulent mixing may result. Thus, spray impact on the walls, into liquid surfaces, or with other sprays could greatly increase the mass transfer. These phenomena are discussed further in the next chapter.

5.2.1. Empirical correlations

The experimental values for the spray N_L were empirically correlated in a power law form. The correlations were obtained by a least squares regression, after the equation was linearized by taking logarithms. The confidence intervals correspond to the standard errors of the least squares estimates of the parameters. The data for the smallest nozzle ($\frac{1}{8}$ -A-SS-2) was not included in this regression because the data for this nozzle was significantly different from the rest of the data. The results for the $\frac{1}{8}$ -A-SS-2 nozzle are discussed in more detail later, in Section 5.2.4. In addition, for the 3CF nozzle, only the data for the center of the spray was included in the regression.

Table 5.5 gives the results for an empirical correlation for the spray N_L . A dimensional correlation predicts the spray N_L as a function of nozzle orifice diameter (d_{or} [in]), nozzle pressure drop (ΔP [psi]), and distance (r [in]). A parity plot of the correlated and predicted N_L values is given in Figure 5.4. The nozzle size has the strongest effect on the spray N_L . As the nozzle size is increased, the mass transfer in

the spray decreases. The spray N_L increases slowly with distance and the higher slope close to the nozzle indicates the higher mass transfer rates in the sheet and/or soon after droplet formation. The nozzle pressure drop has only a weak positive effect on the mass transfer in the spray. These effects are discussed in more detail in the following sections.

Table 5.5. Empirical correlation of spray N_L

$N_L = C_0 d_{or}^{C_1} \Delta P^{C_2} r^{C_3}$	
Parameter	Regressed value
$\ln C_0$	-2.51 ± 0.13
C_1	-0.45 ± 0.04
C_2	0.23 ± 0.04
C_3	0.31 ± 0.03

Note: d_{or} and r in inches and ΔP in psi

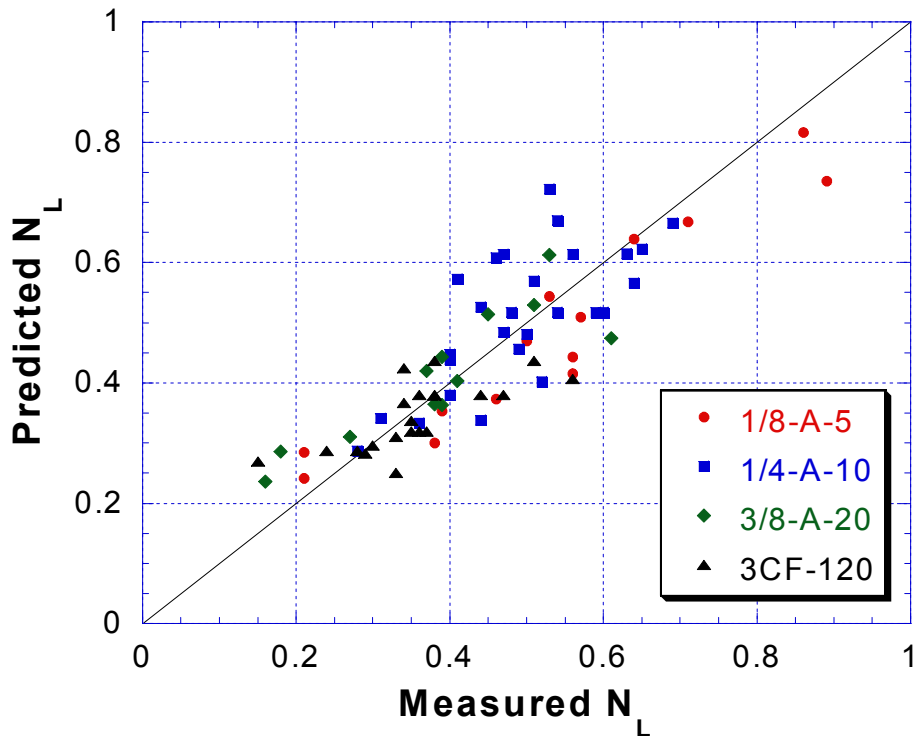


Figure 5.4. Parity plot of empirical spray N_L correlation (Table 5.5)

The second correlation (Table 5.6) is dimensionless and expresses spray N_L as a function of the Reynolds and Weber numbers at the nozzle exit and the distance normalized by the nozzle orifice diameter. In order to account for the higher temperature in the pilot scale experiments, the physical properties were assumed the same as those for water. The density and viscosity as a function of temperature were obtained from Perry's Handbook (Liley et al., 1984), and values for the air-water surface tension were obtained from the CRC Handbook (Weast, 1998).

Table 5.6. Dimensionless correlation of spray N_L

$N_L = C_0 \text{Re}_o^{C_1} \text{We}_o^{C_2} \left(\frac{r}{d_{or}}\right)^{C_3}$	
Parameter	Regressed value
ln C_0	-0.11 ± 0.22
C_1	-0.60 ± 0.08
C_2	0.52 ± 0.08
C_3	0.31 ± 0.03

The negative dependence on Re_o indicates that the greater mass transfer at higher Re_o is not enough to compensate for the corresponding greater liquid flow rate. Since N_L can be viewed as the liquid phase mass transfer capability ($k_L A$) normalized by the liquid flow rate (see Equation 1.4), N_L will decrease if $k_L A$ increases more slowly with Re_o than the liquid flow rate does.

5.2.2. Effect of distance

The mass transfer performance of the 1/8-A-SS-5 spray nozzle is graphed in Figure 5.5 as a function of distance. Mass transfer rates, indicated by the slopes of the data, were very high close to the nozzle and then decreased with distance. At a nozzle pressure drop of 10 psi, an N_L of 0.7 was accomplished within 20 cm of the nozzle. At this pressure, the liquid sheet exiting the nozzle broke into spray droplets at a distance of 3.8 cm, and the spray N_L was already approximately 0.4 at the point of sheet breakup. In the droplet region, the N_L of the spray increased approximately linearly with distance. Since the slope of N_L versus distance was low, the droplets are

expected to add little to the mass transfer of the spray, even at greater distances. Thus, the contribution of the sheet to mass transfer is expected to be substantial even though the sheet region is only a small fraction of the total spray.

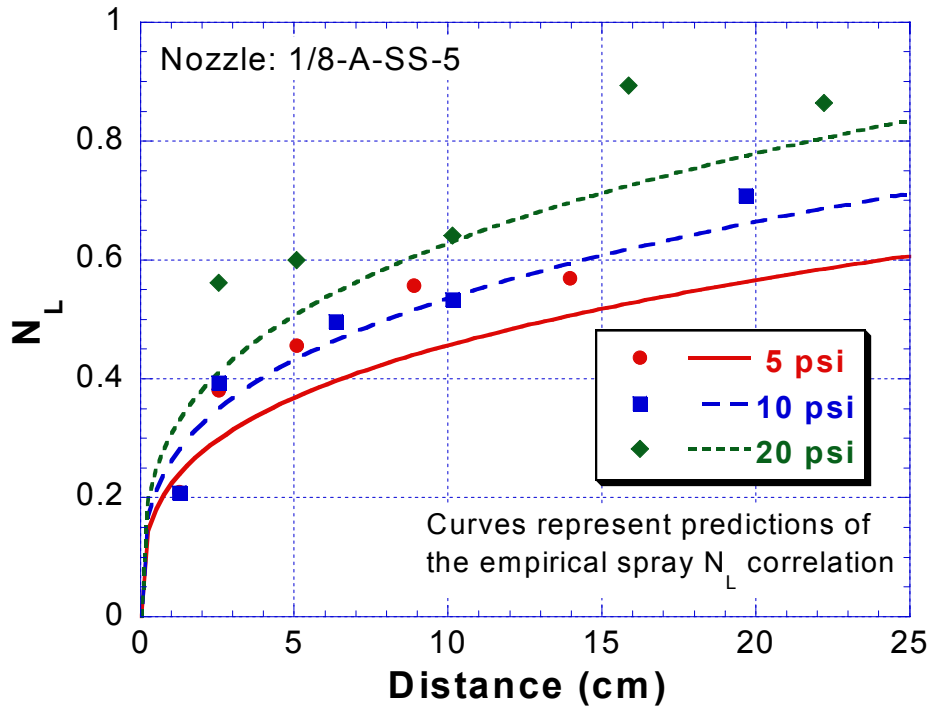


Figure 5.5. Spray mass transfer in laboratory experiments (Nozzle: 1/8-A-SS-5, quench sampler)

A similar effect of distance was observed in the pilot scale experiments as well (Figure 5.6). Again, the slope of the N_L data with distance is low and approximately constant. Unfortunately, the sheet could not be sampled because of limitations on the quench sampler flow rate. Attempts to collect samples at higher spray fluxes resulted in flooding of the sampler. Nevertheless, extrapolating the data back to the point of sheet breakup (approximately zero distance) yields an estimate of the sheet N_L of 0.2. Although the sheet N_L for the 3-inch nozzle is less than that for the 1/8-inch nozzle, the sheet still accounts for about 40% of the total N_L of the spray.

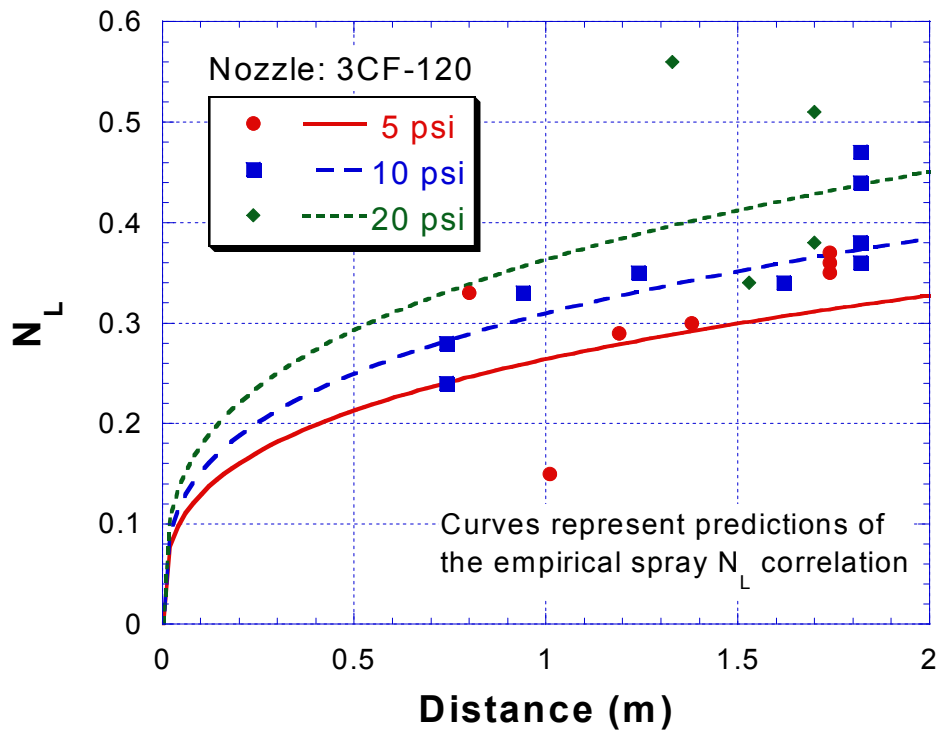


Figure 5.6. Spray mass transfer in pilot scale experiments (Nozzle: 3CF-SILCNB-120, quench sampler)

5.2.3. Effect of nozzle pressure drop

The nozzle pressure drop has little effect on the number of transfer units in the spray. In Figure 5.5, the N_L data at 5 and 10 psi are nearly identical, and the data at 20 psi are only about 0.2 transfer units higher. Although the N_L in the sheet seems slightly higher at 20 psi, it is not a strong function of the pressure drop. In Figure 5.6, even less of an effect of pressure can be observed because of scatter in the data. According to the empirical correlation, N_L varies with pressure drop to the 0.23 ± 0.04 power.

The nozzle pressure drop could have different effects on the mass transfer coefficient, area and contact time in the sheet. As the pressure drop is increased, the shorter sheet breakup length and the higher velocity are expected to result in lower interfacial area per unit liquid volume (a_L) and contact time. However, the higher

pressure drop could also result in a greater k_L . The data suggest that the N_L of the sheet increases slightly with ΔP , so the mass transfer coefficient in the sheet has a stronger dependence on the ΔP than the area or contact time do.

In the spray droplet region, the slope of the 20 psi data is approximately the same as that for the data at 5 and 10 psi. The higher pressure drop results in higher spray velocity and thus shorter contact time in the spray. The higher pressures also generate slightly smaller droplets, which have more area per unit liquid volume. However, the decrease in droplet size is not large enough to compensate for the reduction in contact time, so the mass transfer coefficient of the droplets must be increasing significantly with pressure as well. The higher k_L in the droplets may be due to higher k_L in the sheet, the dependence of the oscillation k_L on droplet size, or a combination of the two.

5.2.4. Effect of nozzle size

As nozzle size is increased, the N_L values as a function of distance decrease. Larger nozzles have thicker sheets and generate larger droplets, which result in substantially lower a_L . Experimental data and correlation predictions for the different spray nozzles operated at 10 psi pressure drop are shown in Figure 5.7. The distance from the nozzle is normalized by dividing by the nozzle orifice diameter. With the exception of the smallest nozzle shown ($1/8$ -A-SS-2), the experimental data for the laboratory scale nozzles almost seem to collapse onto a single curve. The correlated N_L values decrease slightly as nozzle size increases, even after the distance is normalized by the nozzle orifice diameter. The scatter in the experimental data may make it difficult to distinguish trends among the raw data.

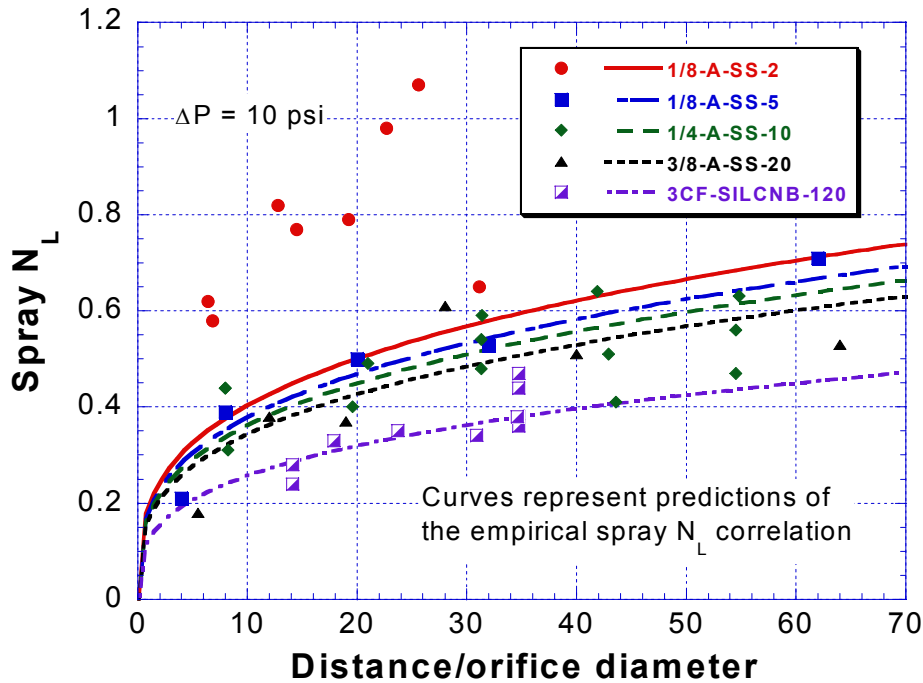


Figure 5.7. Effect of nozzle size on spray mass transfer ($\Delta P = 10$ psi, quench sampler)

The N_L data for the 3-inch nozzle has a similar dependence on spray distance and orifice diameter as the other nozzles, even though the pilot scale nozzle is an order of magnitude larger than the laboratory nozzles and has a flow rate two orders of magnitude larger. On the other hand, the data for the 1/8-A-SS-2 nozzle is noticeably different from the rest of the data, and extrapolating the empirical correlation does not match the data. As mentioned earlier, the data for this nozzle was not included in the regression of the empirical correlations in Table 5.5.

Since the 1/8-A-SS-2 is the smallest nozzle tested, it may be in a different flow regime. To investigate this hypothesis, the Reynolds numbers for the two smallest nozzles are compared in the following table. Re_{pipe} is computed for the flow in the 1/2 inch piping system (schedule 80, i.d. 1.39 cm) and in the pipe immediately upstream of the nozzle (1/8 inch, i.d. 0.683 cm). Re_o is computed as before, for the sheet at the nozzle exit. These Reynolds numbers should determine the flow behavior in the pipe

and the sheet. Finally, the Re for the flow around the droplets (Re_d) is calculated to determine if droplet oscillation is expected.

Table 5.7. Comparison of Re for small nozzles

Nozzle	ΔP	Q (cm ³ /s)	d_{32} (μm)*	Re_{pipe}		Re_o	Re_d
				1/2 inch	1/8 inch		
1/8-A-SS-2	10	12.6	335	1158	2351	2278	216
	20	17.8	307	1638	3325	3216	281
1/8-A-SS-5	5	22.3	439	2048	4156	2580	200
	10	31.5	403	2896	5878	3642	260
	20	44.6	370	4095	8312	5140	338

* See data from Spraying Systems (Appendix A)

The Re_d values for the small nozzles are close to the critical value for the onset of droplet oscillation. As discussed in Chapter 3, droplet oscillation begins at Re_d values of about 200. However, the values for Re_o and Re_d for the 1/8-A-SS-5 nozzle at 5 psi are less than those for the 1/8-A-SS-2 nozzle at 20 psi. Therefore, the flow of the sheet and the droplet behavior are not expected to be very different between the two nozzles and do not explain the dramatic change in the behavior of the small nozzle.

The Reynolds numbers for flow in the pipe upstream of the nozzles do not overlap. For the 1/8-A-SS-2 nozzle, the Reynolds numbers in the 1/2 inch pipe are low enough that the flow is expected to be laminar. At the higher flow rates of the 1/8-A-SS-5 nozzle, the Reynolds numbers are in the transition region to turbulent flow. However, all of the Reynolds numbers in the 1/8 inch pipe indicate turbulent flow conditions. If the flow upstream of the 1/8-A-SS-2 nozzle is laminar, then the laminar flow conditions or entry effects in the short run of 1/8 inch pipe could alter the sheet behavior or breakup phenomena.

The data for the 1/8-A-SS-2 nozzle at 10 and 20 psi are reasonably described by a linear relationship $N_L = 0.0885 r + 0.554$, where the spray distance r is in cm. In the droplet region, the mass transfer coefficient is related to the slope (see Equation 3.40). The droplet k_L is thus estimated to be 0.75 cm/s at 10 psi and 0.97 cm/s at 20

psi. These mass transfer coefficients are greater than most of the droplet models would predict, as shown in the following table. The Ruckenstein circulation model most closely fits the experimental results.

Table 5.8. Comparison of droplet k_L model predictions for 1/8-A-SS-2 nozzle

Model	$\Delta P = 10$ psi	$\Delta P = 20$ psi
Penetration	0.061 cm/s	0.073 cm/s
Oscillation	0.167	0.178
Ruckenstein	0.805	0.999
Handlos & Baron	0.086	0.122
Laddha & Degaleesan	1.208	1.708
Estimated values	0.75	0.97

5.2.5. Summary

The N_L values for sprays were measured using quench sampling methods to eliminate spray impact and sample collection effects. The N_L data were significantly less than other reported data that did not isolate the spray from these effects. Based on these results, only 0.5 to 1.0 of the 1 to 3 transfer units that are expected in a spray may be due to the spray itself. Other sources of mass transfer must exist in a real spray contactor in order to account for the previously reported data, and they would be expected to be similar in magnitude to the spray N_L . The source of the remainder of the mass transfer is discussed later.

In the spray, N_L increased with distance, but the highest mass transfer rates occurred near the nozzles. Even before droplet formation, mass transfer in the sheet provided 40% of the total N_L of the spray. Mass transfer rates in the spray droplets were much lower, and N_L increased approximately linearly with distance from the point of sheet breakup to a spray distance of 70 orifice diameters.

The spray N_L exhibited a weak effect of nozzle pressure, due to the tradeoff between increasing k_L and/or area and decreasing contact time. Larger nozzles gave lower N_L at a given spray distance and nozzle pressure. N_L also had an inverse

dependence on Re_o , indicating that the mass transfer increased more slowly than the liquid flow rate.

5.3. ANALYSIS/CALCULATION OF k_L

After obtaining data for N_L , the next step in analyzing the mass transfer is to separate the effects of the liquid phase mass transfer coefficient and the interfacial area for mass transfer. Two approaches are described in this section: the standard calculation of $k_L a$ and a Lagrangian modeling approach. The $k_L a$ calculation was found to be extremely sensitive to the contactor volume since the spray is conical in the region of interest. Theoretical k_L models for the sheets and droplets were applied and combined with calculated areas and contact times to predict the N_L of the spray.

5.3.1. Calculation of $k_L a$

One of the most common methods of representing liquid phase mass transfer characteristics of a contactor is $k_L a$, the mass transfer capability normalized by the contactor volume. Sometimes, the area per unit contactor volume can be determined independently, and then k_L can be calculated. In order to calculate $k_L a$ for the spray, an effective contactor volume was defined as a function of distance from the spray nozzle (Figure 5.8).

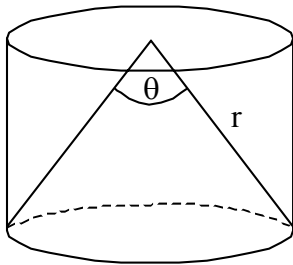


Figure 5.8. Calculation of effective contactor volume

Thus, the effective contactor volume V_c was calculated, and the data for N_L was transformed into values for $k_L a$ using the liquid flow rate and the effective contactor volume.

$$V_c = \pi \left[r \sin\left(\frac{\theta}{2}\right) \right]^2 \left[r \cos\left(\frac{\theta}{2}\right) \right] = \pi r^3 \sin^2\left(\frac{\theta}{2}\right) \cos\left(\frac{\theta}{2}\right) \quad (5.7)$$

$$k_L a = \frac{k_L A}{V_c} = \frac{N_L Q_L}{V_c} \quad (5.8)$$

The calculated values for $k_L a$ varied greatly with position in the spray. For comparison with literature, $k_L a$ values far from the nozzle were used. These values ranged from about 0.005 to 0.050 s^{-1} , which are close to the 0.002 to 0.018 s^{-1} range of Mehta and Sharma (1970) and Pinilla et al. (1984). The calculated $k_L a$ values are also the same order of magnitude as values expected for spray extraction ($\sim 10^{-3} s^{-1}$) according to Seibert (1988).

The $k_L a$ data were then regressed as a power law in Re_o , We_o , and η , where η is a dimensionless contact time. The Re_o and We_o were expected to describe the mass transfer occurring initially in the sheet. The variation of N_L with distance or contact time was then expected to be a function primarily of the droplets. Based on the work of Hughes and Gilliland, the mass transfer of the droplets was expected to vary as viscosity dampened the droplet oscillations. Thus, η is defined as the contact time divided by a characteristic time scale for viscous damping, or

$$\eta = \frac{r/U_o}{\rho d^2/\mu} = \frac{r\mu}{\rho d^2 U_o} \quad (5.9)$$

The $k_L a$ correlation is given in Table 5.9 and in Figure 5.9. As in the dimensionless N_L correlation, $k_L a$ has a negative dependence on the sheet Reynolds number. The sheet Weber number has a weaker effect on $k_L a$, and the uncertainty in value of the exponent is relatively high. The parameter with the smallest uncertainty is the exponent on η , but the dependence of $k_L a$ on η is mostly due to the calculation of the contactor volume.

Table 5.9. Correlation of spray $k_L a$

$k_L a = C0 Re_o^{C1} We_o^{C2} \eta^{C3}$	
Parameter	Regressed value
ln C0	-3.75 ± 0.24
C1	-1.47 ± 0.07
C2	0.67 ± 0.08
C3	-2.69 ± 0.03

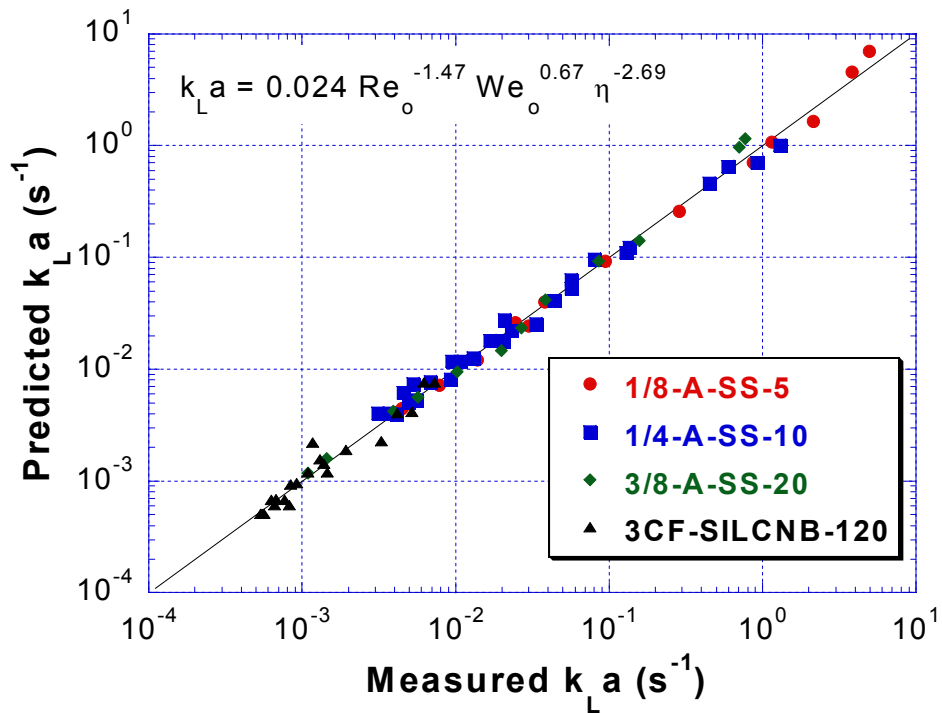


Figure 5.9. Parity plot for $k_L a$ correlation (Table 5.9)

The parity plot in Figure 5.9 also shows that the $k_L a$ values cover a wide range, almost four orders of magnitude from 6×10^{-4} to 5 cm/s . The wide variation in the $k_L a$ values is a result of vastly different contactor volumes and the high interfacial area of the sheet. In Equation 5.7, the effective contactor volume varies with r^3 so Equation 5.8 is normalizing the mass transfer by a volume that changes dramatically as distance from the nozzle is increased. In addition, much of the additional volume

does not contain spray, since the droplets are not well distributed over the contactor volume.

Close to the nozzle, high interfacial area in the sheet, normalized by the small contactor volume, contributes to extremely high values of $k_L a$. Far from the nozzle, the droplets contribute little additional area, but since the contactor volume increases with r^3 , the $k_L a$ decreases rapidly. On the other hand, the liquid flow rate is constant, regardless of the effective contactor volume. For these reasons, normalizing the mass transfer by the liquid flow rate is preferred instead of normalizing by the contactor volume, and expressing spray mass transfer in terms of N_L is better than using $k_L a$.

5.3.2. Comparison with Levich-Davies theory

The magnitude of the sheet N_L is much higher than the laminar sheet model would predict. Although the critical Reynolds number for transition from laminar to turbulent flow in a sheet is unclear, the high mass transfer rates suggest that turbulence is enhancing the mass transfer in the sheet. Instead of using purely empirical effective diffusion coefficients as other researchers have done, the Levich-Davies model was applied. This model has the advantage of being at least somewhat predictive, so that separate empirical constants (effective diffusion coefficients, penetration times, surface renewal rates, etc.) do not have to be assumed for each set of operating conditions.

The N_L data for the 1/8-A-SS-5 nozzle are compared with model predictions in Figure 5.10. The lines represent model predictions, which were calculated with an empirical factor (α) of 3.0 included in the Levich-Davies model for the sheet k_L (see Equation 3.8 and Section 3.2.3.1). The area and contact time of the sheet were calculated using the empirical sheet breakup lengths in Equations 3.29 and 3.30. At sheet breakup, the droplets were assumed to form immediately, i.e. the ligaments and secondary breakup were neglected. The k_L of the droplets was initially equal to the sheet k_L and decayed exponentially to the steady state value for oscillating droplets according to Equation 3.38. The trajectory and thus the contact time of the droplets

were calculated by a drag calculation, in which the differential equations were solved using a Runge-Kutta numerical integration.

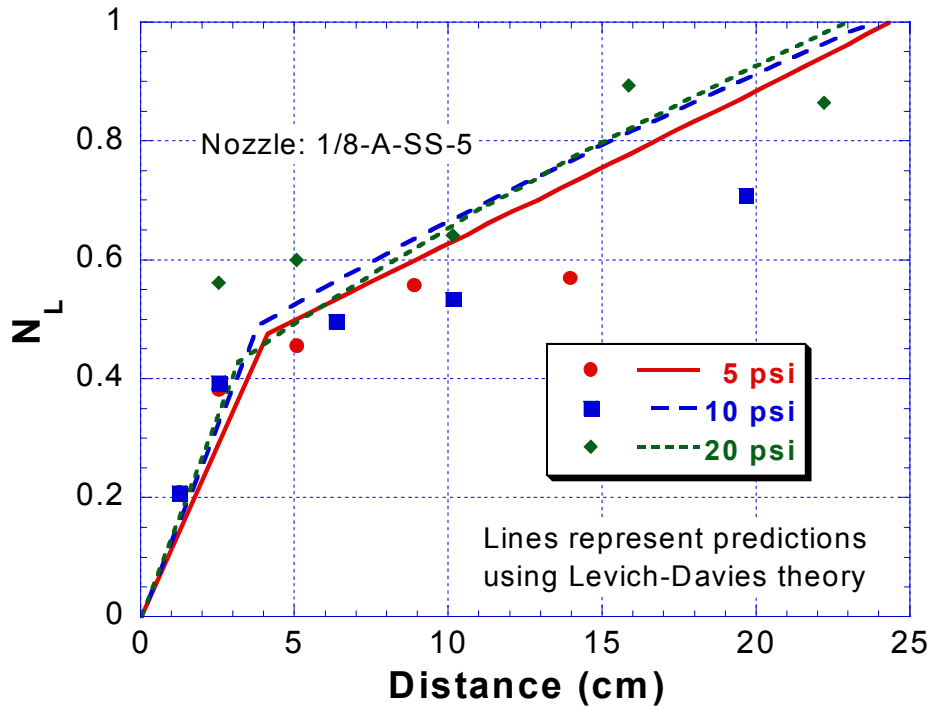


Figure 5.10. Comparison of spray mass transfer with Levich-Davies calculation (Nozzle: 1/8-A-SS-5)

Initially, the Levich-Davies model for turbulent mass transfer underpredicted the mass transfer in the sheet. Since other experimental investigations of this model (Davies and Hameed, 1971; Srinivasan and Aiken, 1988) also demonstrated uncertainty in the coefficient of the expression, the empirical factor α was introduced to match the model predictions to the experimental data. With an α of 3.0, the calculated N_L values match the data for the laboratory nozzles fairly well and show practically no dependence on pressure drop.

In the sheet, the higher pressure drop results in shorter breakup lengths and therefore less area and contact time. However, the mass transfer coefficient predicted by the Levich-Davies model increases, and the overall effect is that the mass transfer in the sheet is essentially independent of nozzle pressure. In the droplets, the higher

pressure results in smaller droplets, which have more area per unit volume. Since the k_L for an oscillating droplet increases with decreasing droplet size, the droplet k_L increases with pressure as well. However, the higher nozzle pressures result in higher initial velocities for the droplets. According to the drag calculation, the droplets did not have enough time to decelerate to their terminal velocities. Thus, the higher droplet velocities reduce the contact time and offset the increase in $k_L a_L$.

Results for all of the nozzles at 10 psi are compared with model predictions in Figure 5.11. Again, the lines represent model predictions for the laboratory nozzles, and the distance from the nozzle is normalized by the nozzle orifice diameter. The order of magnitude of the model predictions match the experimental data, but the model tends to overestimate the effect of nozzle size. The data for the $\frac{1}{8}$ -A-SS-2 nozzle is unusual, as discussed in Section 5.2.4. The data for the other laboratory nozzles appear to have the same dependence on normalized distance, but the model predicts significantly less mass transfer as the nozzle size increases from the $\frac{1}{8}$ -A-SS-5 to the $\frac{3}{8}$ -A-SS-20 nozzle, particularly in the sheet.

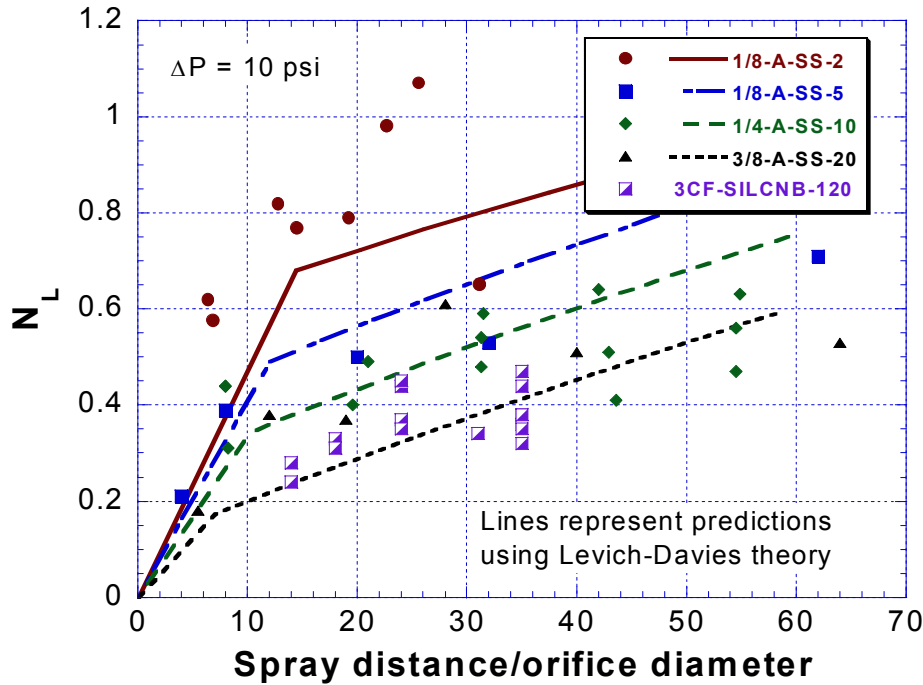


Figure 5.11. Comparison of spray mass transfer with Levich-Davies calculation ($\Delta P = 10$ psi)

The model does not predict the effect of nozzle size on the sheet mass transfer well. As the nozzle size is increased from the 1/8-A-SS-5 to the 3/8-A-SS-20, the N_L data for the sheet do not change significantly. Even the data for the 3CF-SILCNB-120 nozzle shows only a slightly lower sheet N_L . The model, on the other hand, predicts that the sheet mass transfer decreases significantly for the laboratory nozzles. Therefore, the Levich-Davies model is not a good method for predicting the mass transfer coefficient in the sheet.

Since the droplets do not have sufficient time to decelerate, their contact time is very short. As a result, the mass transfer coefficients of the droplets do not decay very much due to viscous damping, and no curvature can be observed in the N_L data as a function of distance. In Figure 5.11, the curves for the model predictions have slightly higher slopes than the data, except for the 1/8-A-SS-2 nozzle. Thus, it may not be reasonable to assume that the initial k_L of the droplet is equal to the k_L of the sheet.

5.3.3. Semi-empirical model

In light of the weaknesses in the previous model formulation, a semi-empirical model was developed. The area and contact time for the sheet and the droplets were calculated as described in Chapter 3. The k_L of the sheet was correlated empirically, and the k_L of the droplets was calculated semi-empirically.

5.3.3.1. Sheet k_L model

The mass transfer coefficient of the sheet was regressed as a power law, similar in form to the Levich-Davies model and others in the literature described in Chapter 3. Therefore, the mass transfer coefficient of the sheet is assumed to be of the form

$$\text{Sh} = \frac{k_{L,s} h_o}{D} = \begin{cases} C_0 \text{Re}_o^{C_1} \text{We}_o^{C_2} \text{Sc}^{1/2} \left(\frac{r}{L_b} \right)^{C_3} & \text{if } r \leq L_b \\ C_0 \text{Re}_o^{C_1} \text{We}_o^{C_2} \text{Sc}^{1/2} & \text{if } r > L_b \end{cases} \quad (5.10)$$

The k_L , in dimensionless form as the Sherwood number, was expressed as a function of the Reynolds number, the Weber number, and the Schmidt number. Although the Schmidt number dependence was not tested, a square-root dependence was assumed, as suggested by the vast majority of mass transfer models and data in the literature. The diffusion coefficient for CO_2 in water was calculated by the correlation of Versteeg and van Swaaij (1988):

$$D_{\text{CO}_2} [\text{cm}^2/\text{s}] = 0.0240 \exp(-2122/T[\text{K}]) \quad (5.11)$$

Since some of the experimental data points were in the sheet, a term was also included for the position in the sheet. For the rest of the data taken in the droplet region, the contribution of the sheet k_L to the total spray N_L was included by setting the sheet length equal to L_b .

5.3.3.2. Droplet k_L model

As mentioned previously, the contact time of the droplets was so short in the spray experiments that the effects of deceleration and viscous damping could not be

observed. Since the calculated droplet velocity did not change much, it is assumed constant to simplify the calculation. The data indicate that N_L increases effectively linearly with distance in the droplet region. The slope of N_L vs. distance is consistent with the steady oscillating droplet model for k_L . In order to test the sensitivity of the model to the droplet k_L , a semi-empirical expression for the droplet N_L was used.

$$N_{L,d} = C4 k_{L,d} \left(\frac{6}{d_{32}} \right) \left(\frac{r - L_b}{U_o} \right) \quad (5.12)$$

The parameter C4 was varied to match the experimental data and test how well the oscillation model described the droplet mass transfer. For experimental data with single droplets, Altwicker and Lindhjem (1988) found that the accuracy of the Angelo et al. (1966) oscillation model was improved if ε is set at zero and an oscillation time twice that of Lamb (1945) is used. Based on the work of and Hsu and Shih (1993), the oscillation model is expected to predict droplet k_L well if C4 in Equation 5.7 is equal to 0.78 ± 0.21 .

5.3.3.3. Regression results

The regression was performed on the data for the 1/8-A-SS-5 through 3CF-SILCNB-120 nozzles. The sum of the squared residuals between the data and the predicted N_L values was minimized using the Solver function in Microsoft Excel. The regressed parameters are given below in Table 5.10, with results of a sensitivity analysis. The column labeled sensitivity is the effect of a 10% increase in the parameter on the residual sum of squares. The columns labeled “confidence interval” are another way of expressing the sensitivity of the model to each parameter. These numbers are the change in each parameter necessary to increase the residual sum of squares by 100%.

Table 5.10. Regressed parameters and sensitivity for semi-empirical model

Parameter*	Regressed value	Sensitivity	Confidence Interval	
C0	1.64×10^{-4}	25%	-19.9%	19.9%
C1	0.81	2745%	-3.1%	2.6%
C2	0.84	1578%	-3.9%	3.1%
C3	-0.99	1.65%	-135%	60%
C4	0.36	3.72%	-52%	52%

* As defined by Equations 5.10 and 5.11

C1 and C2 are the most sensitive parameters in the regression, as can be seen by the high sensitivities and narrow confidence intervals. As shown in Equation 5.10, C1 represents the Re_o dependence and C2 the We_o dependence. The dependence of Sh on Re_o does not match any of the mass transfer models discussed in Chapter 3, but the value of C1 does fall within the range covered by those models (0.5 to 1.5). The exponent on We_o is higher than expected since only the Levich-Davies model included a Weber number dependence and that was only 0.5.

The regression is least sensitive to parameters C3 and C4, which represent variation of the sheet k_L with distance and the correction for the droplet k_L , respectively. The uncertainty in C3 was large partly because relatively few data points were taken in the sheet. The uncertainty in C4 was high because the slope of N_L with distance was low and scatter in the data limited the precision with which the slope could be estimated. However, it is interesting to note that the value of C4 is 0.36, lower than the expected value based on single droplet studies. Data in the literature support a semi-empirical value of 0.78 ± 0.21 , which lies just outside of the confidence interval estimated for C4. Thus, the mass transfer coefficients in the spray droplets appear to be less than they would be for single droplets.

The predictions of the semi-empirical model are compared with experimental N_L values in Figure 5.12. Data at 10 psi pressure drop are included for all of the nozzles. The semi-empirical model fits the data much better than the model based on the Levich-Davies theory and about as well as the empirical power law regression in Section 5.2.1. If all of the experimental data (except for the 1/8-A-SS-2 nozzle) is

compared with the predictions of the semi-empirical model, an R^2 value of 0.74 is obtained. The empirical correlation (Table 5.5) has a corresponding R^2 of 0.72. As before, the data for the $\frac{1}{8}$ -A-SS-2 nozzle does not follow the same trend as the rest of the data, and extrapolating the semi-empirical model to conditions for the smallest nozzle does not match the experimental data well. However, a comparison of Figure 5.7 and Figure 5.12 reveals that the extrapolation of the semi-empirical model is slightly better than the empirical correlation at describing the higher N_L for the $\frac{1}{8}$ -A-SS-2 nozzle.

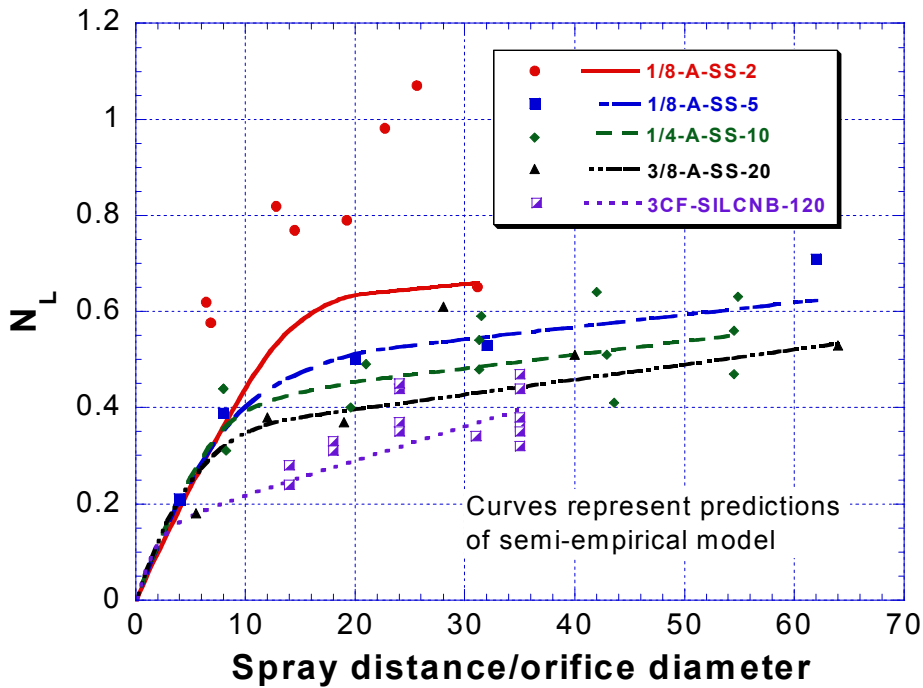


Figure 5.12. Semi-empirical model results ($\Delta P = 10$ psi)

The N_L of the sheet decreases with increasing nozzle size because the sheet thickness is much greater and the area per unit volume is much less. The calculated a_L of the sheet decreases from about 150 cm^{-1} for the $\frac{3}{8}$ -A-SS-20 nozzle to about 5 cm^{-1} for the 3CF-SILCNB-120 nozzle. However, the sheet N_L does not decrease as dramatically. The contact time of the sheet increases slightly since the sheet length is greater for the larger nozzles but not enough to offset the decrease in area. The

relatively weak effect on N_L despite the wide range of a_L indicates that the sheet mass transfer coefficient is much higher for the large nozzle. Experimental $k_{L,s}$ values were calculated from the data as follows

$$k_{L,s} = \frac{N_{L,s}}{a_{L,s} t_s} = \frac{N_L - N_{L,d}}{a_{L,s} t_s} = \frac{N_L - C4 k_{L,d} \left(\frac{6}{d_{32}} \right) \left(\frac{r - L_b}{U_o} \right)}{a_{L,s} t_s} \quad (5.13)$$

In Figure 5.13, the semi-empirical model predictions for the sheet k_L are graphed versus values calculated from the data.

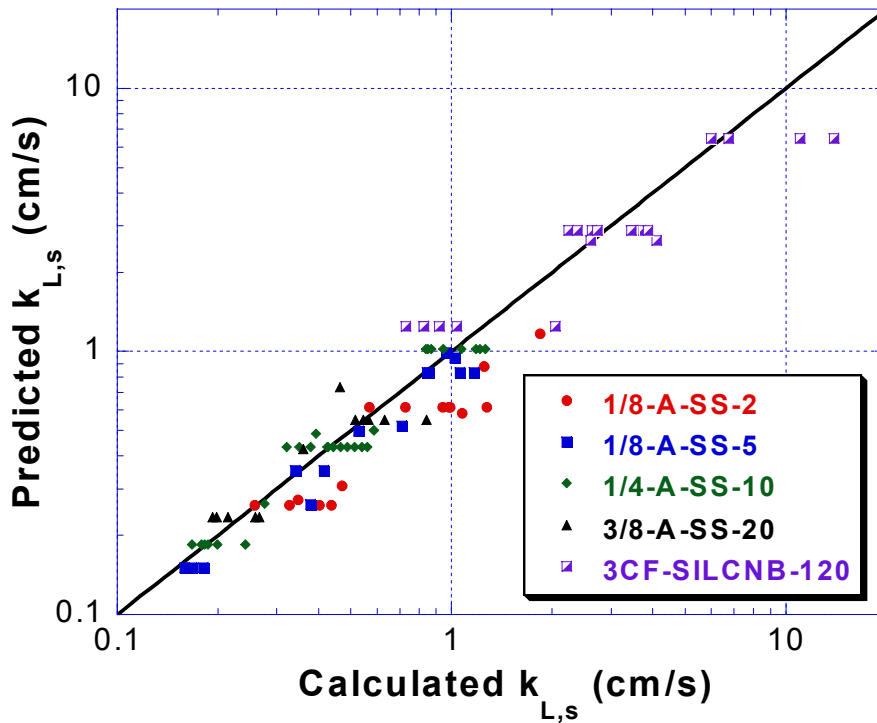


**Figure 5.13. Parity plot of sheet mass transfer coefficients
(Predicted - Equation 5.10, calculated - data and Equation 5.12)**

The semi-empirical model predictions for $k_{L,s}$ ranged from 0.15 to 1.2 cm/s for the laboratory nozzles and from 1.2 to 6.4 cm/s for the 3CF-SILCNB-120 nozzle. As mentioned previously, the sheet N_L does not change much over the range of nozzle pressures or the wide range of nozzle sizes. Since increasing pressure decreases the

sheet length and therefore both the sheet area and contact time, the slightly higher sheet N_L implies that $k_{L,s}$ must increase a great deal with pressure.

5.3.3.4. Model interpretation

The effects of the different operating parameters on the predicted values for k_L are shown in Figure 5.14. Model predictions are given for the smallest and largest nozzles used in the regression ($1/8$ -A-SS-5 and 3CF-SILCNB-120, respectively) and for nozzle pressures of 5 and 20 psi. When the predicted k_L values are graphed as a function of distance, the vast difference between the mass transfer coefficients for the sheet and droplet regions is apparent. Within the sheet, the model predicts that the average k_L of the sheet decreases with distance. Since relatively few measurements were taken in the sheet, the rate of this decrease is subject to significant uncertainty. After the sheet breaks into droplets, the k_L values are about an order of magnitude lower and remain constant as a function of distance.

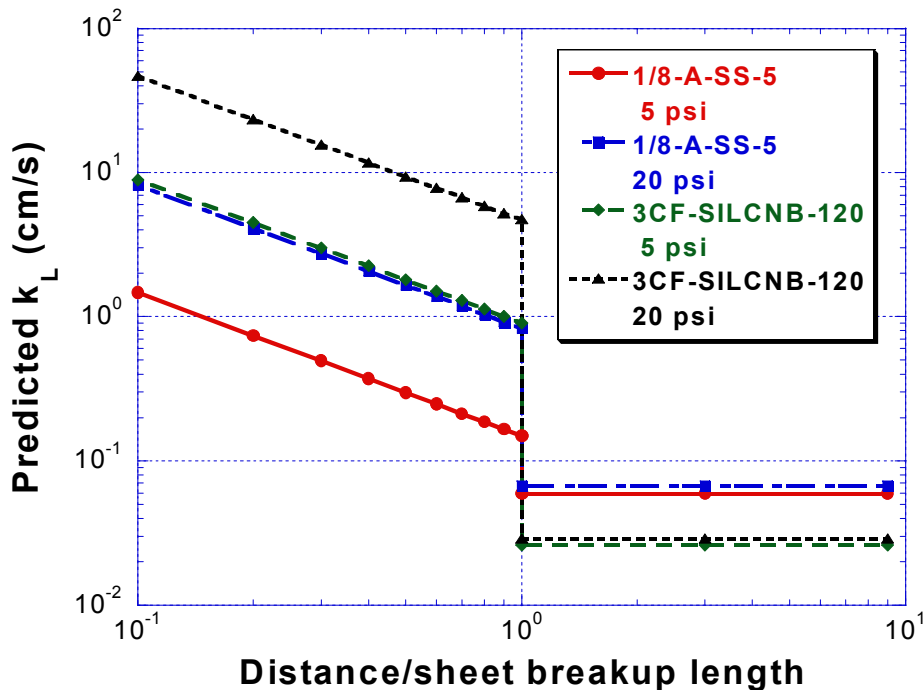


Figure 5.14. Model predictions of sheet and droplet k_L as a function of distance (calculations based on physical properties at 22°C)

The predicted mass transfer coefficients for the sheet increase dramatically as the nozzle size and operating pressure are increased. The sheet for the 3CF-SILCNB-120 nozzle has k_L values 5.9 times higher than the k_L values for the $\frac{1}{8}$ -A-SS-5 nozzle. Similarly, the predicted k_L values at a nozzle pressure of 20 psi are 5.4 times higher than the predictions at 5 psi.

The operating parameters have a different effect on the k_L of the droplets. The nozzle pressure has a weaker effect on the droplet size and the droplet k_L . At 20 psi, the predicted k_L for the droplets is only 14% higher than at 5 psi. As the nozzle size is increased, the droplet size increases and the predicted k_L of the droplets decreases by 57%. As a result, the mass transfer coefficients of the sheets and the droplets diverge as the nozzle size is increased. For small nozzles, the k_L values of the sheet and droplets approach each other, but for large nozzles, the k_L of the sheet is orders of magnitude higher than that of the droplets.

The model predictions for the droplet mass transfer coefficients are compared with literature values in Figure 5.15. The solid line represents the model of Angelo et al. (1966) with $\alpha = 0$. The semi-empirical droplet model of Hsu and Shih included a factor of 0.78 ± 0.21 to match the literature data. The results of the current work for sprays indicated a semi-empirical factor (C4) of 0.36. As seen in Figure 5.15, this work predicts droplet k_L values consistently lower than the literature data for single droplets. Perhaps the presence of other droplets affects the flow of gas around individual droplets and thus affects the wake shedding phenomena, which are thought to drive the droplet oscillations.

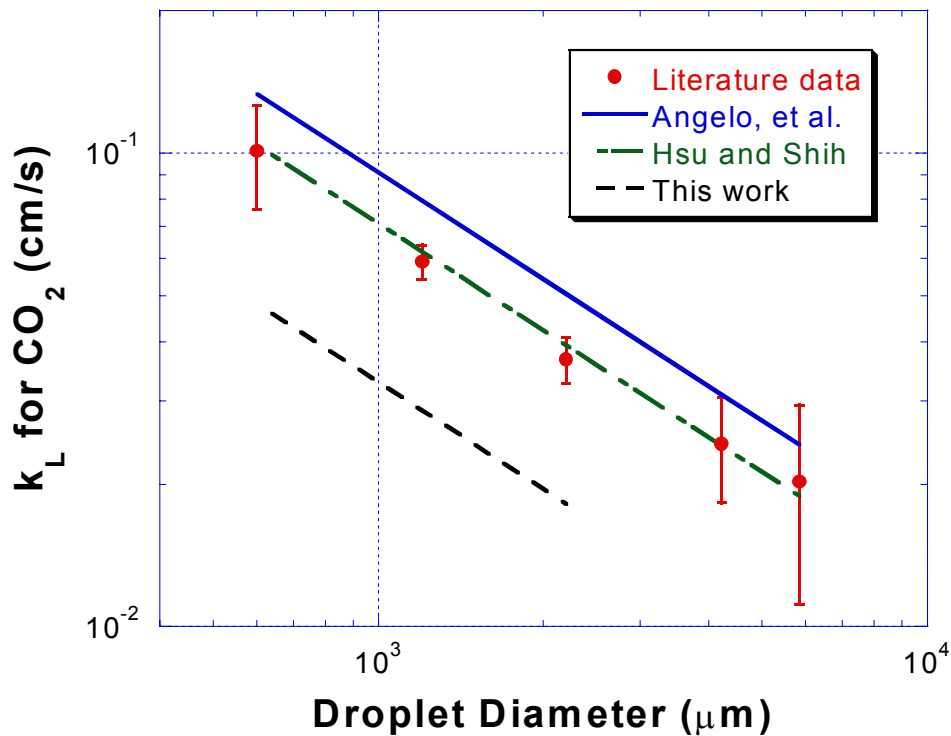


Figure 5.15. Comparison of semi-empirical model predictions with literature data for droplet k_L

The contributions of the mass transfer coefficient and interfacial area to the total N_L are illustrated in Figure 5.16 for the $\frac{1}{4}$ -A-SS-10 nozzle at 5 psi pressure drop. Predicted values for the area per unit liquid volume, the mass transfer coefficient, and the product ($k_L a_L$) are graphed as a function of distance. The resulting predictions for N_L are also compared with the experimental data. The calculated area of the sheet is a strong function of distance and increases to 330 cm^{-1} at the point of sheet breakup. To match the experimental N_L data, the regressed values for sheet k_L decrease sharply with distance.

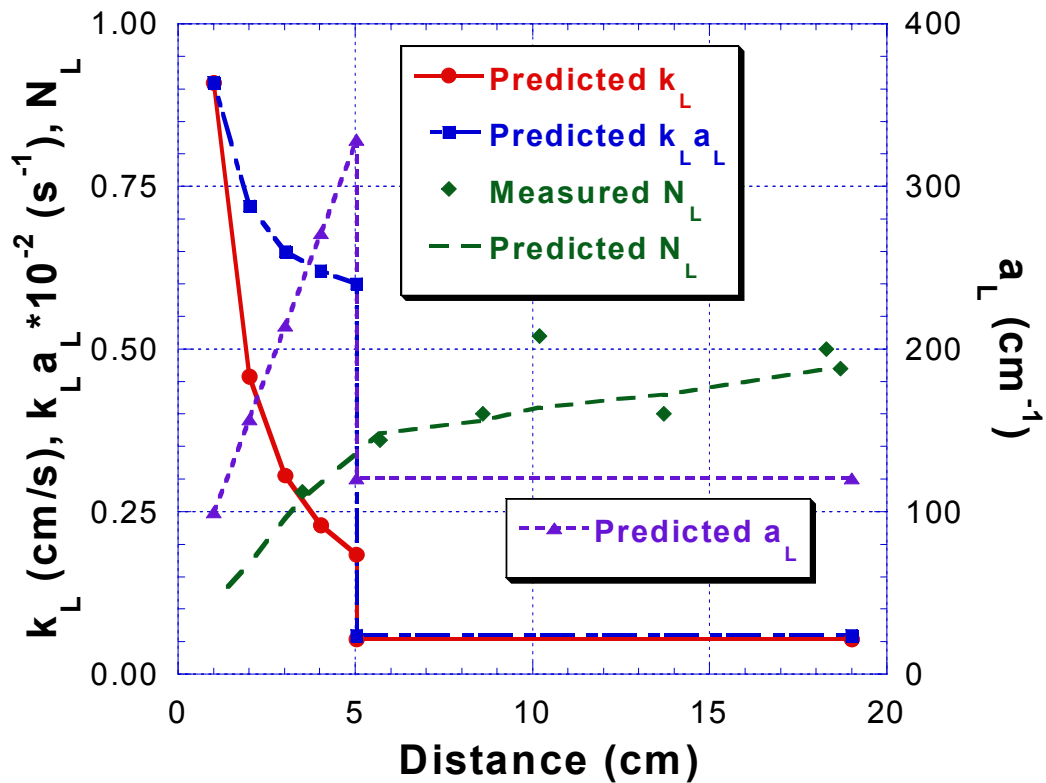


Figure 5.16. Comparison of k_L , area, and N_L predictions with experimental data (Nozzle: 1/4-A-SS-10, $\Delta P = 5$ psi, correlated $L_b = 5.03$ cm)

After the sheet breaks into droplets at a distance of about 5 cm, the model assumes constant k_L and area for the spray droplets. Since both k_L and area of the droplets are much lower than in the sheet, the $k_L a_L$ and the slope of the N_L curve are lower as well. Although the values for k_L and area were calculated and not verified experimentally, the predicted values for N_L are in close agreement with the experimental data points.

5.4. SUMMARY

The measured N_L values for sprays were significantly less than other reported data that did not separate the spray N_L from spray impact and sample collection effects. The spray contributes only 0.5 – 1.0 to the 1 – 3 transfer units expected for a spray column. A real spray contactor must benefit from other mass transfer

phenomena in order to account for the data in the literature, and these effects would be expected to be similar in magnitude to the spray N_L .

In the spray, N_L increased with distance, but the highest mass transfer rates occurred near the nozzles. Even before droplet formation, mass transfer in the sheet provided 40% of the total N_L of the spray. Mass transfer rates in the spray droplets were much lower, and N_L increased approximately linearly with distance from the point of sheet breakup to a spray distance of 70 orifice diameters.

A semi-empirical model was developed to describe the spray N_L data. This model predicts very high a_L in the sheet and models k_L for the sheet with a turbulent mass transfer correlation and k_L for the droplets with an oscillation model. Even with the high calculated area, high values for $k_{L,s}$ are required to achieve measurable N_L in the sheet. Correlated $k_{L,s}$ values for the laboratory nozzles are 0.1 to 1.0 cm/s. Although a_L decreases by as much as two orders of magnitude between the laboratory and pilot scale nozzles, the N_L decreases only slightly, indicating that $k_{L,s}$ for the pilot scale nozzle is even higher.

Chapter 6: Mass transfer during spray impact

In a real spray tower, other opportunities for mass transfer exist besides the spray region. As a result, measurements of the mass transfer in a spray were significantly lower than expected values for the mass transfer in a spray column. The spray N_L includes mass transfer during droplet formation and droplet motion through the continuous phase. However, the spray N_L does not include interaction of the spray with other parts of a real spray contactor, e.g. wall effects or interference with adjacent sprays.

Previous researchers neglected mass transfer on the walls for various reasons – inability to separate spray from liquid running down the walls, area on the wall estimated to be much less than area of the droplets, etc. However, the impact event could provide significant mass transfer by increasing k_L through turbulent surface renewal. The interfacial area at the point of impact could also be increased if droplets shatter into smaller droplets or if gas is entrained with the droplets into an accumulated liquid layer. In addition, the effect of spray impact is expected to be independent of the nozzle type – whether hollow cone or full cone. Whatever the spray pattern, when the droplets impact surfaces at high velocity, significant mass transfer could occur.

The N_L data obtained during the sampler development indicate that spray impact could be as important as the mass transfer in the spray is. In a real contactor, spray is expected to encounter other spray, solid surfaces, and/or liquid pools. Mass transfer measurements for these types of spray impact were performed in the laboratory and are discussed in this chapter.

6.1. IMPACT INTO LIQUID

When high velocity spray droplets strike a liquid surface, several physical processes may contribute to additional mass transfer. The impact generates surface motion in the liquid, and this results in a higher mass transfer coefficient than might

be expected for a stagnant pool of liquid. Splashing and mixing at the surface of these liquids also increase mass transfer. In addition, as the droplets penetrate the liquid surface, they entrain gas into the liquid and provide additional gas-liquid contact area. As the entrained gas bubbles back to the surface, the liquid is circulated and a frothy mixture may result. Similar processes are used to model emissions from wastewater treatment units and sewer drop structures (Corsi and Olson, 1998).

6.1.1. Experimental methods

Experiments were conducted with the 1/4-A-SS-10 nozzle to measure the significance of mass transfer during spray impact into pools of liquid. Spray was collected in a simple sampler with no packing or quench solution (Figure 6.1). Similar to the other samplers described in Chapter 4, the pool sampler consists of an acrylic tube with inner diameter of 3/4" and 4" in length. Liquid is withdrawn continuously and the spray flow rate was measured using a peristaltic pump. Since the ratio of the sample flow rate to the spray flow rate did not affect the sampler development (see Section 4.5.2), the liquid level was maintained at the top of the sampler and about 5% of the liquid was allowed to overflow.

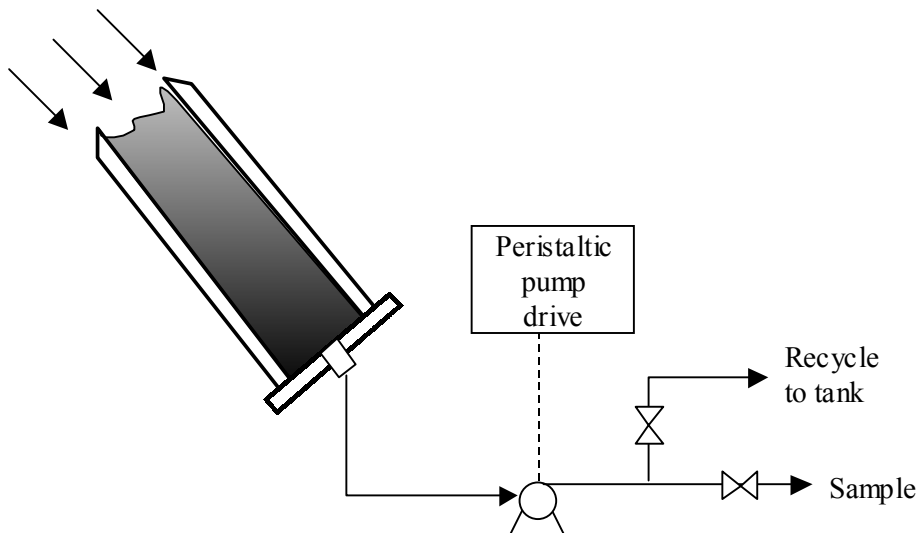


Figure 6.1. Sampler for spray impact into liquid

The mass transfer during impact was expected to vary with the velocity of spray striking the liquid surface and with the flow rate of spray. The operating pressure of the nozzle was varied to study the effect of spray velocity, and the spray distance was varied to measure the effect of spray flux on the mass transfer. The N_L measured using the pool sampler was compared with the spray N_L obtained with the quench sampler. Since the quench sampler did not contribute additional mass transfer, the difference between these measurements is the mass transfer in the pool sampler.

The mass transfer in the pool sampler should be representative of spray impact in pools of accumulated liquid. In a spray column, this type of mass transfer might be expected in the bottom of the absorber, where liquid is collected. In a wet FGD scrubber, this would occur on the surface of the liquid in the reaction tank. These experiments can also represent the mass transfer with spray impact onto a tray.

6.1.2. Results

The mass transfer data for the pool mass transfer experiments are compared with data for the spray N_L in Figure 6.2. The solid data points were measured with the pool sampler. Therefore, these values include both the mass transfer of the spray and the mass transfer in the liquid pool of the sampler. The hollow data points represent data collected using the quench sampler, and the associated lines represent the predicted values according to the empirical correlation (Table 5.5).

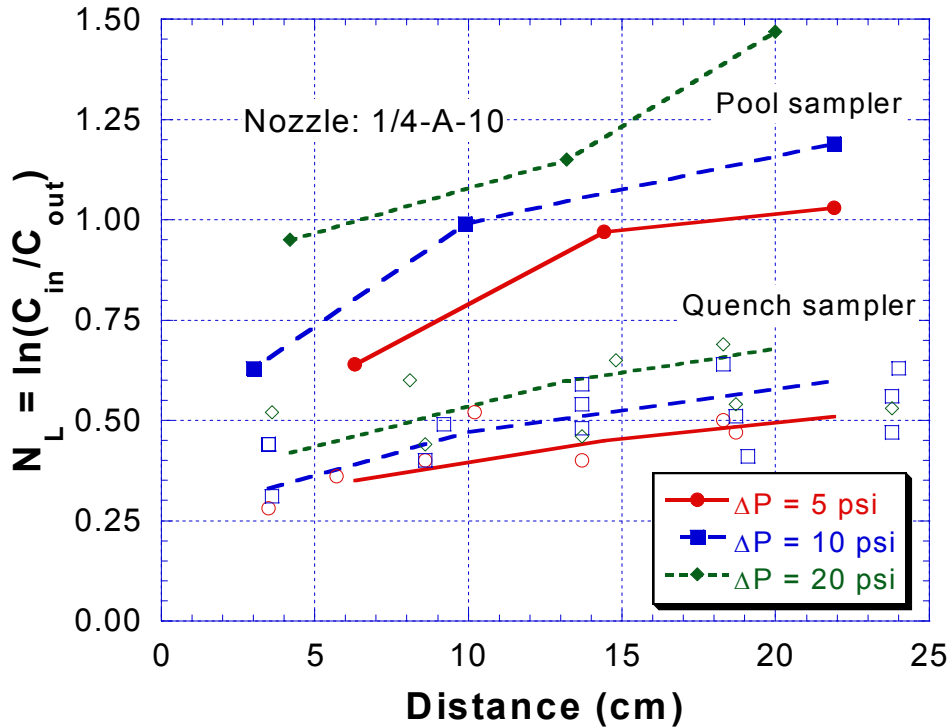


Figure 6.2. Comparison of pool sampler and quench sampler results (Solid points – pool sampler, hollow points – quench sampler)

Under all the experimental conditions, the N_L measured with the pool sampler was markedly higher than the spray N_L , measured with the quench sampler. In many cases, the N_L was twice as high as the spray N_L . The mass transfer also increased faster with distance than the spray N_L correlation does. Since the velocity of spray droplets did not change much over the short spray distances, the pool mass transfer increases as the spray flux decreases. The effect of operating pressure on the observed N_L is also more significant than it was for the spray N_L measurements. Therefore, the data also indicate that the pool mass transfer increases with higher nozzle pressure or spray velocity.

6.1.3. Analysis

The pool mass transfer was calculated as the difference between the N_L values measured with the pool sampler and the predictions of the spray N_L correlation. The

results for the pool N_L are graphed in Figure 6.3. The values for the pool N_L range from 0.3 to 0.8 transfer units. Since the spray N_L values at the same conditions were between 0.25 and 0.75, the mass transfer in the liquid of the sampler must be comparable to the mass transfer in the spray. This somewhat surprising result highlights the importance of reliable sample collection in determining mass transfer in sprays. In addition, these results also suggest that more efficient contactor designs may be able to take advantage of N_L during spray impact.

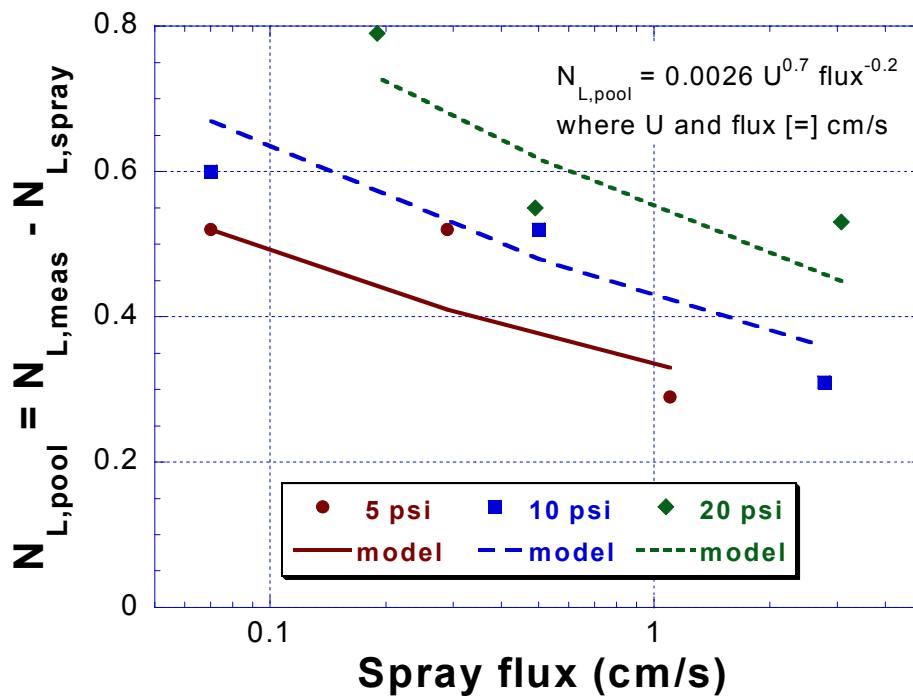


Figure 6.3. Pool mass transfer
(Nozzle: ¼-A-SS-10, model curves from Equation 6.1)

The pool N_L was correlated with the spray velocity and the spray flux. The pool mass transfer had a strong dependence on the velocity with which spray struck the liquid surface. As the distance from the nozzle was increased from 5 to 20 cm, the flux decreased dramatically from 3.0 to 0.07 cm/s, and the pool N_L increased. Although the exponent of the flux is small, the flux varies over a wide range so the pool N_L changes significantly over the relatively small range of spray distance.

The pool N_L correlation can also be expressed in terms of the velocity and the liquid fraction, like the overflow sampler correlation (Equation 4.5).

$$N_L = 0.0026U_o^{0.7}(\text{flux})^{-0.2} = 0.0026U_o^{0.5}f^{-0.2} \quad (6.1)$$

Given the uncertainty in the correlations, Equations 4.5 and 6.1 are very similar. Thus, the mass transfer in the pool sampler and the overflow sampler are equivalent, and these results may be applied to spray impact onto wetted or flooded packing as well. The impact of the spray onto packing and the liquid on top of the packing can provide substantial liquid phase mass transfer. Since the volume associated with this process is quite small, the mass transfer during spray impact is very effective in terms of required contactor volume.

6.2. INTERSECTING SPRAYS

In spray columns with more than one nozzle, the sprays may interact with each other, and the liquid from one spray can intercept droplets from adjacent spray nozzles. When these droplets collide, they may coalesce and transfer some of their translational kinetic energy into internal circulation. After coalescence, the droplets may also break up again into two or more droplets. Any or all of these phenomena may affect the mass transfer in the spray.

6.2.1. Experimental methods

Two $\frac{1}{8}$ -A-SS-5 nozzles were used in the laboratory to attempt to measure the significance of spray interception for mass transfer. The nozzles were installed 6.7 cm apart, and the horizontal coordinate x was defined relative to the midpoint between the nozzles as shown in Figure 6.4. The spray from the two nozzles intersected at $x = 0$ and approximately 5.1 cm below the nozzles. For reference, the breakup lengths for the $\frac{1}{8}$ -A-SS-5 nozzles were 3 to 4 cm at 5 to 20 psi. Thus, at the point of intersection, the liquid was in the form of droplets and not sheets.

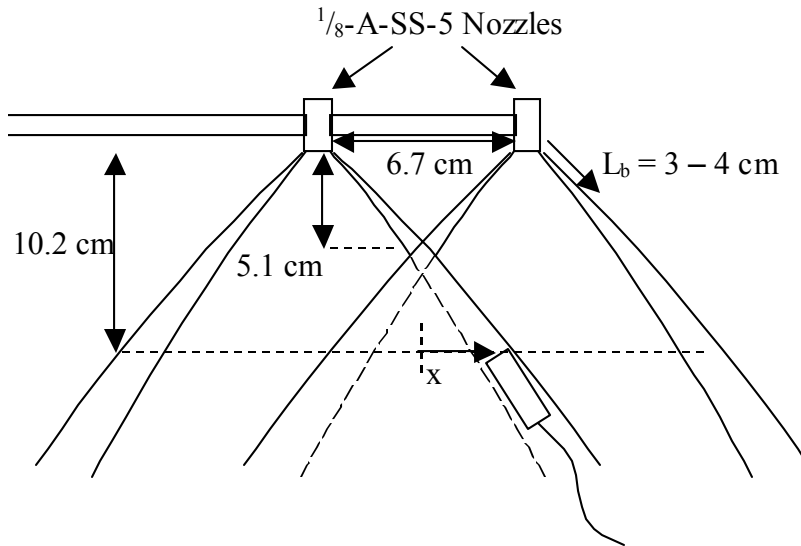


Figure 6.4. Intersecting sprays experimental setup

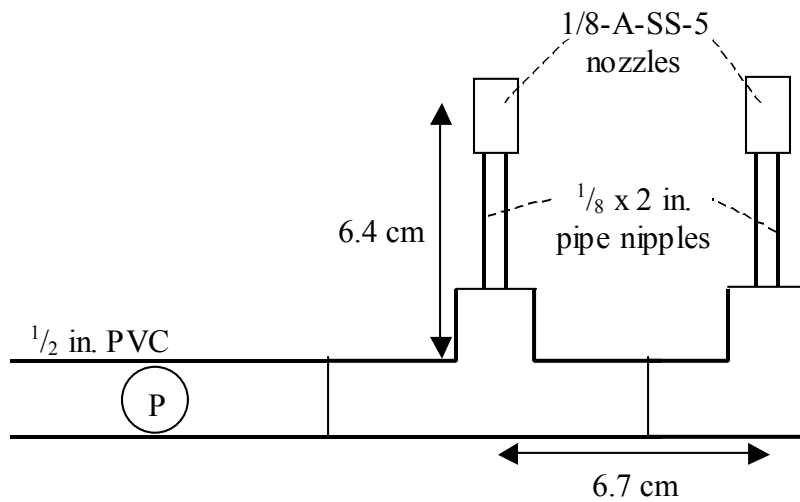


Figure 6.5. Top view of nozzles for intersecting sprays experiment

Before taking mass transfer measurements, the spray distribution was determined by measuring the flow rate through the sampler at various positions inside and outside of the interception zone. The flux profile gives some indication of whether droplet collisions are significant or not. If the flux profile resembles two overlapping hollow cone spray patterns, then the sprays are most likely passing

through one another without much droplet collision. In this case, interaction between the sprays is expected to be minimal. Significant departures from such a flux profile, such as nearly uniform spray flux in the interception zone, would suggest that droplet collisions are important.

The probability of droplet collisions depends in part on the spray flux or the liquid fraction at the point where the sprays cross. Droplets would be more likely to collide with other droplets in a dense spray than in a disperse one. The spray flux was measured at the intersection point ($x = 0$, $y = 5.1$ cm) for nozzle pressures of 5, 10 and 20 psi. The flux at the intersection was 1.5 cm/s at 5 and 10 psi. At 20 psi, the spray flux was 1.9 cm/s.

The flux where the sprays intersect is a function of the nozzle size, operating pressure, and nozzle spacing. Experiments were conducted with $\frac{1}{8}$ -A-SS-5 nozzles because the laboratory apparatus could deliver flow to two of these nozzles at 20 psi. Larger nozzles were not used in this experiment because the maximum nozzle pressure would have been limited to 10 psi or less. The piping system was constructed to obtain the minimum nozzle spacing using the $\frac{1}{2}$ " PVC fittings available.

Flux profiles 10.2 cm below the $\frac{1}{8}$ -A-SS-5 nozzles are given in Figure 6.6. At a nozzle pressure of 5 psi, the peaks in the flux profile are very narrow. As the nozzle pressure is increased to 10 psi, the maximum spray fluxes are about the same, but the peaks become broader. At 20 psi, the peak spray fluxes are slightly higher and the distribution is about the same as at 10 psi.

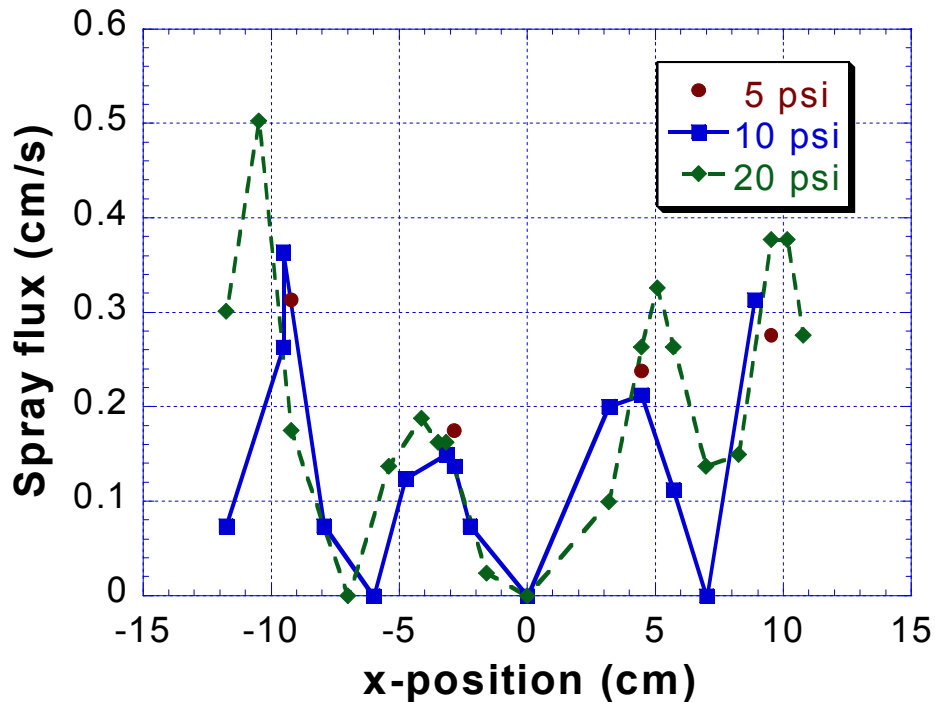


Figure 6.6. Spray flux profile in intersecting sprays experiment (10.2 cm below nozzles)

In the center region ($|x| < 7$ cm), where spray interception might be expected, the peak spray fluxes are consistently lower than the outer positions, where the sprays should be unaffected by each other. In addition, at 10 and 20 psi, the peaks in the flux profile for the interception region seem broader than the outer peaks. However, the spray flux is still zero at $x = 0$. The flux profile indicates that some interaction is occurring but not much.

6.2.2. Results

Samples of the spray were collected 10.2 cm below the nozzles at various horizontal positions. The measured N_L values at these positions are shown in Figure 6.7. The data at $x \approx \pm 7$ cm represent spray at the maximum flux within the interception region. The other data points ($x \approx \pm 12$ cm) refer to samples collected outside of the interception region. The horizontal lines in the graph show the predicted spray N_L values for the 1/8-A-SS-5 nozzle at this spray distance.

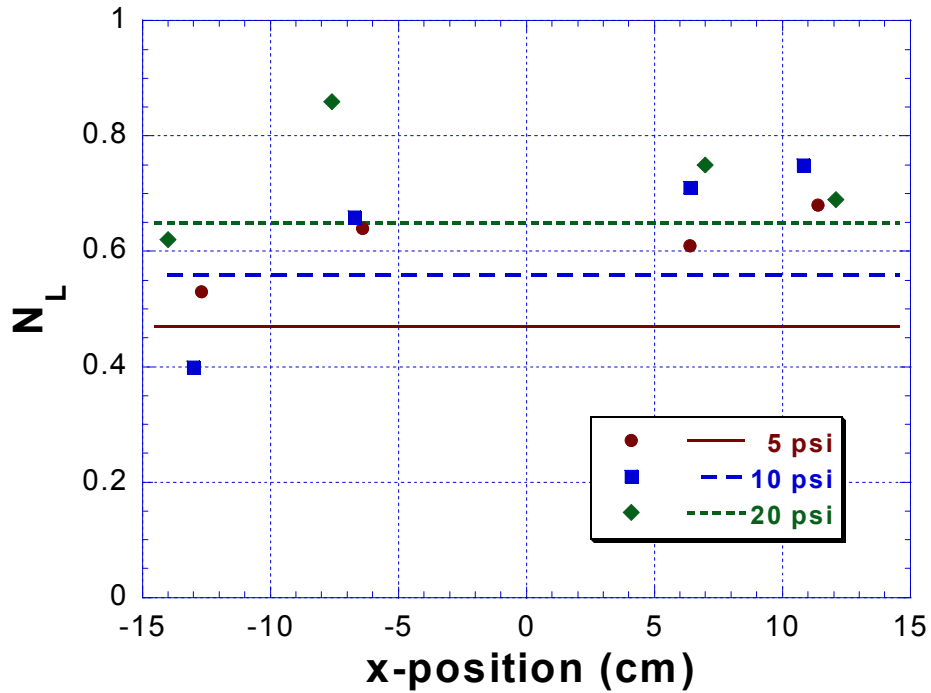


Figure 6.7. Effect of spray interaction on mass transfer

Since the spray at $x \approx \pm 12$ cm was outside of the interception region, these data points should have agreed with the spray N_L correlation. The data inside of the interception region have slightly higher N_L values on average. However, significant scatter exists in the experimental data. To estimate the effect of the spray interaction, the measured N_L values at $x \approx \pm 12$ cm were averaged and subtracted from the values at $x \approx \pm 7$ cm. These differences were attributed to the interaction between the two sprays in the interception region (Figure 6.8).

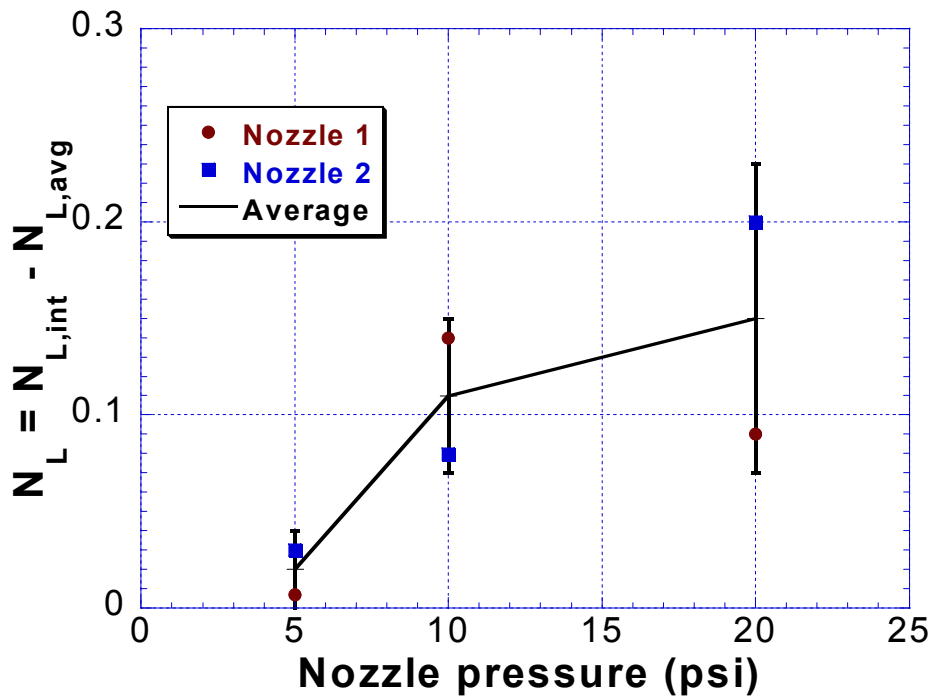


Figure 6.8. Intersecting sprays mass transfer

In Figure 6.8, the data labeled Nozzle 1 refer to samples collected at $x \approx +7$ cm (spray from the first nozzle, positioned at $x = -3.4$ cm), and the Nozzle 2 data were calculated from the data at $x \approx -7$ cm. The error bars show one standard deviation around the average value. The effect of spray interception does not appear to be very significant, and its measurement is subject to relatively large error. The difference between the intercepted spray N_L and the un-intercepted spray N_L was at most 0.15 ± 0.08 .

6.2.3. Comparison with real scrubber conditions

The conditions where spray patterns intersect in a real spray column may be different from those in the model system of the laboratory intersecting spray experiment. The major differences between the large scale and the laboratory systems are the droplet sizes and the liquid flow rates. The liquid flux at the intersection point is considered for comparison.

In the laboratory experiments, the liquid flux at same spray distance as the intersection point was measured to be approximately 1.0 cm/s at 10 psi nozzle pressure. In the pilot scale experiments, liquid fluxes were observed from 2.4 cm/s at spray distance of 0.74 m to 0.2 cm/s at 1.8 m. These fluxes were correlated with the distance and nozzle pressure as follows.

$$\text{flux(cm/s)} = 0.53P^{0.46}r^{-1.8} \quad (6.2)$$

If 120° spray nozzles are placed two feet apart in a large-scale scrubber, the sprays are expected to cross at spray distance of 0.35 m. If Equation 6.2 is extrapolated to 0.35 m, the expected flux at 10 psi is 10 cm/s. Since the expected flux with the 3-inch nozzle in a large-scale scrubber is so much higher, a great deal more spray interaction could occur.

Although the laboratory measurements of interception mass transfer were only about 0.1 transfer units, the results may not be directly applied to large scale systems because of the disparity in spray flux at the interception point.

6.3. WALL EFFECTS

Wall effects, or more generally spray impact on solid surfaces, are expected to be common in spray columns, but the magnitude of mass transfer during these events is unknown. Many opportunities exist for spray to hit solid surfaces such as the column walls, spray nozzles, piping for adjacent spray headers, other types of column internals, etc. When spray strikes these surfaces, the droplets may shatter and generate additional mass transfer area. Most likely, the liquid also forms thin films on the solid surfaces, and impact events agitate the liquid film and provide higher mass transfer coefficients.

6.3.1. Experimental methods

As a model system for spray impact on solid surfaces, an experiment to measure mass transfer wall effects was designed (Figure 6.9). A flat, stainless steel plate was suspended vertically from the sample arm. The metal plate was positioned

so that most of the spray hitting the plate would run down the wall instead of deflecting off the surface. The quench sampler was centered at the bottom edge of the plate to catch the liquid running down the wall without contributing additional mass transfer.

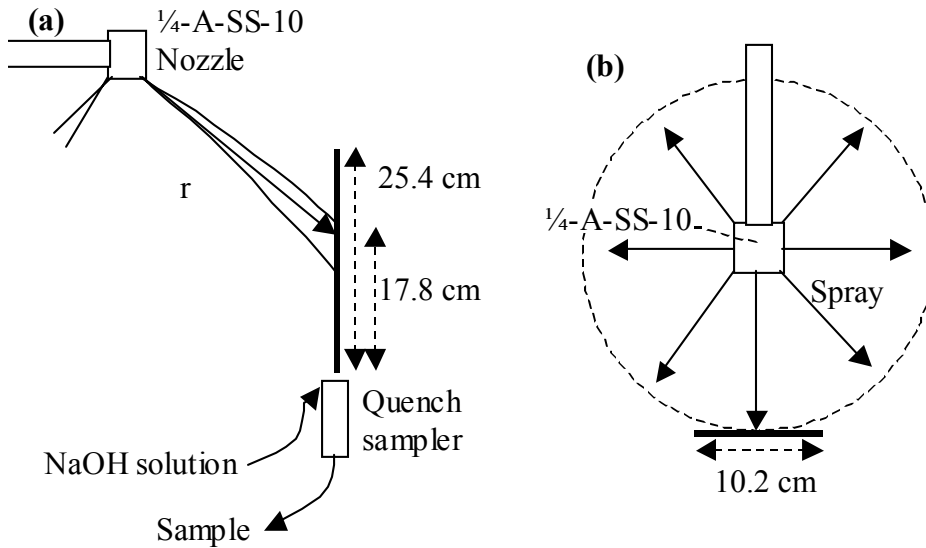


Figure 6.9. Wall effect experimental setup (a) side view (b) top view

The plate was 10.2 cm wide and 25.4 cm in height. For each spray distance, the plate was positioned so that the bulk of the spray hit the plate approximately 7.6 cm from the top. Thus, the length of the wetted wall section has held constant at 17.8 cm.

As with the pool mass transfer experiments, the $\frac{1}{4}$ -A-10 nozzle was used and the mass transfer including the spray impact effect was measured at various distances and nozzle pressures. The observed N_L was compared with the predicted values of the empirical spray correlation to determine the contribution of the spray impact mass transfer. However, the wall effect experiments require another correction for the mass transfer to the wetted wall section.

The sample flow rate was measured using the quench sampler so the flow per unit width (Q/w) and the Reynolds number of the wetted wall could be calculated.

$$\text{Re}_w = \frac{4\rho Q}{\mu w} \quad (6.3)$$

The values of Re_w in the experiments were between 100 and 500. These values for Re_w and the unsteady nature of the spray impact suggest that the wetted wall is in a rippling flow regime (Fair et al., 1984). Therefore, mass transfer coefficient for the wetted wall was calculated using the model of Vivian and Peaceman (1956).

$$\frac{k_L L_w}{D} = 0.433 \text{Re}_w^{0.4} \text{Sc}^{1/2} \left(\frac{\rho^2 g L_w^3}{\mu^2} \right)^{1/6} \quad (6.4)$$

The liquid collected in the quench sampler was exposed to an area of wL_w , where the length of the wetted wall (L_w) was 17.8 cm and the width (w) was the diameter of the sampler or 1.9 cm. Thus, the interfacial area was 33.9 cm². The contribution of the wetted wall to the total N_L was calculated by

$$N_{L,ww} = \frac{k_L A}{Q} = \frac{k_L h w}{Q} \quad (6.5)$$

Finally, the mass transfer due to spray impact on the wall can be calculated.

$$N_{L,imp} = N_{L,meas} - N_{L,spray} - N_{L,ww} \quad (6.6)$$

6.3.2. Results

The N_L measurements in the wall effect experiments are shown in Figure 6.10. The predicted spray N_L values were subtracted from the observed values to obtain the N_L due to the wall effects. The experimental values are shown in the figure as solid data points. The open data points represent N_L values predicted using the wetted wall model of Vivian and Peaceman (1956).

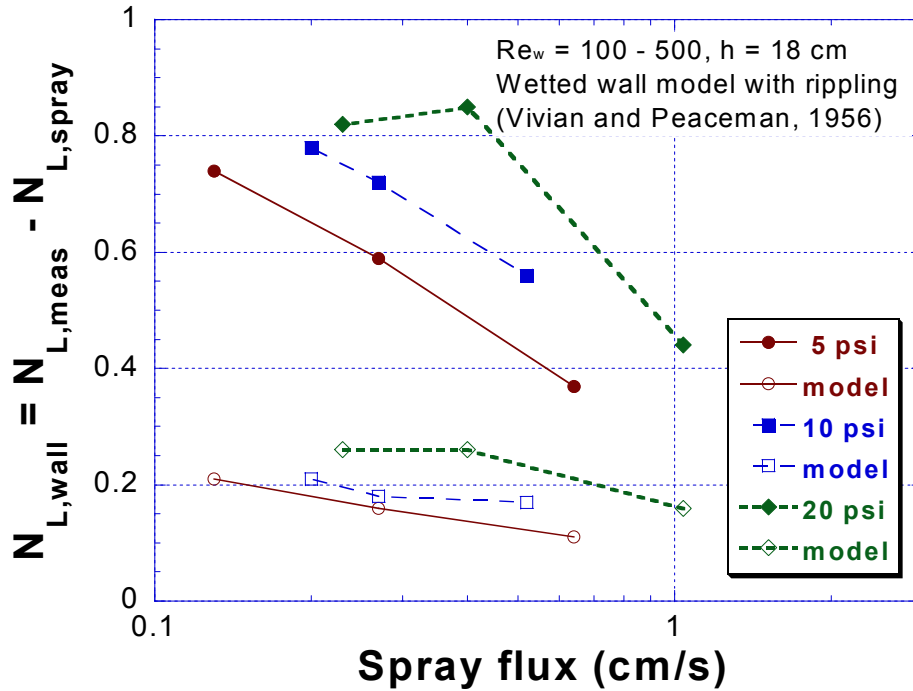


Figure 6.10. Comparison of wall effect with wetted wall model

The experimental data have much higher N_L values than predicted using the spray N_L correlation. The mass transfer due to the presence of the “wall” ranged from 0.4 transfer units at the higher fluxes (closer to the nozzle) to 0.8 transfer units at the lower fluxes. This wall effect mass transfer was also much greater than expected for wetted wall mass transfer, for which the N_L was calculated to be about 0.2. The additional mass transfer is due to the spray impact on the wall.

6.3.3. Interpretation

The observed mass transfer was interpreted as the sum of the N_L due to the spray, the impact, and the wetted wall. The spray N_L and the wetted wall N_L were calculated and subtracted from the measured values to obtain the mass transfer during spray impact on the wall ($N_{L,imp}$). $N_{L,imp}$ was significant in the laboratory experiments, and 0.2 to 0.6 transfer units may be attributed to the spray impact (Figure 6.11). Since the spray mass transfer for the ¼-A-SS-10 nozzle accounted for

about 0.5 to 0.7 transfer units, the wall impact may nearly double the N_L of the contactor over that of the spray itself.

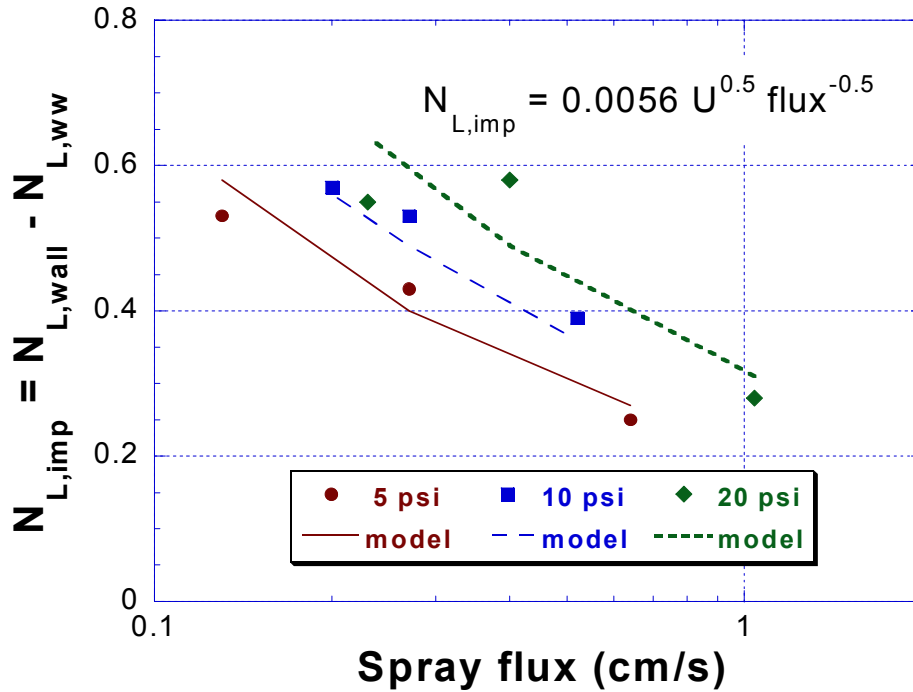


Figure 6.11. Wall impact mass transfer (model curves from Equation 6.7)

$N_{L,imp}$ was also correlated as a function of liquid flux at the point of impact and the spray velocity.

$$N_{L,imp} = 0.0056 U_o^{0.5} (\text{flux})^{-0.5} \quad (6.7)$$

In Equation 6.7, both U_o and flux have units of cm/s. Measurements of the liquid flux in a previous experiment with the 1/4-A-SS-10 nozzle were used to correlate the flux with pressure and distance. The wall impact N_L varies with both the spray velocity and the flux, approximately to the 0.5 power. Values for $N_{L,imp}$ are graphed in Figure 6.11 as a function of spray flux and nozzle pressure. The predictions of Equation 6.7 are shown as curves in Figure 6.11.

A comparison of Figure 6.3 and Figure 6.11 shows that the effects of spray impact on walls and into liquids were similar in magnitude. Both types of impact led

to N_L values of about 0.2 to 0.7. In addition, the correlations for the impact N_L had similar dependences on velocity and flux, as shown in Table 6.1.

Table 6.1. Comparison of pool and wall impact N_L correlations

Coefficient*	Pool impact (Equation 6.1)	Wall impact (Equation 6.7)
ln A	-5.94 ± 1.38	-5.18 ± 1.11
B	0.72 ± 0.19	0.55 ± 0.15
C	-0.17 ± 0.04	-0.47 ± 0.07

* As defined by $N_L = AU_o^B(\text{flux})^C$

The variation of the impact N_L with the spray velocity was about the same for the pool and the wall impact correlations. On the other hand, the flux dependence was slightly different for the two types of impact. The difference may be because the pool impact also includes the effects of gas entrainment. As the flux increases, more gas is entrained into the liquid pool and more interfacial area will be available for mass transfer. Thus, the flux dependence is greater for the pool impact than for the wall impact. However, the negative exponent on flux for the pool N_L indicates that the higher mass transfer rates are still not enough to offset the increased liquid flow rate.

6.4. APPLICATION TO PUBLISHED DATA

Previous researchers have reported data for mass transfer in spray columns, but they neglected wall effects and the mass transfer during spray impact. The literature data are summarized in Section 2.3. In each experiment, the N_L of the spray column was measured, and all of the mass transfer was assumed to be occurring in the spray. In fact, much of the mass transfer observed in these systems was probably due to spray impact on the column walls or pools of liquid.

Pigford and Pyle (1951) performed experiments with full cone spray nozzles and separated the liquid flowing down the walls from the spray collected in the

middle of the bottom of the column. The reported N_L values were calculated from the spray samples. However, it is unclear whether liquid was allowed to accumulate in the collection basin at the bottom of the column. If a significant liquid level existed there, then the mass transfer during impact into that liquid would resemble mass transfer discussed in Section 6.1. If liquid did not accumulate in the basin, then the mass transfer would be more like that described in Section 6.3.

With the column dimensions, nozzle pressures, and liquid flow rates reported by Pigford and Pyle, the N_L for spray impact can be calculated. The velocity of spray is calculated from the nozzle pressure by Equation 3.22. The spray flux can be estimated if the liquid is assumed well distributed in the full cone spray pattern, which had a spray angle reported as approximately 60° . Then the N_L may be calculated for spray impact into a pool by Equation 6.1 and for spray impact onto a solid surface by Equation 6.7. The predicted N_L values for spray impact are compared with the reported data in Table 6.2.

Table 6.2. Comparison of published data with predicted N_L for spray impact

	ΔP (psi)	Reported N_L values	Impact N_L at collection		N_L for wall impact ²
			Pool ¹	No pool ²	
Pigford and Pyle, 1951	3	1.8*	0.5	1.1	
	30	3.4*	1.1	1.5	
Mehta and Sharma, 1970	4	0.9	0.6	1.4	0.9
	16	1.6	0.9	1.4	0.9

¹Calculated from Equation 6.1

²Calculated from Equation 6.7

*Average of reported values with 6 spray nozzles and $z = 1.32$ m

The predicted N_L for spray impact is a significant fraction of the total N_L for the spray contactor. If a liquid level was present in the bottom of the column, then a comparison of the pool N_L with the reported values shows that spray impact may represent 30% of the total mass transfer. If the bottom of the column did not contain

accumulated liquid, then the spray impact may contribute 60% of the total at a nozzle pressure of 3 psi and 44% at 30 psi.

Mehta and Sharma (1970) did not separate the wall flow from the spray. Although full cone nozzles were used, the tall (1.23 m) and relatively narrow (0.21 m) column meant that most of the spray was probably impacting and flowing down the walls. Assuming a spray angle of 60° and a good distribution over the full cone spray pattern, the velocity and flux can be calculated as described above. The N_L is calculated from Equation 6.1 and/or Equation 6.7 for impact at the bottom of the column.

However, since most of the spray was hitting the walls, the N_L for wall impact may be more relevant. Since the velocity was assumed constant, it is the same as in the previous calculations. For an estimate of the average flux, the wall flow rate was calculated assuming a 60° spray angle and no splashing of liquid from the wall back into the spray. The flux was then calculated by dividing the wall flow by the wall area. Thus, the estimated N_L values for wall impact were 0.9 transfer units. At a nozzle pressure of 4 psi, the N_L of the column could be entirely due to wall effects. Even at a nozzle pressure of 16 psi, the estimated N_L for wall impact is 56% of the overall N_L .

Jarvis and Burke (1988) discussed some experiments in which limestone was sprayed onto dual flow trays. The SO_2 removal (expressed as $\ln(y_{in}/y_{out})$) was measured with no trays, one tray, and two trays in service. The removal increased only slightly as more trays were added. Jarvis and Burke explained the difference in performance for the two trays using chemistry and limestone grind considerations. However, the higher mass transfer on the first tray could also have been the result of spray impact onto the tray. The liquid falling from the first tray to the second would have had relatively little energy, and the effect of spray impact would have been much less for the second tray.

Most of the papers discussed in Section 2.3 did not report enough information to estimate the N_L for spray impact effects. For example, the flux could not be calculated for the experiments with a hollow cone spray nozzle (Simpson and Lynn, 1977) or a flat spray nozzle (Lin et al., 1977). However, Lin et al. did note that the column diameter was large enough so that spray would not contact it before reaching the bottom of the column. In addition, liquid was not allowed to accumulate in the bottom of the column. Thus, wall effects should be negligible and Equation 6.7 should be appropriate to describe the impact N_L at the bottom of the column. Their correlation (Equation 2.8) implies that the N_L varies with $U^{0.4}$ and linearly with z . Although the flux cannot be calculated, it is expected to vary approximately with z^{-2} . According to Equation 6.7, the N_L for impact has a 0.5 dependence on velocity and a -0.5 dependence on flux, both of which are very close to the exponents derived from Equation 2.8. Therefore, most of the published data for mass transfer in sprays may be explained using the current results for mass transfer during spray impact.

6.5. SUMMARY

Experiments were conducted to measure the mass transfer during various forms of spray impact to determine whether these phenomena are the reason for the discrepancy between spray N_L measurements and the expected values for a spray column. The impact of spray droplets onto solid and liquid surfaces was found to be significant and provided as much N_L as the spray region alone. Although the experiments were conducted with hollow cone nozzles, the results for mass transfer during spray impact should be applicable to full cones and other types of spray nozzles. Thus, a large fraction of the liquid phase mass transfer in a real spray column is expected to occur when the spray droplets strike the walls, piping, or liquid surfaces in the contactor.

The impact N_L increased with the spray velocity to the 0.5 to 0.7 power. The higher kinetic energy of the droplets would be expected to increase the impact phenomena (droplet breakup, gas entrainment, surface renewal, etc.). The impact N_L

had a -0.2 dependence on spray flux for spray impact into liquid pools and a -0.5 dependence on flux for wall impact. Since the spray flux is proportional to the flow rate if velocity is held constant, the fact that the N_L dependence is greater than -1.0 indicates that the mass transfer is increasing but not as quickly as the flow rate.

Mass transfer during spray interception of other spray was not demonstrated to be significant in the laboratory experiments. However, the spray flux at the intersection point was lower in the laboratory experiments than it would be in a commercial spray scrubber. The higher flux in a large-scale spray column may result in more droplet collisions and additional mass transfer. Future researchers will most likely need to measure mass transfer during spray interception with large-scale nozzles to accurately reproduce the conditions in a real contactor.

More efficient contactor designs could take advantage of mass transfer during spray impact. For example, the nozzles could be packed closely together to limit the spray droplet region, which has relatively low mass transfer efficiency per unit contactor volume. The spray could then be intercepted with solid targets such as baffles, screens, or coarse packing elements. The impact events require very little contactor volume so high N_L values may be attainable in spray/impact contactors much smaller than current spray column designs.

Chapter 7: Conclusions

The mass transfer during sample collection from high velocity gas-liquid streams can be significant. A quench sampling method was developed, which effectively eliminates mass transfer during sample collection. This new sampling method provides more accurate mass transfer measurements so that the mass transfer in the spray and during impact on surfaces could be separated.

7.1. SPRAY MASS TRANSFER AS A FUNCTION OF DISTANCE

Most of the mass transfer in the spray occurs in the sheet as the liquid exits the spray nozzle. The centrifugal hollow cone nozzles provided 0.4 liquid transfer units within 10 orifice diameters from the nozzle. Once the mass transfer in the spray was isolated, much of the spray N_L was found to occur in the liquid sheet emanating from the spray nozzle, even before the sheet breaks into droplets. For the nozzles in this study, the N_L at the point of sheet breakup was approximately 60% of the total N_L achieved in the spray. The high mass transfer rates in the sheet are the result of turbulent mass transfer and high interfacial area, which compensate for the extremely short contact time of the sheet.

From 10 to 60 orifice diameters, the N_L of the spray increases by only about 0.25 or 0.005 transfer units per orifice diameter. The droplets ($d_{v0.5} = 500-1600$) were expected to be oscillating because of the breakup phenomena and the Reynolds number for the flow around the droplet. The slope of the N_L curve was low in the droplet region primarily because of the high droplet velocities and thus the short contact times. The mass transfer rate in the droplet region was consistent with an oscillating droplet k_L but slightly lower than the oscillation k_L model would predict.

7.2. SPRAY IMPACT

A great deal of mass transfer occurs during spray impact or sample collection. The data obtained during the development of the overflow sampler demonstrated that

sample collection accounted for 0.2 to 0.7 mass transfer units. In separate experiments, mass transfer during spray impact on liquids, walls, and other sprays were studied. The mass transfer that occurred when spray droplets collided with walls or liquid pools accounted for 0.2 to 0.8 transfer units as well. The mass transfer during impact increased with increasing spray velocity and decreased with increasing liquid flux. In addition, mass transfer during impact is expected to be significant for any high velocity spray, whether a hollow cone, full cone, or any other type of spray nozzle is used.

Thus, mass transfer during spray impact was comparable to the spray N_L measured with the quench sampler. Consequently, much of the previous literature for spray columns may overestimate the spray N_L because of wall effects or sample collection issues. As little as half of the total mass transfer may be due to the spray. The remainder of the mass transfer may be occurring at the walls, at spray impact on column internals, or at the liquid surface in the bottom of the spray tower.

The significance of liquid sheets and spray impact for liquid phase mass transfer may also lead to innovative gas-liquid contactor designs. Spray column designs can take advantage of the exceptionally high N_L per unit contactor volume for the sheet and impact phenomena by limiting the amount of contactor volume occupied by the droplets. Impact surfaces could be positioned immediately below the spray nozzles so that as soon as the sheet breaks into droplets, the high velocity droplets impact the surfaces. The liquid could be collected and recycled to the reaction tank or fed to the next spray header.

7.3. NOZZLE PRESSURE DROP

The nozzle pressure drop has little effect on the number of liquid phase transfer units in the spray. Higher nozzle pressures led to higher velocities in the sheet and for the spray droplets. In the sheet, the mass transfer coefficient increased, but the sheet length decreased. Therefore, both the interfacial area and the contact time of the sheet decreased. In the droplet region, the higher pressure resulted in

smaller droplets, which have higher oscillation k_L values and area per unit liquid volume. However, the higher velocities led to shorter contact times for the droplets. These tradeoffs between k_L , a , and t were nearly balanced so that the overall effect of nozzle pressure on the spray N_L was only weakly positive.

The major effect of increasing the nozzle pressure is the greater mass transfer during spray impact. The higher velocities caused more violent spray impact, and more of this energy likely generated additional surface renewal and/or interfacial area.

7.4. NOZZLE SIZE

The N_L of the spray decreases approximately with the orifice diameter as the nozzle size is increased. Spray distance was found to scale roughly with the orifice diameter over the narrow range of laboratory nozzle sizes. The pilot scale N_L data were lower, indicating that the orifice diameter had a slightly stronger effect.

7.5. HIGHLY VARIABLE k_L

The k_L values vary greatly in the different parts of the spray contactor. High k_L values were observed in the sheets emanating from the spray nozzles, and high mass transfer rates ($k_L a$) were observed for spray impact on liquid pools and solid surfaces. However, the mass transfer coefficients for the droplets were significantly lower. Because the k_L values varied widely, the relative mass transfer resistances of the gas and liquid phases are also expected to vary. Unlike the CO_2 -air-water system, mass transfer in the SO_2 -air-water system tends to have significant resistances in both the gas and liquid phases. The mass transfer may become gas film controlled when the k_L is high (in the sheets or at spray impact), and then liquid film controlled in the spray droplets. A single value for the k_L^o/k_g ratio may not be sufficient to describe these systems so the modeling and/or design of spray contactors may require a distribution of k_L^o/k_g ratios.

For example, the model of DeVincentis (1998) could be extended based on the results of this work. Each spray level would be divided into at least three pieces: the sheet, droplet, and impact regions. Both the sheet and the impact regions would have very high k_L compared to the droplet region. The gas phase mass transfer coefficient could be assumed constant, and different values for the ratio of k_L^o/k_g would be used in the simulation of each region. Alternatively, the k_L^o/k_g ratio could be held constant, and the N_g value for the spray level would be distributed among the sheet, droplet, and impact regions. Since no data for k_g as a function of position in the spray scrubber is available, simulations could be performed with either of these assumptions, and the results compared.

Chapter 8: Recommendations

8.1. GAS PHASE MASS TRANSFER

The focus of this work was the liquid phase mass transfer in spray contactors. For chemical systems other than CO₂-air-water, the gas phase mass transfer may be significant or dominating. In the case of SO₂-air-water, the mass transfer resistances in both the gas and liquid phases may be important. In traditional analyses, the k_g , k_L , and specific interfacial area of the contactor are assumed constant. Then, chemical reactions may be included to calculate the overall mass transfer rates.

However, in this work, the liquid phase mass transfer was found to vary widely in different parts of the contactor. Now that the liquid phase mass transfer is better understood, the next logical step is to improve the understanding of the gas side. For the SO₂ system, the high k_L values for the sheet and/or spray impact regions may lead to gas phase control of the mass transfer in these parts of the column. If the mass transfer rate is not completely liquid phase controlled in all of the contactor, then an accurate calculation of the mass transfer rate would require knowledge of k_g as a function of position in the spray tower.

8.2. GAS DISTRIBUTION

In a large commercial scrubber, gas distribution can also be an issue. If the mass transfer rates in both the gas and liquid phases are high, the removal of SO₂ may become limited by the rate at which SO₂ is transferred from the bulk gas stream. This gas distribution issue is similar to gas phase mass transfer but occurs over greater length scales, such as mixing. Recent scrubber designs have attempted to reduce bypassing of the gas around the spray nozzles or along the walls. Otherwise, poor gas distribution would allow some of the gas to pass through the scrubber without ever really contacting spray.

Since the liquid phase mass transfer rates were found to be very high in the nozzle sheets and during spray impact, these areas may be susceptible to gas

distribution limitations. The mixing of the gas phase should be studied in detail along with the gas phase mass transfer to determine the limiting mechanisms in the different parts of the spray contactor. If the gas and liquid phase mass transfer coefficients can be determined, then computational fluid dynamic simulations should be able to incorporate the effects of gas distribution.

8.3. SPRAY IMPACT

The primary focus of the work performed on mass transfer during spray impact was to determine its significance in a real spray tower. Now that the magnitude of the impact N_L has been found to be as high as the spray N_L in many cases, a more detailed study of mass transfer in spray impact phenomena is warranted.

In the pool and wall impact experiments, the velocity and flux of spray were varied because they were expected to have the greatest effect. However, the nozzle size or droplet size should also be varied to determine their effect on the mass transfer during these types of spray impact. These experiments could also be extended to include sheets impacting on walls and/or liquid pools.

Studies of mass transfer during wall impact could also expand to cover other solid surfaces such as pipes, mesh, structured packing, etc. The experiments in this work were limited to spray impact at a fixed angle on a flat plate of fixed length. The accuracy of the measurements for wall impact N_L could be marginally improved by varying the length of the wetted wall to verify that the wetted wall is well described by the model for rippling wall flow. The angle of impact is a more interesting parameter, which should be investigated. At some angle, the maximum amount of kinetic energy should be converted into surface renewal (k_L) or additional interfacial area. Sample collection might be more difficult for other impact angles, but the results would be interesting nonetheless and could indicate the effect of spray impact on pipes, which should be very common in a real scrubber.

The pool experiments could also be modified to use different diameter pool samplers. It is possible that liquid near the edge of the pool sampler is less free to experience turbulent surface renewal than the liquid at the center of the sampler. Varying the sampler diameter would be a convenient way of measuring whether this effect is significant. Even if the sampler size is an issue, the N_L of the pool would be expected to increase with the pool diameter, and the results of this work would be conservative estimates of the N_L for spray impact into liquid pools.

8.4. SPRAY INTERFERENCE IN PILOT SCALE SYSTEM

Although no significant mass transfer was measured due to spray interception, the higher fluxes in a commercial scrubber may result in more interaction between the sprays. To gain more understanding of mass transfer and complex spray behavior in real spray towers, intersecting spray experiments should be conducted at the large scale. The pilot scale apparatus constructed as part of this work would have to be completely redesigned to accommodate two large scale nozzles and allow for sample collection at relevant distances from both nozzles. Alternatively, the quench sampler could be reproduced with sturdier materials and measurements taken in a pilot or full scale scrubber.

The understanding of mass transfer in all of the types of spray impact (wall, pool, and spray) would benefit from the development of theoretical framework for energy dissipation as a source of turbulent surface renewal and/or additional interfacial area.

8.5. CONTACTOR INNOVATIONS

In light of the high mass transfer rates next to the spray nozzle and at spray impact on surfaces, more efficient gas-liquid contactors may be designed. Both the sheet and the spray impact require minimal contactor volume. On the other hand, the spray droplets tend to occupy a large portion of the contactor volume but have relatively slow mass transfer rates. For separations with significant liquid phase

resistance, the size of the contactor could be greatly reduced by limiting the fraction of the column occupied by droplets.

In a spray tower, the nozzles should be packed closely together to take advantage of the efficient mass transfer in the sheet before droplet formation. Further innovations could also incorporate mass transfer during spray impact into the design. Surfaces placed in the path of the spray would serve as targets for spray impact. If these targets were positioned near the sheet breakup point, then as soon as the droplets are formed they strike the targets and generate additional mass transfer. Afterwards, the liquid could be collected and recycled to the reaction tank or fed to the next spray header.

A variety of materials should be used as the impact surfaces to validate and optimize the contactor design. Flat plates have the advantage of simplicity and of low cost. Mesh or some type of coarse column internals may provide additional interfacial area and be more effective, but the cost may be significantly higher. The coarse geometry would have open area for gas flow so that the low pressure drop of the spray contactor would not be sacrificed. Structured packing with high void fraction and low pressure drop would be attractive. Trays with a large ratio of hole area to active area could also be tested. Experiments with such contactor designs should be performed to measure the mass transfer efficiency, which should be much higher for the liquid phase.

Appendix A Nozzle data

Table A.1. Data for Spraying Systems nozzles

Nozzle		1/8-A-SS-0.5	1/8-A-SS-2	1/8-A-SS-5	1/4-A-SS-10	3/8-A-SS-20	3CF-SILCNB-120
Orifice (in)		0.047	0.078	0.125	0.172	0.250	2.063
Capacity ¹ (gpm at given psi)	3			0.27	0.55	1.1	78
	5		0.14	0.35	0.71	1.4	102
	7						120
	10	0.05	0.20	0.50	1.0	2.0	143
	15	0.06	0.25	0.61	1.2	2.4	
	20	0.07	0.28	0.70	1.4	2.8	203
	30	0.09	0.35	0.86	1.7	3.5	249
Angle ¹ (° at given psi)	7		52	56	63	63	71
	20	58	61	67	70	70	73
	60						77
	80	69	69	76	74	74	
d _{v0.5} ^{2,3} (µm)	7						1710
	10	365	435	500	645	910	
	12	360	420	495	640	900	
	15	355	410	485	625	880	1300
	17	345	400	475	620	870	
	20	340	395	470	605	860	1200
	25	320	380	460	590	830	

¹Capacity and spray angle data from Spraying Systems catalog 60.

²Droplet size data for laboratory nozzles from Spraying Systems datasheet 11825-9.

³Droplet size data for 3CF nozzle provided by Spraying Systems (Jett, 1999)

Table A.2. Correlation of spray flow rate

$Q = C_0 d_{or}^{C_1} \Delta P^{C_2}$	
Parameter	Regressed value
ln C0	2.35 ± 0.02
C1	2.011 ± 0.004
C2	0.501 ± 0.006

Note: d_{or} in inches and ΔP in psi

Table A.3. Sauter mean and volume median droplet diameters (Koehn, 2001)

d_{32} (μm)	$d_{V0.5}$ (μm)
100	137
300	405
1000	1400
3000	4100
7000	9900

Appendix B Oscillation criteria

Klee and Treybal, 1956

$$d_{pc} = 0.33\rho_c^{-0.14}\Delta\rho^{-0.43}\mu_c^{0.30}\sigma^{0.24}$$

Hu and Kintner, 1955

$$We = \frac{dU^2\rho_c}{\sigma} > 3.58$$

Johnson and Braida, 1957

$$\frac{Re}{P^{0.15}} = Re\left(\frac{\sigma^3\rho_c^2}{g\mu_c^4\Delta\rho}\right)^{-0.15} > 20$$

Edge and Grant, 1971

$$d_{pc} = 0.162\left(\frac{\rho_d}{\Delta\rho}\right)^{0.5}$$

Grace et al., 1976

$$H = \frac{4}{3}EoP^{0.149}\left(\frac{\mu_c}{\mu_w}\right)^{-0.14} > 59.3$$

$$Eo = \frac{g\Delta\rho d^2}{\sigma}$$

Schroeder and Kintner, 1965; Skelland et al., 1987

$$Re = \frac{dU\rho_c}{\mu_c} > 200$$

Appendix C Calculating k_L and a

Assumptions

1. Steady state
2. Dilute solution (i.e. liquid phase mole fraction of $\text{CO}_2 \ll 1$)
3. Mass transfer is liquid film controlled
4. Negligible concentration of CO_2 in the gas phase.

Material balance on differential section of spray

$$-Q_L dC = k_L (C - 0) dA_i$$

$$dA_i = a A_{cs} dz$$

Define liquid phase transfer unit

$$dN_L \equiv -\frac{dC}{C} = \frac{k_L a}{Q_L} A_{cs} dz = \frac{k_L a}{U'} dz$$

Usually, as in the case of a packed column, an average value of k_L would be assumed, and the above equation would be integrated over a section of the column from the nozzle to position z .

$$N_{L,z} = - \int_{C_{inlet}}^{C_z} \frac{dC}{C} = \int_0^z \frac{k_L a}{U'} dz$$

$$= \ln \left(\frac{C_{inlet}}{C_z} \right) = \frac{k_{L,avg} a}{U'} (z - 0)$$

If the drop velocities are known, then the holdup and the area to volume ratio may be calculated (Seibert and Fair, 1993).

$$\phi \approx \frac{U'}{u \exp(-1.92\phi)}$$

$$a = \left(\frac{6\phi}{d_{vs}} \right)$$

However, the spray will not have a constant superficial velocity or holdup. Since the nozzle will produce a conical spray, U' and ϕ will decrease with distance from the nozzle. Far from the nozzle, the drops decelerate to their terminal velocities and the spray becomes less conical. This region has more constant values for U' and ϕ , and the above procedure may be used to calculate k_L . Unfortunately, for the large nozzles of interest, the conical region of the spray is several feet in diameter, and the standard

method of extracting k_L from N_L data will not be applicable to the spray in the experimental column.

A more appropriate method to calculate k_L in sprays may be to develop a model for k_L that will match the experimental N_L data. For example, if the drops do not undergo significant secondary breakup or coalescence, the concentrations in individual drops may be calculated independently.

$$V_d dC = -k_L A_d C dt$$

$$\frac{dC}{C} = -k_L \left(\frac{6}{d_e} \right) dt$$

The concentration of a droplet is purely a function of the droplet's contact time. The contact time of a droplet at a given position in the spray can be estimated from the droplet initial velocity, gravitational acceleration, and drag. There may be a distribution of contact times because the drag will be different on the different droplet sizes. Thus, the contact time could be a function of droplet diameter and distance from the nozzle.

Then, the concentration in a droplet of size d_i is a function of d_i and distance from the nozzle.

$$C_i(z) = C_o \exp \left[-\frac{6k_L}{d_{e,i}} t(d_{e,i}, z) \right]$$

The concentrations of these individual droplets may be averaged over the drop size distribution to obtain a model for the bulk average concentration as a function of position, which can then be compared with the experimental observations.

$$\bar{C}(z) = \frac{\sum n_i C_i d_i^3}{\sum n_i d_i^3}$$

The important data requirements of this model are the drop size distribution, a model or measurements for velocities/contact times, and model for k_L . The drop size distribution and the velocities are expected to be functions of the nozzle pressure drop, nozzle type, and physical properties of the system. The liquid mass transfer coefficient is expected to be a function of drop size, nozzle pressure drop, and various physical properties.

The model could be simplified by assuming an average droplet diameter, such as the Sauter mean (d_{32}). In addition, the contact time of the droplets may not be such a strong function of the droplet size since the droplets are not independent. The motion

of the other spray droplets can affect the drag forces so that the standard correlations for a single sphere in an infinite medium may not be applicable. Since the contact time of the droplet is often very short, the effect of drag may even be negligible.

The model for k_L could be based on the assumption of droplets with damped oscillations. The drops are non-spherical after formation. Surface tension deforms the drops toward a spherical shape, but inertia can cause oscillations. By considering these forces, one can calculate a natural drop oscillation frequency. However, the viscosity of the liquid phase would tend to damp out these oscillations (Lamb, 1945). Then, based on the Angelo oscillation model, the form of a damped oscillation model might be

$$k_{L,i} = \sqrt{\frac{D}{\pi t_p}} \left[\varepsilon_0 + \varepsilon_1 \exp\left(-\frac{t_i}{\tau}\right) \right]$$

$$\text{where } t_p = \frac{\pi}{4} \sqrt{\frac{\rho d_i^3}{\sigma}}, \quad \tau = \frac{\rho d_i^2}{20\mu}$$

The contact time t_i is expected to be a function of the drop size, pressure drop and distance from the nozzle. The parameters (ε_0 and ε_1) might also depend on the pressure drop. However, in the Angelo model, the effect of the oscillation amplitude is relatively weak and may not be observable.

Appendix D Pilot scale apparatus

PROCESS FLOW DIAGRAMS

Pilot scale experiments were conducted at the Separations Research Program facility on the Pickle Research Campus of The University of Texas at Austin.



Figure D.1. Pilot facility of the UT Separations Research Program

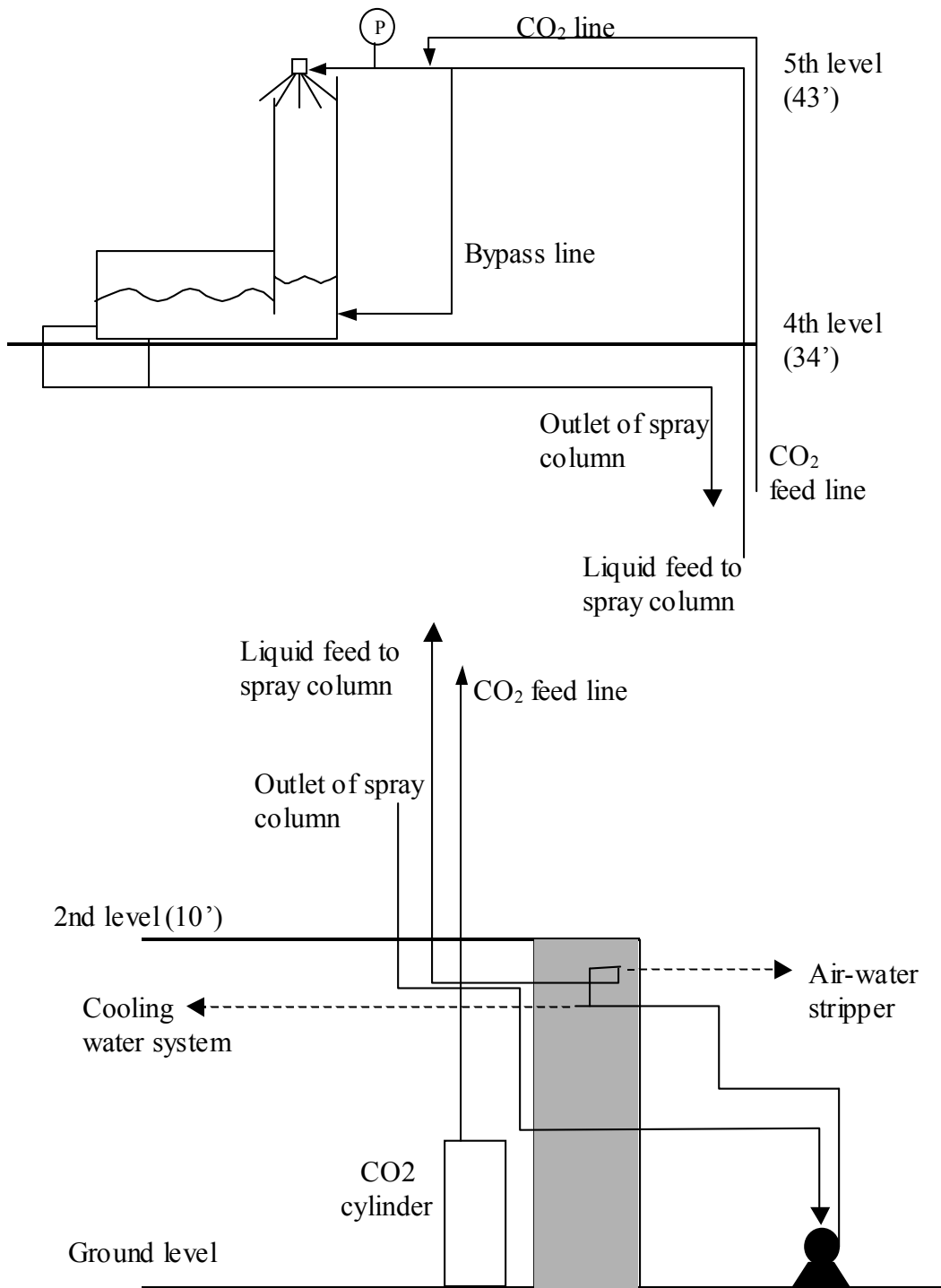


Figure D.2. Diagram of piping for the pilot spray column

SPRAY COLUMN DIMENSIONS

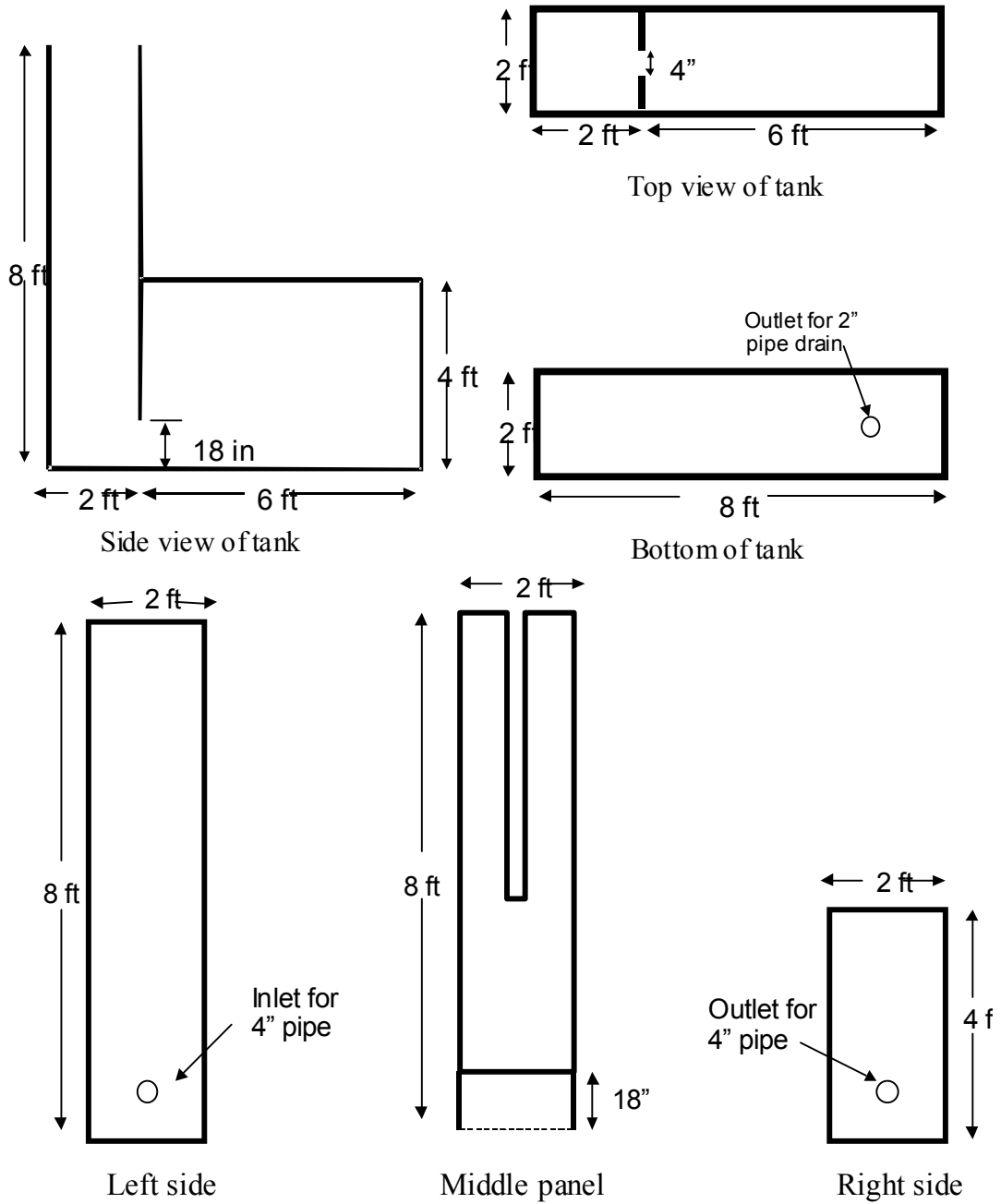


Figure D.3. Detailed diagrams of pilot scale spray contactor

Appendix E Sample storage and stability

Samples were analyzed under a variety of conditions to determine the stability of the liquid samples. In the base case protocol, the samples were stored in phosphate buffer in a tightly capped glass vial and analyzed the next day. Several samples of the feed stream in a laboratory experiment were taken and should have the same concentration of CO₂. The base case analyses are compared with other protocols in the following figure.

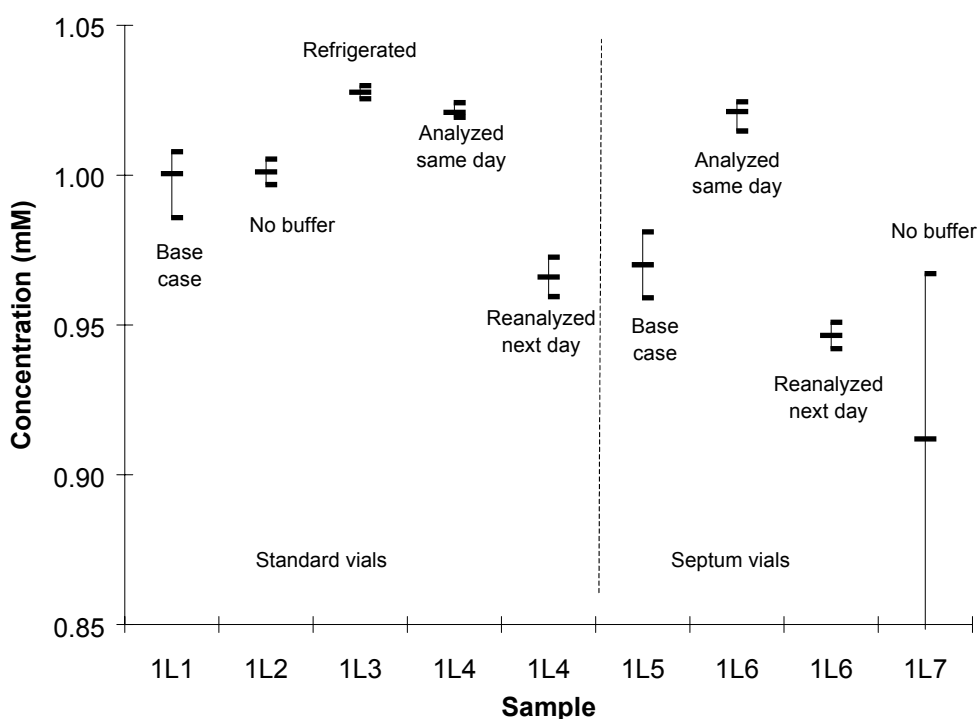


Figure E.1. Sample storage and stability

Glass vials with septa were used to attempt to limit losses of CO₂ to the air. With the standard vials, when the vials were opened to perform analyses, the samples were exposed to air. With the septa, syringes were used to withdraw sample for analysis. However, very little effect of using the vials with septa was observed, and the measured concentrations were even somewhat lower with the septa than with the standard vials.

A comparison of samples 1L1 with 1L2 and 1L5 with 1L7 illustrates the effect of storing samples in phosphate buffer. The phosphate buffer solution stabilized the samples and improved the reproducibility of analyses.

The stability of the samples was also tested by analyzing two of the samples (1L4 and 1L6) on the same day as they were collected. The concentrations of 1L4 and 1L6 were slightly higher than the base case samples (1L1 and 1L5), indicating that some of the carbonate might have desorbed from the liquid into the gas headspace of the vial overnight. When samples 1L4 and 1L6 were reanalyzed the next day, the concentrations were much lower. Thus, once the vials are opened and the samples are analyzed, they appear to lose significant amounts of carbonate to the atmosphere.

ASTM standard D513-92 suggests that samples be stored at a temperature below that at which they are collected until they can be analyzed. To verify the effectiveness of this procedure, sample 1L3 was refrigerated overnight and analyzed the same day as the base case samples. The refrigerated sample had essentially the same concentration as the sample analyzed immediately after collection (1L4). In light of these results, samples were stored with phosphate buffer in standard glass vials and refrigerated until analysis.

Appendix F Total carbonate analyzer

The procedure for the carbonate analysis was modified from the work of previous researchers at The University of Texas (Bishnoi, 2000; Pacheco, 1998)

SETUP

Drying bed(s)

There are 3 magnesium perchlorate drying beds on the carbonate analyzer. The first bed must be changed each day before analyzing samples. It may also need to be changed again if many samples are to be analyzed. The second drying bed may be changed occasionally if the analyzer continues giving erratic results after changing the first bed. The third drying bed should rarely need to be changed. To change any of the drying beds:

1. Remove the drying bed by pulling up on the glass tube. Be careful not to lose the o-rings.
2. Discard the glass wool and the old bed.
3. Wash out the glass tube and then dry thoroughly.
4. Cut a small piece of glass wool and insert it into one end of the glass tube.
5. Through the other end, fill the tube with magnesium perchlorate.
6. Cut another small piece of glass wool and insert it into the open end of the tube.
7. Place the drying bed back in the carbonate analyzer.
8. Gas flow
9. Verify that the nitrogen (N₂) cylinder is open and the pressure regulator is set at 40 psi.
10. Open the nitrogen needle valve by the hood.
11. Adjust the rotameter so that the middle of the ball float is at 11.
12. Check that the gas is flowing all the way through the analyzer and is not obstructed.

Acid bath

1. Obtain 30wt% phosphoric acid (H₃PO₄) solution.
2. Check the septum on the analyzer for wear. If necessary, turn off gas and replace septum.
3. Using a 3mL syringe, inject approximately 1mL of acid into the analyzer.
4. Place the pen on the chart recorder down to begin recording the analyzer response.
5. Wait for the background CO₂ to be stripped out of solution. Allow the analyzer response to stabilize/return back to “zero”.

CALIBRATION

The calibration solutions and procedure will depend on the expected concentrations of the samples to be analyzed.

Standard solutions

The 1.0 mM standard solution for spray experiments should be prepared fresh each day.

1. Obtain or prepare 10 mM sodium carbonate (Na_2CO_3) solution.
2. Using a volumetric pipet, transfer 5 mL of 10 mM Na_2CO_3 solution into a 50 mL volumetric flask.
3. Dilute the solution to 50 mL with distilled water.

Calibration procedure

Calibrate the total carbonate analyzer by injecting different volumes of known concentration.

1. Adjust the range on the analyzer and the chart recorder. (For spray experiments, the analyzer should be on the 0.05% range and the chart recorder should be on the 200mV range.)
2. Check that the chart recorder output for the carbonate analyzer has leveled off.
3. Use the “position” knob on the chart recorder to position the pen at a convenient level (5 or 10) so that you can see if the analyzer response starts to drift down.
4. Draw 100 μL of standard solution into a 100 μL syringe and then discard it. Flush the syringe a few times in the same fashion.
5. Draw 100 μL of standard solution into a 100 μL syringe. Get as much of the gas out of the syringe as possible.
6. Advance the paper on the chart recorder if it is not already running.
7. Inject the 100 μL of standard solution into the analyzer.
8. Watch for the peak on the chart recorder and label it (e.g. 1.0 mM std, 100 μL).
9. After the analyzer output has returned to zero, repeat steps 5-7 until you have three peaks in close agreement (similar peak heights).
10. Repeat steps 5-9 with other volumes of standard solution (70, 50, 30, and 10 μL).

A typical calibration curve is shown in the following figure. The equation gives the millimoles of carbonate in the injection as a function of the magnitude of the analyzer response. The standard error of the y-estimate for the regression was typically about 2% of the response when experimental samples were analyzed.

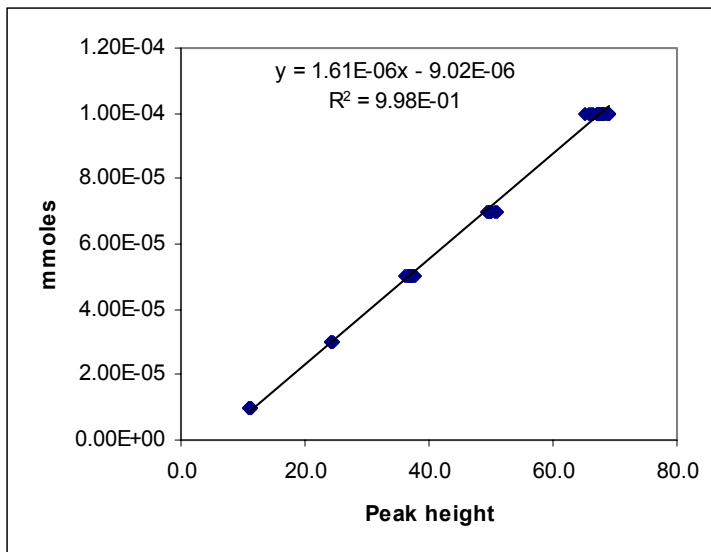


Figure F.1. Typical calibration curve for carbonate analyzer

ANALYSIS

For each sample to be analyzed, the volume of injection may need to be adjusted. If the sample has a high carbonate concentration, less should be injected so that the analyzer response stays within the calibration range. However, the injection volume should be as high as possible. Ideally, the sample injection volume will be in the same range as the calibrations (50-100 μL).

1. Draw 100 μL of the sample into a 100 μL syringe and then discard it. Flush the syringe a few times in the same fashion.
2. Draw 50 μL of sample into a 100 μL syringe. Get as much of the gas out of the syringe as possible.
3. Advance the paper on the chart recorder if it is not already running.
4. Inject the 50 μL of sample into the analyzer.
5. Watch for the peak on the chart recorder and label it (e.g. Sample 1, 50 μL).
6. If the peak height is above the calibrated range, repeat steps 2-5 with a smaller injection volume. If the peak height is low, consider increasing the injection volume. It may be more convenient to use a different size syringe (e.g. 50 or 250 μL).
7. Repeat steps 2-5 until you have three peaks in close agreement (similar peak heights).

TROUBLESHOOTING

From time to time, check that the rotameter is still at 11 and inject 100 μL of standard solution to check the calibration.

Sample cell full

1. Remove the acid bath/sample solution from the analyzer with the 3mL syringe.
2. Using a 3mL syringe, inject approximately 1mL of acid into the analyzer.
3. Wait for the background CO₂ to be stripped out of solution. Allow the analyzer response to stabilize/return back to “zero”.
4. Inject 100 μL of standard solution to check the calibration.

Sudden decrease in gas flow

1. Check gas flow through analyzer
2. May need to change the drying bed. Turn off the gas flow, empty the acid bath, and replace the drying bed(s).

No response from analyzer

1. Check gas flow through analyzer
2. Inspect tubing inside and outside of analyzer.

SHUTDOWN

1. Reduce the gas flow by turning the rotameter down to about 3.
2. Remove the acid bath/sample solution from the analyzer with the 3mL syringe.
3. Turn the rotameter down to zero. Close the nitrogen needle valve by the hood.
4. If no one else is using the nitrogen, close the cylinder.
5. Rinse the syringes with distilled water.

Appendix G Tabulated data

Concentrations given in mM

* denotes outlying data points, neglected when computing the average feed concentration

Quench sampler development

Nozzle **1/64 jet** (no packing in sampler)

C buffer 0.38

C OH 0.94

ΔP (psi)	OH	Level	C feed	flux cm/s	f	C spray	N_L
5	No	High	2.60	0.38	4.58E-04	2.09	0.220
5	No	Low	2.79	0.38	4.58E-04	1.60	0.557
5	Yes	High	2.62	0.38	4.58E-04	2.74	-0.043
5	Yes	Low	2.68	0.38	4.58E-04	2.60	0.030
10	No	High	2.91	0.53	4.48E-04	1.73	0.519
10	No	Low	2.76	0.53	4.48E-04	1.23	0.809

Nozzle **1/64 jet**

C buffer 0.46

C OH 0.33

ΔP (psi)	OH	Level	C feed	flux cm/s	f	C spray	N_L
5	No	High	0.59	0.40	4.81E-04	0.62	-0.04
5	No	Low	0.84	0.40	4.81E-04	0.57	0.38
5	Yes	High	1.07	0.40	4.81E-04	1.01	0.06
5	Yes	Low	1.11	0.40	4.81E-04	1.09	0.01
10	No	High	2.04	0.53	4.48E-04	1.27	0.41
10	No	Low	1.91	0.53	4.48E-04	1.39	0.32
10	Yes	High	1.90	0.53	4.48E-04	1.93	0.00
10	Yes	Low	1.84	0.53	4.48E-04	1.57	0.20
20	No	High	0.95	0.77	4.65E-04	0.48	0.67
20	No	Low	1.02	0.77	4.65E-04	0.50	0.64
20	Yes	High	0.93	0.77	4.65E-04	0.73	0.26
20	Yes	Low	0.94	0.77	4.65E-04	0.61	0.45
Distance from nozzle = 11"							
20	Yes	High	0.91	0.77	4.65E-04	0.57	0.51

Nozzle 1/64" jet
 C buffer 0.31
 C OH 0.37

ΔP (psi)	C feed	flux (cm/s)	f	C spray	N_L
5	4.71	0.38	4.53E-04	4.30	0.06
5	4.46	0.38	4.53E-04	4.30	0.06
10	3.87	0.53	4.54E-04	3.64	0.05
10	3.79	0.53	4.54E-04	3.84	0.00
20	*3.99	0.76	4.56E-04	3.15	0.06
20	3.30	0.76	4.56E-04	3.12	0.07

Nozzle 1/64" jet slanted
 C buffer 0.15
 C OH 0.45

ΔP (psi)	C feed	flux (cm/s)	f	C spray	N_L
5	9.70	0.35	4.23E-04	12.29	-0.24
10	5.99	0.51	4.33E-04	5.91	0.01
20	10.86	0.74	4.44E-04	9.04	0.18

Nozzle 3/64 jet
 C buffer 0.14
 C OH 0.42

ΔP (psi)	C feed	flux (cm/s)	f	C spray	N_L
5	3.51	2.77	3.33E-03	3.60	-0.02
10	4.21	3.97	3.38E-03	3.88	0.08
20	4.39	5.66	3.41E-03	4.56	-0.04

Nozzle 3/64" jet
 C buffer 0.29
 C OH 0.31

ΔP (psi)	C feed	flux (cm/s)	f	C spray	N_L
5	2.34	2.81	3.38E-03	2.17	0.10
5	2.34	2.81	3.38E-03	2.47	-0.03

Laboratory spray mass transfer measurements

Nozzle 1/8-A-SS-2

C buffer 0.21

C OH 0.53

ΔP (psi)	C feed	r (cm)	flux (cm/s)	C spray	N_L
10	2.84	1.3	1.05	1.54	0.62
10	2.85	2.5	0.60	1.26	0.82
10	2.84	3.8	0.47	1.29	0.79
10	2.85	5.1	0.24	0.98	1.07
20	2.60	1.3	1.37	1.39	0.66
20	2.67	5.1	0.53	0.82	1.18
20	2.79	8.9	0.27	0.80	1.21

Nozzle 1/8-A-SS-2

C buffer 0.26

C OH 0.29

ΔP (psi)	C feed	x (in)	y (in)	r (cm)	flux (cm/s)	C spray	N_L
10	3.64	0.3	0.5	1.3	1.11	2.08	0.58
10	3.75	0.6	1.0	2.9	0.65	1.72	0.77
10	*3.99	1.0	1.5	4.5	0.43	1.39	0.98
10	3.73	1.3	2.0	6.2	0.17	1.93	0.65
20	3.00	0.5	0.5	1.7	1.21	1.44	0.75
20	2.95	0.8	1.0	3.2	0.78	1.29	0.86
20	3.12	1.3	1.3	4.5	0.35	1.54	0.69
20	3.16	1.3	2.0	6.2	0.26	0.98	1.14

Nozzle **1/8-A-SS-5**
 C buffer 0.15
 C OH 0.45

ΔP (psi)	C feed	r (cm)	flux (cm/s)	C spray	N_L
5	2.09	1.3	2.28	1.68	0.21
5	2.12	2.5	1.36	1.41	0.38
5	2.07	5.1	0.88	1.31	0.46
5	2.05	8.9	0.81	1.19	0.56
5	2.02	14.0	0.24	1.17	0.57
10	2.13	1.3	2.81	1.59	0.21
10	2.03	2.5	1.53	1.32	0.39
10	1.87	6.4	0.85	1.19	0.50
10	2.02	10.2	0.45	1.15	0.53
10	1.73	19.7	0.04	0.96	0.71
20	2.08	2.5	2.40	1.17	0.56
20	2.07	5.1	1.44	1.12	0.61
20	2.02	10.2	0.51	1.08	0.65
20	2.06	15.9	0.22	0.84	0.90
20	2.02	22.2	0.07	0.86	0.87

Nozzle **1/4-A-SS-10**
 C buffer 0.28
 C OH 0.56

ΔP (psi)	C feed	x (in)	y (in)	r (cm)	flux (cm/s)	C spray	N_L
5	1.73	1.00	2.00	5.7	1.31	1.22	0.36
5	1.76	2.00	3.50	10.2	0.60	1.04	0.53
5	1.75	4.00	6.00	18.3	0.09	1.06	0.50
10	1.70	1.00	1.00	3.6	2.71	1.23	0.31
10	1.70	2.00	3.00	9.2	0.73	1.03	0.49
10	1.68	3.00	4.50	13.7	0.27	0.93	0.59
10	1.66	4.00	6.00	18.3	0.03	0.89	0.64
10	1.68	5.00	8.00	24.0	0.03	0.90	0.63
20	1.72	1.00	1.00	3.6	3.66	1.01	0.52
20	1.69	2.00	2.50	8.1	1.61	0.93	0.60
20	1.68	3.00	5.00	14.8	0.37	0.89	0.65
20	1.70	4.00	6.00	18.3	0.21	0.85	0.70

Nozzle 1/4-A-SS-10 slanted

C buffer 0.23

C OH 0.61

ΔP (psi)	C feed	x (in)	y (in)	r (cm)	flux (cm/s)	C spray	N_L
10	1.80	0	1.38	3.5	3.67	1.15	0.44
10	*1.55	0	3.38	8.6	1.09	1.51	0.03
10	1.76	0	5.38	13.7	0.45	1.03	0.54
10	1.71	0	7.50	19.1	0.15	1.14	0.41
10	1.71	0	9.38	23.8	0.14	1.07	0.47

Nozzle 1/4-A-SS-10 slanted

C buffer 0.32

C OH 0.56

ΔP (psi)	C feed	x (in)	y (in)	r (cm)	flux (cm/s)	C spray	N_L
5	1.76	0	1.38	3.5	2.05	1.31	0.28
5	1.78	0	3.38	8.6	0.84	1.16	0.40
5	1.70	0	5.38	13.7	0.34	1.16	0.40
5	1.67	0	7.38	18.7	0.14	1.08	0.47
10	1.73	0	1.38	3.5	2.62	1.10	0.44
10	1.69	0	3.38	8.6	1.07	1.14	0.40
10	1.65	0	5.38	13.7	0.40	1.05	0.48
10	1.75	0	7.38	18.7	0.14	1.02	0.51
10	1.67	0	9.38	23.8	0.07	0.96	0.56
20	1.68	0	3.38	8.6	1.37	1.08	0.44
20	1.68	0	5.38	13.7	0.53	1.06	0.46
20	1.69	0	7.38	18.7	0.27	0.98	0.54
20	1.69	0	9.38	23.8	0.15	0.99	0.53

Nozzle 3/8-A-SS-20
C buffer 0.12
C OH 0.45

ΔP (psi)	C feed	r (cm)	flux (cm/s)	C spray	N_L
5	2.05	3.2	5.35	1.72	0.16
5	2.06	7.6	2.19	1.54	0.27
5	2.05	12.7	0.96	1.36	0.39
5	1.96	17.8	0.48	1.34	0.41
5	2.02	24.1	0.23	1.37	0.39
5	1.98	38.7	0.06	1.28	0.45
10	2.06	3.5	5.82	1.63	0.18
10	1.95	7.6	2.90	1.34	0.38
10	1.83	12.1	1.10	1.35	0.37
10	1.90	17.8	0.50	1.06	0.61
10	1.98	25.4	0.22	1.18	0.51
10	1.98	40.6	0.06	1.15	0.53

Pilot scale spray mass transfer measurements

Nozzle 3CF-SILCNB-120
 ΔP (psi) 5
C buffer 0.27
C OH 0.55

x (in)	y (in)	r (cm)	flux (cm/s)	C feed	C spray	N_L
14.5	20	80.3	1.72	1.93	1.39	0.33
20	26	100.8	1.39	2.01	1.66	0.15
25	31	118.8	1.13	2.03	1.45	0.29
30	37	138.4	0.92	1.86	1.44	0.30
38	49	174.2	0.45	1.96	1.35	0.36
38	49	174.2	0.45	1.85	1.34	0.37
40	47	174.3	0.57	1.93	1.36	0.35
36	51	174.4	0.21	1.93	1.60	0.19
42	45	174.7	0.17	†1.93	1.49	0.26

† Interpolated from other measurements of feed concentration

Nozzle **3CF-SILCNB-120**
 ΔP (psi) **10**
 C buffer 0.25
 C OH 0.39

x (in)	y (in)	r (cm)	flux (cm/s)	C feed	C spray	N_L
12	19	73.8	2.38	2.02	1.45	0.28
12	19	73.8	2.38	†1.94	1.50	0.24
16	26	93.4	1.37	1.90	1.41	0.31
18	24	93.7	1.60	1.94	1.38	0.33
26	33	124.0	1.23	1.85	1.35	0.35
28	31	124.6	0.67	1.98	1.22	0.45
36	44	161.7	0.81	1.86	1.37	0.34
41	50	181.4	0.67	†1.92	1.31	0.38
39.6	51.5	181.6	0.50	†1.89	1.35	0.35
43	48	181.6	0.64	1.93	1.34	0.36
43	48	181.6	0.60	1.87	1.24	0.44
45	46	182.1	0.17	1.91	1.40	0.32

† Interpolated from other measurements of feed concentration

Nozzle **3CF-SILCNB-120**
 ΔP (psi) **20**
 C buffer 0.23
 C OH 0.33

x (in)	y (in)	r (cm)	flux (cm/s)	C feed	C spray	N_L
30	34	133.3	1.19	1.74	0.99	0.56
33	42	152.7	1.13	1.76	1.32	0.27
35	40	152.9	1.32	1.70	1.24	0.34
38	46	168.9	1.18	1.74	1.19	0.38
36	48	168.9	0.71	1.68	1.31	0.28
40	44	169.2	0.99	*2.23	1.04	0.51
42	42.5	170.6	0.36	1.78	1.44	0.19

Mass transfer during spray impact

Pool impact experiment

Nozzle 1/4-A-SS-10
 C buffer 0.23
 C OH N/A

ΔP (psi)	C feed	x (in)	y (in)	r (cm)	flux (cm/s)	C spray	N_L	Predicted		Regressed
								N_L spray	N_L pool	N_L pool
5	2.57	1.0	2.3	6.3	1.10	1.34	0.64	0.35	0.29	0.33
5	2.46	2.5	5.0	14.4	0.29	0.96	0.97	0.45	0.52	0.41
5	2.55	4.0	7.5	21.9	0.07	0.91	1.03	0.51	0.52	0.52
10	2.61	0.5	1.0	3.0	2.77	1.31	0.63	0.32	0.31	0.36
10	2.33	2.0	3.3	9.9	0.50	0.92	0.99	0.47	0.52	0.48
10	2.44	4.0	7.5	21.9	0.07	0.75	1.19	0.60	0.60	0.67
20	2.24	0.8	1.5	4.2	3.07	0.86	0.95	0.42	0.53	0.45
20	2.18	2.5	4.5	13.2	0.49	0.70	1.15	0.60	0.55	0.62
20	2.21	4.0	6.8	20.0	0.19	0.51	1.47	0.68	0.79	0.73

Spray interception experiment

Nozzle 2 1/8-A-SS-5
 C buffer 0.27
 C OH 0.50

ΔP (psi)	C feed	x (in)	y (in)	x (cm)	flux (cm/s)	C spray	N_L	N_L avg	N_L int - N_L avg	Average	Stdev
5	2.93	-5.00	3.50	-12.7	0.31	1.71	0.53	0.61		0.02	0.02
5	2.92	-2.50	3.50	-6.4	0.17	1.53	0.64		0.03		
5	2.89	2.50	3.50	6.4	0.24	1.58	0.61		0.01		
5	2.91	4.50	3.50	11.4	0.28	1.47	0.68				
10	2.90	-5.13	3.50	-13.0	0.36	1.92	0.40	0.57		0.11	0.04
10	2.90	-2.63	3.50	-6.7	0.15	1.48	0.66		0.08		
10	2.75	2.50	3.50	6.4	0.21	1.40	0.71		0.14		
10	2.88	4.25	3.50	10.8	0.31	1.35	0.75				
20	*3.02	-5.50	3.50	-14.0	0.50	1.52	0.62	0.66		0.15	0.08
20	2.89	-3.00	3.50	-7.6	0.19	1.20	0.86		0.20		
20	2.81	2.75	3.50	7.0	0.33	1.34	0.75		0.09		
20	2.82	4.75	3.50	12.1	0.38	1.42	0.69				

Wall impact experiment

Nozzle 1/8-A-SS-10

C buffer 0.23

C OH 0.28

ΔP (psi)	C_{feed}	x (in)	y (in)	r (cm)	Q_p (cm ³ /min)	C spray	N_L	Predicted				Regressed
								N_L spray	N_L ww	flux	N_L imp	N_L imp
5	2.54	1.50	2.50	7.4	137.7	1.20	0.73	0.36	0.11	0.64	0.25	0.27
5	2.53	2.50	4.00	12.0	81.6	0.91	1.01	0.42	0.16	0.27	0.43	0.40
5	2.46	4.00	6.00	18.3	49.3	0.74	1.22	0.48	0.21	0.13	0.53	0.58
10	2.49	2.25	3.00	9.5	68.7	0.88	1.02	0.46	0.17	0.52	0.39	0.36
10	2.48	3.00	4.50	13.7	64.4	0.72	1.23	0.52	0.18	0.27	0.53	0.49
10	2.37	4.00	5.00	16.3	51.5	0.65	1.33	0.55	0.21	0.20	0.57	0.56
20	2.36	1.50	2.50	7.4	81.6	0.91	0.94	0.50	0.16	1.04	0.28	0.31
20	2.33	3.00	4.00	12.7	34.2	0.56	1.44	0.59	0.26	0.40	0.58	0.49
20	2.34	4.00	5.50	17.3	34.2	0.54	1.47	0.65	0.26	0.23	0.55	0.64

Semi-empirical model predictions

Nozzle	Experimental				Sheet predictions					Droplet predictions				Total
	T (°C)	ΔP (psi)	r (cm)	N _L	L _b (cm)	k _{LS} (cm/s)	a _s (cm ⁻¹)	t _s (ms)	N _{LS}	k _{Ld} (cm/s)	d ₃₂ (μm)	t _d (ms)	N _{Ld}	N _L
1/8-A-SS-2 ¹	22	10	1.3	0.62	3.01	0.615	448.2	1.08	0.298	0.072	334.6	0.00	0.000	0.298
	22	10	2.5	0.82	3.01	0.309	802.9	2.16	0.537	0.072	334.6	0.00	0.000	0.537
	22	10	3.8	0.79	3.01	0.261	934.4	2.56	0.625	0.072	334.6	0.68	0.009	0.634
	22	10	5.1	1.07	3.01	0.261	934.4	2.56	0.625	0.072	334.6	1.76	0.023	0.648
	22	20	1.3	0.66	2.42	1.166	468.0	0.76	0.417	0.077	307.2	0.00	0.000	0.417
	22	20	5.1	1.18	2.42	0.615	806.1	1.46	0.722	0.077	307.2	1.60	0.024	0.746
	22	20	8.9	1.21	2.42	0.615	806.1	1.46	0.722	0.077	307.2	3.90	0.059	0.781
	22	10	1.34	0.58	3.01	0.581	469.1	1.15	0.312	0.072	334.6	0.00	0.000	0.312
	22	10	2.89	0.77	3.01	0.272	899.5	2.46	0.602	0.072	334.6	0.00	0.000	0.602
	22	10	4.51	0.98	3.01	0.261	934.4	2.56	0.625	0.072	334.6	1.28	0.017	0.642
	22	10	6.17	0.65	3.01	0.261	934.4	2.56	0.625	0.072	334.6	2.69	0.035	0.660
	22	20	1.69	0.75	2.42	0.877	592.2	1.02	0.529	0.077	307.2	0.00	0.000	0.529
	22	20	3.18	0.86	2.42	0.615	806.1	1.46	0.722	0.077	307.2	0.46	0.007	0.729
	22	20	4.47	0.69	2.42	0.615	806.1	1.46	0.722	0.077	307.2	1.23	0.019	0.741
22	20	6.17	1.14	2.42	0.615	806.1	1.46	0.722	0.077	307.2	2.26	0.034	0.756	
1/8-A-SS-5	22	5	1.3	0.21	4.47	0.522	192.8	1.53	0.154	0.059	439.1	0.00	0.000	0.154
	22	5	2.5	0.38	4.47	0.262	327.4	3.06	0.263	0.059	439.1	0.00	0.000	0.263
	22	5	5.1	0.46	4.47	0.150	531.6	5.38	0.428	0.059	439.1	0.74	0.006	0.434
	22	5	8.9	0.56	4.47	0.150	531.6	5.38	0.428	0.059	439.1	5.33	0.043	0.471
	22	5	14.0	0.57	4.47	0.150	531.6	5.38	0.428	0.059	439.1	11.44	0.092	0.520
	22	10	1.3	0.21	3.59	0.990	200.5	1.08	0.215	0.063	403.1	0.00	0.000	0.215
	22	10	2.5	0.39	3.59	0.497	342.4	2.16	0.368	0.063	403.1	0.00	0.000	0.368
	22	10	6.4	0.50	3.59	0.353	459.5	3.06	0.495	0.063	403.1	2.35	0.022	0.517
	22	10	10.2	0.53	3.59	0.353	459.5	3.06	0.495	0.063	403.1	5.60	0.052	0.548

Nozzle	Experimental				Sheet predictions					Droplet predictions				Total
	T (°C)	ΔP (psi)	r (cm)	N _L	L _b (cm)	k _{Ls} (cm/s)	a _s (cm ⁻¹)	t _s (ms)	N _{Ls}	k _{Ld} (cm/s)	d ₃₂ (μm)	t _d (ms)	N _{Ld}	N _L
1/8-A-SS-5 (cont.)	22	10	19.7	0.71	3.59	0.353	459.5	3.06	0.495	0.063	403.1	13.71	0.128	0.624
	22	20	2.5	0.56	2.88	0.943	358.1	1.53	0.517	0.067	370.1	0.00	0.000	0.517
	22	20	5.1	0.60	2.88	0.832	398.3	1.74	0.575	0.067	370.1	1.32	0.014	0.589
	22	20	10.2	0.64	2.88	0.832	398.3	1.74	0.575	0.067	370.1	4.38	0.048	0.623
	22	20	15.9	0.89	2.88	0.832	398.3	1.74	0.575	0.067	370.1	7.83	0.085	0.660
	22	20	22.2	0.86	2.88	0.832	398.3	1.74	0.575	0.067	370.1	11.65	0.126	0.701
1/4-A-SS-10	22	5	18.3	0.50	5.03	0.184	328.7	6.06	0.366	0.054	498.3	16.00	0.103	0.469
	22	5	10.2	0.52	5.03	0.184	328.7	6.06	0.366	0.054	498.3	6.27	0.040	0.406
	22	5	5.7	0.36	5.03	0.184	328.7	6.06	0.366	0.054	498.3	0.78	0.005	0.371
	22	10	9.2	0.49	4.04	0.433	285.0	3.44	0.425	0.057	457.5	4.36	0.033	0.458
	22	10	18.3	0.64	4.04	0.433	285.0	3.44	0.425	0.057	457.5	12.16	0.091	0.516
	22	10	3.6	0.31	4.04	0.487	258.1	3.06	0.385	0.057	457.5	0.00	0.000	0.385
	22	10	13.7	0.59	4.04	0.433	285.0	3.44	0.425	0.057	457.5	8.26	0.062	0.487
	22	10	24.0	0.63	4.04	0.433	285.0	3.44	0.425	0.057	457.5	16.97	0.127	0.552
	22	20	14.8	0.65	3.25	1.022	248.0	1.95	0.495	0.061	420.1	6.97	0.061	0.556
	22	20	3.6	0.52	3.25	1.022	248.0	1.95	0.495	0.061	420.1	0.21	0.002	0.497
	22	20	8.1	0.60	3.25	1.022	248.0	1.95	0.495	0.061	420.1	2.94	0.026	0.521
	22	20	18.3	0.69	3.25	1.022	248.0	1.95	0.495	0.061	420.1	9.08	0.079	0.574
	22	10	19.1	0.41	4.04	0.433	285.0	3.44	0.425	0.057	457.5	12.78	0.096	0.521
	22	10	13.7	0.54	4.04	0.433	285.0	3.44	0.425	0.057	457.5	8.19	0.061	0.486
	22	10	3.5	0.44	4.04	0.501	252.1	2.97	0.376	0.057	457.5	0.00	0.000	0.376
	22	10	23.8	0.47	4.04	0.433	285.0	3.44	0.425	0.057	457.5	16.84	0.126	0.551
	22	5	3.5	0.28	5.03	0.264	241.1	4.21	0.268	0.054	498.3	0.00	0.000	0.268
	22	5	8.6	0.40	5.03	0.184	328.7	6.06	0.366	0.054	498.3	4.26	0.028	0.393
	22	5	13.7	0.40	5.03	0.184	328.7	6.06	0.366	0.054	498.3	10.38	0.067	0.433
	22	5	18.7	0.47	5.03	0.184	328.7	6.06	0.366	0.054	498.3	16.50	0.106	0.472
22	10	3.5	0.44	4.04	0.501	252.1	2.97	0.376	0.057	457.5	0.00	0.000	0.376	

Nozzle	Experimental				Sheet predictions					Droplet predictions				Total
	T (°C)	ΔP (psi)	r (cm)	N _L	L _b (cm)	k _{Ls} (cm/s)	a _s (cm ⁻¹)	t _s (ms)	N _{Ls}	k _{Ld} (cm/s)	d ₃₂ (μm)	t _d (ms)	N _{Ld}	N _L
¼-A-SS-10 (cont.)	22	10	8.6	0.40	4.04	0.433	285.0	3.44	0.425	0.057	457.5	3.86	0.029	0.454
	22	10	13.7	0.48	4.04	0.433	285.0	3.44	0.425	0.057	457.5	8.19	0.061	0.486
	22	10	18.7	0.51	4.04	0.433	285.0	3.44	0.425	0.057	457.5	12.51	0.094	0.519
	22	10	23.8	0.56	4.04	0.433	285.0	3.44	0.425	0.057	457.5	16.84	0.126	0.551
	22	20	8.6	0.44	3.25	1.022	248.0	1.95	0.495	0.061	420.1	3.21	0.028	0.523
	22	20	13.7	0.46	3.25	1.022	248.0	1.95	0.495	0.061	420.1	6.27	0.055	0.550
	22	20	18.7	0.54	3.25	1.022	248.0	1.95	0.495	0.061	420.1	9.33	0.081	0.576
	22	20	23.8	0.53	3.25	1.022	248.0	1.95	0.495	0.061	420.1	12.39	0.108	0.603
⅜-A-SS-20	22	5	3.2	0.16	5.79	0.424	116.4	3.82	0.189	0.048	577.9	0.00	0.000	0.189
	22	5	7.6	0.27	5.79	0.234	188.0	6.97	0.306	0.048	577.9	2.21	0.011	0.317
	22	5	12.7	0.39	5.79	0.234	188.0	6.97	0.306	0.048	577.9	8.33	0.041	0.348
	22	5	17.8	0.41	5.79	0.234	188.0	6.97	0.306	0.048	577.9	14.45	0.072	0.378
	22	5	24.1	0.39	5.79	0.234	188.0	6.97	0.306	0.048	577.9	22.10	0.110	0.416
	22	5	38.7	0.45	5.79	0.234	188.0	6.97	0.306	0.048	577.9	39.69	0.198	0.504
	22	10	3.5	0.18	4.65	0.732	130.4	2.97	0.284	0.051	530.6	0.00	0.000	0.284
	22	10	7.6	0.38	4.65	0.551	163.8	3.96	0.357	0.051	530.6	2.53	0.015	0.372
	22	10	12.1	0.37	4.65	0.551	163.8	3.96	0.357	0.051	530.6	6.32	0.037	0.394
	22	10	17.8	0.61	4.65	0.551	163.8	3.96	0.357	0.051	530.6	11.19	0.065	0.422
	22	10	25.4	0.51	4.65	0.551	163.8	3.96	0.357	0.051	530.6	17.68	0.102	0.459
	22	10	40.6	0.53	4.65	0.551	163.8	3.96	0.357	0.051	530.6	30.66	0.177	0.534
3CF-SILCNB-120	33	10	182	0.38	9.01	2.636	7.8	7.67	0.159	0.031	1224.7	147.34	0.223	0.382
	33	10	182	0.47	9.01	2.636	7.8	7.67	0.159	0.031	1224.7	147.34	0.223	0.382
	38	10	182	0.36	8.52	2.888	7.6	7.26	0.160	0.033	1224.7	147.75	0.236	0.396
	38	10	181	0.38	8.52	2.888	7.6	7.26	0.160	0.033	1224.7	146.90	0.234	0.394
	38	10	182	0.44	8.52	2.888	7.6	7.26	0.160	0.033	1224.7	147.75	0.236	0.396
	38	10	124	0.35	8.52	2.888	7.6	7.26	0.160	0.033	1224.7	98.35	0.157	0.317
	38	10	94	0.33	8.52	2.888	7.6	7.26	0.160	0.033	1224.7	72.80	0.116	0.276

Nozzle	Experimental				Sheet predictions					Droplet predictions				Total
	T (°C)	ΔP (psi)	r (cm)	N _L	L _b (cm)	k _{Ls} (cm/s)	a _s (cm ⁻¹)	t _s (ms)	N _{Ls}	k _{Ld} (cm/s)	d ₃₂ (μm)	t _d (ms)	N _{Ld}	N _L
3CF-SILCNB-120 (cont.)	38	10	74	0.28	8.52	2.888	7.6	7.26	0.160	0.033	1224.7	55.77	0.089	0.249
	38	10	74	0.24	8.52	2.888	7.6	7.26	0.160	0.033	1224.7	55.77	0.089	0.249
	38	10	162	0.34	8.52	2.888	7.6	7.26	0.160	0.033	1224.7	130.71	0.209	0.368
	39	5	174	0.36	10.50	1.247	8.3	12.64	0.131	0.031	1333.9	196.94	0.274	0.404
	39	5	174	0.37	10.50	1.247	8.3	12.64	0.131	0.031	1333.9	196.94	0.274	0.404
	39	5	174	0.35	10.50	1.247	8.3	12.64	0.131	0.031	1333.9	196.94	0.274	0.404
	39	5	80	0.33	10.50	1.247	8.3	12.64	0.131	0.031	1333.9	83.71	0.116	0.247
	39	5	101	0.15	²									
	39	5	138	0.30	10.50	1.247	8.3	12.64	0.131	0.031	1333.9	153.57	0.213	0.344
	39	5	119	0.29	10.50	1.247	8.3	12.64	0.131	0.031	1333.9	130.69	0.182	0.312
	35	20	133	0.56	7.08	6.447	7.1	4.26	0.196	0.034	1124.5	75.84	0.136	0.332
	35	20	169	0.51	7.08	6.447	7.1	4.26	0.196	0.034	1124.5	97.52	0.175	0.371
	35	20	169	0.38	7.08	6.447	7.1	4.26	0.196	0.034	1124.5	97.52	0.175	0.371
	35	20	153	0.34	7.08	6.447	7.1	4.26	0.196	0.034	1124.5	87.88	0.158	0.354

¹Data for 1/8-A-SS-2 was not included in the regression of the model parameters

²Unusually low data point was neglected because of negative estimates for the sheet N_L (N_{Ls} = N_L - N_{Ld})

Appendix H Sample calculations for spray contacting

Example 1: Calculate N_L for spray contactor such as the scrubber in Figure 1.1

Assumptions:

Physical properties of water at 60°C

$$\text{Liquid density} = 0.982 \text{ g/cm}^3$$

$$\text{Liquid viscosity} = 0.0052 \text{ g/cm s}$$

$$\text{Surface tension} = 66.4 \text{ g/s}^2$$

$$\text{Liquid phase diffusion coefficient for SO}_2 = 3.57 \times 10^{-5} \text{ cm}^2/\text{s}$$

Vertical header spacing of 5 ft

3CF-120 spray nozzles ($d_{or} = 2 \frac{1}{16}$ in)

$$\Delta P = 7 \text{ psi}$$

$$d_{32} = 1240 \text{ }\mu\text{m}$$

$$\theta = 90^\circ \text{ (with countercurrent gas flow)}$$

The initial velocity may be calculated from the nozzle pressure drop.

$$U_o = \sqrt{\frac{2\Delta P}{\rho_L}} = 991 \frac{\text{cm}}{\text{s}}$$

From the capacity rating of the nozzle and the operating pressure,

$$Q = 120 \frac{\text{gal}}{\text{min}} \left(\frac{\Delta P}{7 \text{ psi}} \right)^{0.5} = 7570 \frac{\text{cm}^3}{\text{s}}$$

The initial thickness of the sheet at the nozzle exit is then

$$h_o = \frac{d_{or}}{2 \cos(\frac{\theta}{2})} \left(1 - \sqrt{1 - \frac{4Q \cos(\frac{\theta}{2})}{U_o \pi d_{or}^2}} \right) = 0.497 \text{ cm}$$

Dimensionless groups for the sheet are computed

$$\text{Re}_o = \frac{h_o U_o \rho_L}{\mu_L} = 92600$$

$$\text{We}_o = \frac{h_o U_o^2 \rho_L}{\sigma} = 7240$$

$$\text{Sc}_L = \frac{\mu_L}{\rho_L D_L} = 149$$

The sheet breakup length is calculated from the empirical correlation

$$L_b = d_{or} * 4740 \text{Re}_o^{-0.8} \text{We}_o^{0.07} = 4.92 \text{cm}$$

The mass transfer coefficient of the sheet is given by the semi-empirical relation

$$\text{Sh}_s = 1.64 \times 10^{-4} \text{Re}_o^{0.81} \text{We}_o^{0.84} \text{Sc}^{0.5} = 36900$$

$$k_{L_s} = \text{Sh}_s * \left(\frac{D_L}{h_o} \right) = 2.64 \frac{\text{cm}}{\text{s}}$$

The area per unit volume of the sheet

$$a_s = \frac{2\pi U_o}{Q} \left(d_{or} - 2h_o \cos\left(\frac{\theta}{2}\right) + L_b \sin\left(\frac{\theta}{2}\right) \right) = 6.59 \text{cm}^{-1}$$

Then, the N_L of the sheet is predicted as

$$N_{L_s} = k_{L_s} a_s \frac{L_b}{U_o} = 0.087$$

In the droplet region, the sprays are assumed to be independent since no data exists for spray interaction or its significance for mass transfer. The droplets travel from the nozzle down to the next spray header.

The distance from the spray nozzle to the next header

$$r = \frac{\text{header spacing}}{\cos\left(\frac{\theta}{2}\right)} = 2.16 \text{m}$$

The theoretical k_L for oscillation is

$$\tau_{osc} = \frac{\pi}{4} \sqrt{\frac{\rho_L d_{32}^3}{\sigma}} = 0.0042 \text{s}$$

$$k_{L_d} = 2 \sqrt{\frac{D}{\pi \tau_{osc}}} = 0.104 \frac{\text{cm}}{\text{s}}$$

Then, the N_L of the droplet region is predicted as

$$N_{L_d} = 0.36 k_{L_d} \left(\frac{6}{d_{32}} \right) \left(\frac{r - L_b}{U_o} \right) = 0.39$$

When the spray droplets encounter the next header, the piping and nozzles associated with the header provide many opportunities for spray impact phenomena. Assuming the spray flux is similar to those measured in the pilot scale experiments,

$$\text{flux} = 0.53 \Delta P^{0.46} r^{-1.8} = 0.32 \frac{\text{cm}}{\text{s}}$$

Then the mass transfer during spray impact may be estimated

$$N_{L,\text{imp}} = 0.0056 U_o^{0.55} (\text{flux})^{-0.47} = 0.42$$

The total N_L is the sum of the contributions of the sheet, droplets, and impact.

$$N_L = N_{Ls} + N_{Ld} + N_{L,\text{imp}} = 0.90$$

Example 2: Oxygen (O_2) absorption from air at 60°C and atmospheric pressure
Same nozzle and scrubber design as above

Physical properties same as before, except

Liquid phase diffusion coefficient for $O_2 = 5.24 \times 10^{-5} \text{ cm}^2/\text{s}$

Oxygen solubility $m = 1.15 \times 10^6 \text{ cm}^3/\text{mol}$

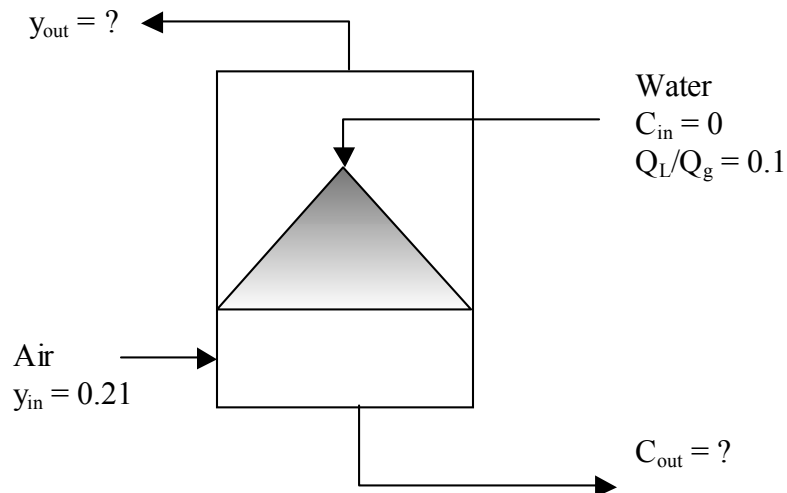
Assumptions:

The mass transfer is liquid phase controlled

O_2 is the only species being transferred

Dilute concentrations of O_2 in the water

(a) Compute the concentration of dissolved oxygen in the water outlet.



Calculate N_L as before, correcting for the diffusion coefficient of O_2 .

$$N_L = N_{L,SO_2} \left(\frac{D_{L,O_2}}{D_{L,SO_2}} \right)^{0.5} = 1.09$$

For liquid phase control, $N_{OL} \approx N_L$

$$N_{OL} = \frac{C_{in} - C_{out}}{(C - C^*)_{lm}} = \frac{C_{in} - C_{out}}{\left(C_{in} - \frac{y_{out}}{m} \right) - \left(C_{out} - \frac{y_{in}}{m} \right)} = 1.09$$

$$\ln \left(\frac{C_{in} - \frac{y_{out}}{m}}{C_{out} - \frac{y_{in}}{m}} \right)$$

A material balance gives the operating line for the absorber

$$Q_L (C_{out} - C_{in}) = Q_g \frac{P}{RT} (y_{in} - y_{out})$$

Since the inlet concentrations and the gas-liquid ratio are known, the equations for N_{OL} and the operating line may be solved simultaneously to determine the outlet concentrations.

Thus,

$$y_{out} = 0.2097$$

$$C_{out} = 1.21 \times 10^{-7} \text{ mol/cm}^3 = 0.121 \text{ mM}$$

The concentration of O_2 in the gas outlet is approximately the same as the inlet because the liquid to gas ratio and the solubility of O_2 are low.

(b) Determine the liquid to gas ratio to achieve 10% O_2 in the gas outlet.

The liquid to gas ratio may be varied to attain appreciable removal of O_2 from the gas stream. If the change in the total gas flow rate is small, it may be neglected and the liquid to gas ratio remains constant. If the gas and liquid are assumed to be in plug flow, the above analysis may be followed.

Plug flow case:

$$Q_L/Q_g = 42.5$$

$$C_{out} = 9.47 \times 10^{-8} \text{ mol/cm}^3 = 0.0947 \text{ mM}$$

However, the gas phase is expected to experience backmixing. If the gas phase is assumed to be well mixed and the liquid remains plug flow, then the equation for N_{OL} has to be modified to use y_{out} in the log mean driving force.

$$N_{OL} = \frac{C_{in} - C_{out}}{(C - C^*)_{lm}} = \frac{C_{in} - C_{out}}{\left(C_{in} - \frac{y_{out}}{m} \right) - \left(C_{out} - \frac{y_{out}}{m} \right)} = 1.09$$

$$\ln \left(\frac{C_{in} - \frac{y_{out}}{m}}{C_{out} - \frac{y_{out}}{m}} \right)$$

Again, the equations for the operating line and N_{OL} are solved simultaneously. To attain a concentration of 10% O_2 in the gas outlet,

Well mixed case:

$$Q_L/Q_g = 70.0$$

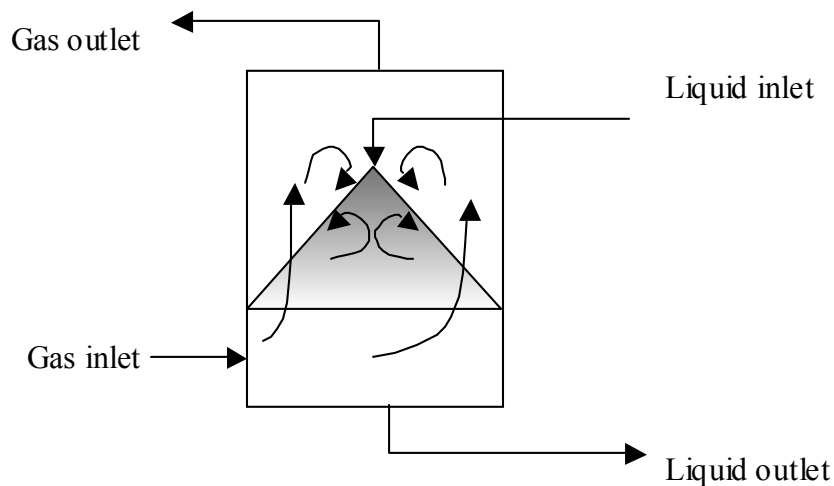
$$C_{out} = 5.75 \times 10^{-8} \text{ mol/cm}^3 = 0.0575 \text{ mM}$$

If the absorber were designed assuming plug flow ($Q_L/Q_g = 42.5$) but the gas is well mixed, then the outlet concentrations would be

$$y_{out} = 0.126$$

$$C_{out} = 7.24 \times 10^{-8} \text{ mol/cm}^3 = 0.0724 \text{ mM}$$

In practice, the gas distribution will be somewhere between the plug flow and the well mixed cases.



In addition, the liquid phase mass transfer (k_L) varies in the spray absorber and may be very different from the gas distribution. The high k_L in the sheet may result in local starvation of O_2 depending on the distribution of gas flow. Thus, fundamental modeling of spray gas-liquid contactors should combine the results of the current work with measurements of the gas phase mass transfer and gas distribution as a function of position in the contactor.

Bibliography

- Agarwal, R.S. *Limestone Slurry Scrubbing – Modeling and Parameter Estimation*. Ph.D. Dissertation, The University of Texas at Austin, 1995.
- Altwickler, E.R.; Lindhjem, C.E. Absorption of Gases into Drops. *AIChE J.* **1988**, 34 (2), 329-332.
- American Society for Testing and Materials (ASTM). Standard Practice for Determining Data Criteria and Processing for Liquid Drop Size Analysis. *Annual Book of ASTM Standards*, Designation E799-92, 1998.
- American Society for Testing and Materials (ASTM). Standard Test Methods for Total and Dissolved Carbon Dioxide in Water. *Annual Book of ASTM Standards*, Designation D513-92, 1996.
- Amokrane, H.; Caussade, B. Gas Absorption into a Moving Spheroidal Water Drop. *J. Atm. Sci.* **1999**, 56 (12), 1808-1829.
- Amokrane, H.; Saboni, A.; Caussade, B. Experimental Study and Parameterization of Gas Absorption by Water Drops. *AIChE J.* **1994**, 40 (12), 1950-1960.
- Angelo, J.B.; Lightfoot, E.N.; Howard, D.W. Generalization of the Penetration Theory for Surface Stretch: Application to Forming and Oscillating Drops. *AIChE J.* **1966**, 12 (4), 751-760.
- Bishnoi, S. *Carbon Dioxide Absorption and Solution Equilibrium in Piperazine Activated Methyl-diethanolamine*. Ph.D. Dissertation, The University of Texas at Austin, 2000.
- Brogren, C.; Karlsson, H.T. Modeling the absorption of SO₂ in a spray scrubber using the penetration theory. *Chem. Eng. Sci.* **1997**, 52 (18), 3085-3099.
- Caussade, B.; Saboni, A. Hydrodynamics and Mass Transfer on a Moving Drop of Water. In *Air-Water Mass Transfer*, Selected Papers from the Second International Symposium on Gas Transfer at Water Surfaces, Minneapolis, MN, Sept 11-14, 1990.
- Chigier, N.A. The Physics of Atomization. Plenary Lecture. In *Proceedings of the Fifth International Conference on Liquid Atomization and Spray Systems*, Gaithersburg, MD, July 15-18, 1991; Semerjian, H.G., Ed.; National Institute of Standards and Technology, Gaithersburg, MD, 1991.
- Clift, R.; Grace, J.R.; Weber, M.E. *Bubbles drops and particles*; Academic Press: New York, 1978.
- Corsi, R.L.; Olson, D.A. Section 5.2 Emission Models. In *Odor and VOC Control Handbook*; Rafson, H.J., Ed.; McGraw-Hill: New York, 1998.

- Davies, J.T. *Turbulence phenomena*; Academic Press: New York, 1972.
- Davies, J.T.; Hameed, A. Gas Absorption into Turbulent Jets of Kerosene. *Chem. Eng. Sci.* **1971**, 26, 1295-1296.
- Davies, J.T.; Ting, S.T. Mass Transfer into Turbulent Jets. *Chem. Eng. Sci.* **1967**, 22, 1539-1548.
- Demyanovich, R.J. Absorption of Carbon Dioxide by Impinging Thin Liquid Sheets. *Chem. Eng. Comm.* **1991**, 103, 151-166.
- DeVincentis, J.W. *Modeling of Limestone Slurry Scrubbing in Spray Towers with Forced Oxidation*. M.S. Thesis, The University of Texas at Austin, December 1998.
- Dimiccoli, A.; Di Serio, M.; Santacesaria, E. Mass Transfer and Kinetics in Spray-Tower-Loop Absorbers and Reactors. *Ind. Eng. Chem. Res.* **2000**, 39 (11), 4082-4093.
- Dombrowski, N.; Hooper, P.C. The Effect of Ambient Density on Drop Formation in Sprays. *Chem. Eng. Sci.* **1962**, 17, 291-305.
- Dombrowski, N.; Johns, W.R. The aerodynamic instability and disintegration of viscous liquid sheets. *Chem. Eng. Sci.* **1963**, 18, 203-214.
- Edge, R.M.; Grant, C.D. Terminal Velocity and Frequency of Oscillation of Drops in Pure Systems. *Chem. Eng. Sci.* **1971**, 26 (7), 1001-1012.
- Epstein, M. *EPA Alkali Scrubbing Test Facility: Summary of Testing through October 1974*. Publication No. EPA-650/2-75-047; U.S. Environmental Protection Agency: Washington, DC, 1975.
- Fair, J.R.; Steinmeyer, D.E.; Penney, W.R.; Crocker, B.B. Section 18 Liquid-Gas Systems. In *Perry's Chemical Engineers' Handbook*, 6th ed.; Perry, R.H.; Green, D.W., Maloney, J.O., Eds.; McGraw-Hill: New York, 1984.
- Fortescue, G.E.; Pearson, J.R.A. On Gas Absorption into a Turbulent Liquid. *Chem. Eng. Sci.* **1967**, 22, 1163-1176.
- Fraser, R.P.; Eisenklam, P.; Dombrowski, N.; Hasson, D. Drop Formation from Rapidly Moving Liquid Sheets. *AIChE J.* **1962**, 8 (5), 672-680.
- Gage, C.L.; Rochelle, G.T. Limestone Dissolution in Flue Gas Scrubbing: Effect of Sulfite. *J. Air Waste Manage. Assoc.* **1992**, 42, 926-935.
- Gage, S.J. Approaches for Control of Acid Rain. In *Proceedings: Symposium on Flue Gas Desulfurization – Houston, October 1980: Volume 1*; U.S. Environmental Protection Agency: Washington, DC, 1980.

- Garner, F.H.; Lane, J.J. Mass Transfer to Drops of Liquid Suspended in a Gas Stream Part II: Experimental Work and Results. *Trans. Inst. Chem. Eng.* **1959**, 37, 162-172.
- George, J.; Minel, F.; Grisenti, M. Physical and Hydrodynamical Parameters Controlling Gas-Liquid Mass Transfer. *Int. J. Heat Mass Transfer* **1994**, 37 (11), 1569-1578.
- Grace, J.R.; Wairegi, T.; Nguyen, T.H. Shapes and Velocities of Single Drops and Bubbles Moving Freely through Immiscible Liquids. *Trans. Inst. Chem. Eng.* **1976**, 54 (3), 167-173.
- Hadamard, J.S. Mouvement Permanent lent d'une Sphere Liquide et Visqueuse dans un Liquide Visqueux. *Comptes Rendus de l'Academie des Sciences* **1911**, 152, 1735-1738.
- Håkansson, R. ABB: Växjö, Sweden. Personal communication, 1998.
- Handlos, A.E.; Baron, T. Mass and Heat Transfer from Drops in Liquid-Liquid Extraction. *AIChE J.* **1957**, 3 (1), 127-136.
- Hasson, D.; Luss, D.; Peck, R. Theoretical Analyses of Vapour Condensation on Laminar Liquid Jets. *Int. J. Heat Mass Transfer* **1964**, 7, 969-981.
- Hewitt, R.A.; Saleem, A. Operation and Maintenance Experience of the World's Largest Spray Tower SO₂ Scrubbers. In *Proceedings: Symposium on Flue Gas Desulfurization – Houston, October 1980: Volume 1*; U.S. Environmental Protection Agency: Washington, DC, 1980.
- Higbie, R. The Rate of Absorption of a Pure Gas into a Still Liquid during Short Periods of Exposure. *Trans. AIChE* **1935**, 31, 365-389.
- Hines, A.L.; Maddox, R.N. *Mass Transfer: Fundamentals and Applications*; Prentice-Hall: Englewood Cliffs, NJ, 1985.
- Hsu, C.T.; Shih, S.M. Semiempirical Equation for Liquid-Phase Mass-Transfer Coefficient for Drops, *AIChE J.* **1993**, 39 (6), 1090-1092.
- Hu, S.; Kintner, R.C. The Fall of Single Liquid Drops through Water. *AIChE J.* **1955**, 1, 42-48.
- Hughes, R.R.; Gilliland, E.R. Mass Transfer Inside Drops in a Gas. *Chem. Eng. Prog. Symp. Series* **1955**, 51 (16), 101-120.
- Hughes, R.R.; Gilliland, E.R. The Mechanics of Drops. *Chem. Eng. Prog.* **1952**, 48 (10), 497-504.
- Ibrahim, E.A. Characteristics of the spray produced by liquid sheets atomization. Proceedings of the 1998 ASME Fluids Engineering Division Summer Meeting: Washington, DC, June 21-25, 1998.

- Jarvis, J.B.; Burke, J.M. *EPRI High-Sulfur Test Center: Wet FGD Sodium Carbonate Mass-Transfer Tests*; Report CS-6029; Electric Power Research Institute (EPRI): Palo Alto, CA, 1988.
- Jett, B. Spraying Systems Company: Wheaton, IL. Personal communication, 1999.
- Johnson, A.I.; Braida, L. Velocity of Fall of Circulating and Oscillating Liquid Drops through Quiescent Liquid Phases. *Can. J. Chem. Eng.* **1957**, 35, 165-172.
- Jozewicz, W.; Singer, C.; Srivastava, R.K.; Tsigotis, P.E. *Status of SO₂ Scrubbing Technologies*. In *EPRI-DOE-EPA Combined Utility Air Pollutant Control Symposium: The MEGA Symposium: Volume 1: SO₂ Controls*, Atlanta, GA, August 16-20, 1999; Electric Power Research Institute: Palo Alto, CA, 1999.
- Kaji, R.; Hishinuma, Y.; Kuroda, H. SO₂ Absorption by Water Droplets. *J. Chem. Eng. Japan* **1985**, 18 (2), 169-172.
- King, C.J. *Separation Processes*, 2nd ed.; McGraw-Hill: New York, 1980.
- Klee, A.J.; Treybal, R.E. Rate of Rise or Fall of Liquid Drops. *AIChE J.* **1956**, 2, 444-447.
- Koehn, D. Spraying Systems Company: Borden, TX. Personal communication, 2001.
- Kronig, R.; Brink, J. C. On the Theory of Extraction from Falling Droplets. *Applied Scientific Research* **1950**, A2, 142-154.
- Laddha, G.S.; Degaleesan, T.E. *Transport Phenomena in Liquid Extraction*, McGraw-Hill: New York, 1978.
- Lamb, H. *Hydrodynamics*; Dover Publications, Inc.: New York, 1945.
- Lamont, J.C.; Scott, D.S. An Eddy Cell Model of Mass Transfer into the Surface of a Turbulent Liquid. *AIChE J.* **1970**, 16 (4), 513-519.
- Laslo, D. Alstom Power: Knoxville, TN. Personal communication, 2002.
- Lefebvre, A.H. *Atomization and Sprays*; Hemisphere Publishing Corp.: New York, 1989.
- Levich, V.G. *Physicochemical Hydrodynamics*; Prentice-Hall: Englewood Cliffs, NJ, 1962.
- Liley, P.E.; Reid, R.C.; Buck, E. Section 3 Physical and Chemical Data. In *Perry's Chemical Engineers' Handbook*, 6th ed.; Perry, R.H.; Green, D.W., Maloney, J.O., Eds.; McGraw-Hill: New York, 1984.
- Lin, W.C.; Rice, P.A.; Cheng, Y.S.; Barduhn, A.J. Vacuum Stripping of Refrigerants in Water Sprays. *AIChE J.* **1977**, 23 (4), 409-415.

- Marshall, W.R., Jr. *Atomization and Spray Drying*; Chemical Engineering Progress Monograph Series No. 2; American Institute of Chemical Engineers: New York, 1954.
- Mashayek, F.; Ashgriz, N. Nonlinear Oscillations of Drops with Internal Circulation. *Phys. Fluids* **1998**, 10 (5), 1071-1082.
- McWhirter, J.R.; Chern, J.M.; Hutter, J.C. Oxygen Mass Transfer Fundamentals of Surface Aerators. *Ind. Eng. Chem. Res.* **1995**, 34 (8), 2644-2654.
- Mehta, K.C.; Sharma, M.M. Mass Transfer in Spray Columns. *Br. Chem. Eng.* **1970**, 15, 1440-1444, 1556-1558.
- Montgomery, D.C. *Design and Analysis of Experiments*, 4th ed.; John Wiley & Sons: New York, 1997.
- Noblett, J.G.; Shires, T.M.; Moser, R.E. Recent Applications of FGDPRISM for Operations Optimization and SO₂ Removal Enhancement. Presented at the SO₂ Control Symposium, Miami, FL, 1995.
- Nonnenmacher, S.; Piesche, M. Design of hollow cone pressure swirl nozzles to atomize Newtonian fluids. *Chem. Eng. Sci.* **2000**, 55, 4339-4348.
- Oskarsson, K.; Berglund, A.; Deling, R.; Snellman, U.; Stenback, O.; Fritz, J.J. *A Planner's Guide for Selecting Clean-Coal Technologies for Power Plants*. World Bank Technical Paper 387. The World Bank: Washington, DC, 1997.
- Pacheco, M.A. *Mass Transfer, Kinetics, and Rate-Based Modeling of Reactive Absorption*. Ph.D. Dissertation, The University of Texas at Austin, 1998.
- PBS Frontline. Available at <http://www.pbs.org/wgbh/pages/frontline/shows/blackout/future/> (2001).
- Piarah, W.H.; Paschedag, A.; Kraume, M. Numerical Simulation of Mass Transfer between a Single Drop and an Ambient Flow. *AIChE J.* **2001**, 47 (7), 1701-1704.
- Pigford, R.L.; Pyle, C. Performance Characteristics of Spray-Type Absorption Equipment. *Ind. Eng. Chem.* **1951**, 43 (7), 1649-1662.
- Pinilla, E.A.; Diaz, J.M.; Coca, J. Mass Transfer and Axial Dispersion in a Spray Tower for Gas-Liquid Contacting. *Can. J. Chem. Eng.* **1984**, 62, 617-622.
- Prasher, B.D.; Fricke, A.L. Mass Transfer at a Free Gas-Liquid Interface in Turbulent Thin Films. *Ind. Eng. Chem. Process Des. Dev.* **1974**, 13 (4), 336-340.
- Rayleigh, L. On the Instability of Jets. *Proc. London Math. Soc.* **1878**, 10, 4-13.
- Ruckenstein, E. Mass Transfer between a Single Drop and a Continuous Phase. *Int. J. Heat Mass Trans.* **1967**, 10, 1785-1792.

- Rybczynski, W. Über die fortschreitende bewegung einer flussigen kugel in einem zahem medium. *Bulletin International de l'Academic Polonaise des Sciences et des Lettres, Classe des Sciences Mathematiques et Naturelles, Serie A* **1911**, 40-46.
- Schroeder, R.R.; Kintner, R.C. Oscillations of Drops Falling in a Liquid Field. *AIChE J.* **1965**, 11 (1), 5-8.
- Seibert, A.F.; Fair, J.R. Hydrodynamics and Mass Transfer in Spray and Packed Liquid-Liquid Extraction Columns. *Ind. Eng. Chem. Res.* **1988**, 27 (3), 470-481.
- Seibert, A.F.; Fair, J.R. Mass-transfer efficiency of a large-scale sieve tray extractor. *Ind. Eng. Chem. Res.* **1993**, 32 (10), 2213-2219.
- Senecal, P.K.; Schmidt, D.P., Nouar, I.; Rutland, C.J.; Reitz, R.D.; Corradini, M.L. Modeling high-speed viscous liquid sheet atomization. *Int. J. Multiphase Flow* **1999**, 25, 1073-1097.
- Simpson, S.G.; Lynn, S. Vacuum-Spray Stripping of Sparingly Soluble Gases from Aqueous Solutions: Part I. Mass Transfer from Streams Issuing from Hydraulic Nozzles. *AIChE J.* **1977**, 23 (5), 666-73.
- Skelland, A.H.P.; Woo, S.; Ramsay, G.G. Effects of Surface-Active Agents on Drop Size, Terminal Velocity, and Droplet Oscillation in Liquid-Liquid Systems. *Ind. Eng. Chem. Res.* **1987**, 26 (5), 907-911.
- Spraying Systems Company: Wheaton, IL. Catalog 60 Industrial Spray Products, 2000; 194-196, 251-252.
- Spraying Systems Company: Wheaton, IL. Whirljet nozzle data sheet 11825-9.
- Srinivasan, V.; Aiken, R.C. Mass Transfer to Droplets Formed by the Controlled Breakup of a Cylindrical Jet – Physical Absorption. *Chem. Eng. Sci.* **1988**, 43 (12), 3141-3150.
- Subramanyam, S.V. A Note on the Damping and Oscillations of a Fluid Drop Moving in Another Fluid. *J. Fluid Mech.* **1969**, 37 (4), 715-725.
- Tamir, A.; Rachmilev, I. Absorption of Carbon Dioxide in a Rapid Laminar Fan-shaped Water Sheet. *Chem. Eng. J.* **1972**, 4, 85-90.
- Taniguchi, I.; Takamura, Y.; Asano, K. Experimental Study of Gas Absorption with a Spray Column. *J. Chem. Eng. Japan.* **1997**, 30 (3), 427-433.
- Train, R.E. Sulfur Oxide Control and Electricity Production. In Proceedings: Symposium on Flue Gas Desulfurization New Orleans March 1976: Volume 1; U.S. Environmental Protection Agency: Washington, DC, 1976.
- Trompiz, C.J.; Fair, J.R. Entrainment from spray distributors for packed columns. *Ind. Eng. Chem. Res.* **2000**, 39, 1797-1808.

- U.S. Department of Energy (DOE). *Report of the National Energy Policy Development Group*. Available at http://www.energy.gov/HQPress/releases01/maypr/energy_policy.htm (2001)
- U.S. Environmental Protection Agency (EPA). *Acid Rain Program: Overview*. Available at <http://www.epa.gov/airmarkets/arp/overview.html> (2001).
- U.S. Environmental Protection Agency (EPA). *Air Pollution Technology Fact Sheet: Spray-Tower Scrubber*. Available at <http://www.epa.gov/ttn/catc/products.html> (2000).
- U.S. Environmental Protection Agency (EPA). *The Effects of Title IV of the Clean Air Act Amendments of 1990 on Electric Utilities: An Update*. Available at http://www.eia.doe.gov/cneaf/electricity/clean_air_upd97/exec_sum.html (1997).
- Versteeg, G.F.; van Swaaij, W.P.M. Solubility and Diffusivity of Acid Gases (CO₂, N₂O) in Aqueous Alkanolamine Solutions. *J. Chem. Eng. Data* **1988**, 33, 29.
- Vivian, J.E.; Peaceman, D.W. Liquid-side Resistance in Gas Absorption. *AIChE J.* **1956**, 2 (4), 437-443.
- Walcek, C.J.; Pruppacher, H.R.; Topalian, J.H.; Mitra, S.K. On the Scavenging of SO₂ by Cloud and Raindrops: II. An Experimental Study of SO₂ Absorption and Desorption for Water Drops in Air. *J. Atm. Chem.* **1984**, 1, 291-306.
- Weast, R.C., Ed. *CRC Handbook of Chemistry and Physics*, 1st Student Edition; Chemical Rubber Company Press: Boca Raton, FL, 1988.

Vita

Norman Kirk Yeh, the son of Hou Leh and Wendy Yeh was born July 26, 1974 in Bedford, Texas. After graduating from Trinity High School in Euless, Texas, in 1992, he attended the Massachusetts Institute of Technology in Cambridge, Massachusetts. In 1996, he received the degree of Bachelor of Science in chemical engineering with a minor in chemistry. He then enrolled in the David H. Koch School of Chemical Engineering Practice at MIT. As part of the Practice School, he was an intern at Merck & Company in West Point, Pennsylvania, and the Dow Chemical Company in Freeport, Texas. In 1997, he received the degree of Master of Science in Chemical Engineering Practice. That fall, he entered the Graduate School of The University of Texas at Austin.

Permanent employment has been accepted at the ExxonMobil Upstream Research Company in Houston, Texas.

Permanent address: 401 W. Ash Lane, Euless, Texas, 76039

This dissertation was typed by the author.